ISTANBUL TECHNICAL UNIVERSITY ★ GRADUATE SCHOOL OF SCIENCE ENGINEERING AND TECHNOLOGY

A NUMERICAL INVESTIGATION INTO THE EFFECT OF THE VERTICAL TAPERED WINGLETS ON FULLY-SUBMERGED HYDROFOILS

M.Sc. THESIS

Aras ÇETİNKAYA

Department of Naval Architecture and Marine Engineering

Naval Architecture and Marine Engineering Programme

NOVEMBER 2017

ISTANBUL TECHNICAL UNIVERSITY ★ GRADUATE SCHOOL OF SCIENCE ENGINEERING AND TECHNOLOGY

A NUMERICAL INVESTIGATION INTO THE EFFECT OF THE VERTICAL TAPERED WINGLETS ON FULLY-SUBMERGED HYDROFOILS

M.Sc. THESIS

Aras ÇETİNKAYA
(508121018)

Department of Naval Architecture and Marine Engineering

Naval Architecture and Marine Engineering Programme

Advisor: Assoc. Prof. Dr. U. Oral UNAL

NOVEMBER 2017

İSTANBUL TEKNİK ÜNİVERSİTESİ ★ FEN BİLİMLERİ ENSTİTÜSÜ

DİKEY KANATÇIKLARIN TAMAMEN BATMIŞ SUALTI KANATLARINA ETKİLERİNİN SAYISAL YÖNTEMLE İNCELENMESİ

YÜKSEK LİSANS TEZİ

Aras ÇETİNKAYA
(508121018)

Gemi İnşaatı ve Gemi Makineleri Anabilim Dalı

Gemi İnşaatı ve Gemi Makinaları Mühendisliği Programı

Tez Danışmanı: Doc. Dr. U. Oral ÜNAL

KASIM 2017

Aras ÇETINKAYA, a M.Sc. student of ITU Graduate School of Science Engineering and Technology 508121018, successfully defended the thesis entitled "A NUMERICAL INVESTIGATION INTO THE EFFECT OF THE VERTICAL TAPERED WINGLETS ON FULLY-SUBMERGED HYDROFOILS", which he prepared after fulfilling the requirements specified in the associated legislations, before the jury whose signatures are below.

Advisor :	**Assoc. Prof. Dr. U.Oral ÜNAL** Istanbul Technical University	.....
Jury Members :	**Prof. Dr. Ömer GÖREN** Istanbul Technical University	.....
	Asst. Prof. Dr. Murat ÖZBULUT Piri-Reis University	.....

Date of Submission : 13/11/2017
Date of Defence : 28/11/2017

To the unknown,

FOREWORD

I would like to extend my sincerest thanks and gratitude to Assoc. Prof. Dr. Uğur Oral ÜNAL for always helping me with his knowledge, foresight, and discipline, for bringing my creative ideas to maturity, for improving my observational skills, and for never letting my self-confidence falter throughout this dissertation.

I would also like to thank my beloved father and mother, Adnan ÇETİNKAYA and Keysun ÇETİNKAYA for giving me with the biggest motivation, and for the continuous emotional and financial support they have given me as I wrote this thesis.

I would like to thank Talat Gökçer CANYURT, Çagri AYDIN, and Çagatay Sabri KÖKSAL, my researcher and engineer friends, with whom I greatly enjoy my discussions and the sharing of our ideas, and whom I admire for not letting me feel lonely in my academic and professional life, for giving me their time and energy when I came across obstacles.

I would like to thank my room and desk mates Ahmet Yusuf GÜRKAN and Gürbüz BİLİCİ, with whom I have enjoyed talking, working, and spending time, for all their help during the entirety of my higher education.

I would like to sincerely thank my dear uncle Tahsin ÇETİNKAYA, who helps me correct my mistakes, for selflessly and patiently helping me solve technical problems I have faced with his knowledge, experience, and intellect.

Lastly, I would like to thank my friends, whom I feel proud to call so, Taylan Berkin TÖRAL, Beytullah Onur USTA, Serdar BENDERLİ, and İsmail Anıl KILINÇ, for all their indirect helps by sharing my happiness and my troubles, and for always being with me.

November 2017

Aras Çetinkaya
(Naval Architect – Marine Engineer)

TABLE OF CONTENTS

Page

ABBREVIATES

AMG **:** Algebric Multigrid
AOA **:** Angle of Attack
CFD **:** Computational Fluid Dynamics
DNS **:** Direct Numerical Simulation
HAD **:** Hesaplamalı Akışkanlar Mekaniği
LES **:** Large Eddy Simulation
LLM **:** Lifting Line Method
NACA **:** National Advisory Committee for Aeronautics
NASA **:** National Aeronautics and Space Administration
N-S **:** Navier-Stokes
RANS **:** Reynolds Averaged Navier Stokes
SIMPLE **:** Semi-Implicit Method for Pressure-Linked Equations
SST **:** Shear Stress Transport
VLM **:** Vortex Lattice Method
BMAX **:** Boeing-Max Series

SYMBOLS

A_n	: Fourier serial coefficients
C_D	: Total drag coefficient
C_{Di}	: Induced drag coefficient
C_{Dp}	: Profile drag coefficient
$C_{D(2D)}$	: Two dimentional drag coefficient
$C_{D(2.5D)}$	: Drag coefficient of wing with infinite span
C_L	: Total lift coefficient
Cl	: Sectional lift coefficient
Cl_a	: 2D lift coefficient slope
Cp	: Pressure coefficient
c	: Chord length
Cmw	: Chord length of main wing
Cwr	: Root chord length of winglet
Cwt	: Tip chord length of winglet
Di	: Induced Drag
e	: Span efficiency factor
M	: Mach number
k	: Turbulence kinetic energy
Li	: Induced Lift
L	: Lift
P	: Pressure
Re	: Reynolds number
S	: Projection area of wing
Sw	: Span length of winglet
V_∞	: Freestream velocity
ω	: Dissipation magnitude per unit kinetic energy
$\vec{\omega}$	: Vorticity
ω_x	: X vorticity
ω_i	: Local downwash velocity
y^+	: Dimentionless distance from wall surface

α	: Angle of attack
α_i	: Induced angle of attack
α_{geo}	: Geometric angle of attack
α_o	: Zero lift angle of attack
α_∞	: Freestream angle of attack
γ	: Sectional circulation
ρ	: Density
Γ	: Total circulation
Θ	: Sweep angle of winglet's trailing edge
θ	: Fourier function angle
Ψ	: Cant angle
ν	: Kinematic viscosity
τ	: Stress function
Λ, AR	: Aspect Ratio
μ	: Dynamic viscosity
η	: Kolmogorov length scale

LIST OF TABLES

Page

LIST OF FIGURES

Page

A NUMERICAL INVESTIGATION INTO THE EFFECT OF THE VERTICAL TAPERED WINGLETS ON FULLY-SUBMERGED HYDROFOILS

SUMMARY

In this study, the effects of variations of the basic parameters of winglets, which have similar characteristics in each wing, on the efficiency of a wing underwater are examined. Computational Fluid Dynamics (CFD) was used to obtain the result. The executive equations of the CFD analyzes were used with the SIMPLE algorithm, which is a decompression method that gives a pressure rate-dependence for the continuous flow of a Reynolds-averaged Navier Stokes (RANS) based numerical study, and the SST k-ω turbulence model chosen for boundary layer flow analysis.

In the study, a rectangular wing with a cross section of NACA0012, a section length of 1 meter and a side ratio of 6 was used. During the entire study, the attack angle of the main wing was kept constant at 5^o and the Reynolds number at $6x10^6$. The solution volumes created for the analyzes were created around the half-wing opening using the mirror principle. The performance of the new wing structures formed by attaching the selected blades NACA0006 onto the tip of the bare wing were compared with each other and with the bare wing for each parameter examined. The wings are generally regarded as simple wedges with a taper ratio of 0.3 as a simple basic geometry.

A validation study has been conducted with the aim of checking the consistency and reliability of the CFD solution mesh and method used. The independence studies of the grids were carried out together with the validation studies and the final solution grid parameters selected for the 3D wing were preserved while the solution meshes of the wingleted wings were constructed.

The winglet geometry parameters examined in this study are the ratio of the winglet root section length to the base wing section length, the ratio of the winglet span to the base wing section length, the direction of the winglet, and the angle of the winglet trailing edge. These parameters are symbolized as CCR, SCR, DW and β, respectively. Parameters such as the radius of junction and the cant angle are not investigated since the optimal values may vary in different basic wings and in different flow conditions. It was predicted that the effect of the examined winglets only on the induced speeds should not be attributed to the lift force of the whole wing itself and therefore the slope of the bladder was fixed at 0 °. Firstly, the CCR ratio was fixed upwards at a direction of 0.5 and at β 0o. The flapping wings examined are labeled W1, W2 and W3 respectively. As a result of analysis, the most efficient wing was determined as W1 with 6.19% CL / CD increase. The W1 wing also provided the highest value of 10.03 per cent as a CL increase between 3 wings. No decline was observed in CD values, but W3 was observed with a minimum increase of 2.41%. This shows that the winglets are not effective enough in reducing the induced drag force than the contributions to the profile drag force. W3 has the

least surface area and gives the least value in CD increase. However, it has been found that the tip has the lowest value in yield increase since it is the most unsuccessful wing in terms of damping or deformation.

Secondarily, the SCR parameter was examined at three different values of 0.5, 0.75, 1 and the other parameters were kept constant at the same value as the parameters of W1. Therefore, two new wingleted wing analyzes were performed and these wings were coded as W4 and W5, respectively, with SCR values 0.75 and 1, respectively. As a result of analysis, the most efficient wing was determined as W4 with 6.44% CL / CD increase. W4 wing increased 12.22% in CL and 5.42% in CD compared to wingless wing. The W5 wing achieved the highest CL increase by 13%, but at the same time it had the highest value of 7.23% in the CD increase, and performed a more unsuccessful performance than the W4 with a CL / CD value of 5.38%. In view of the results obtained, it has been observed that the liquefaction effect of the SCR ratio has a parabolic structure. Although the optimal SCR rate for this study was found to be 0.75, this value may vary in different wings and in different flow parameters.

The next parameter, the direction of the fin direction, has been investigated in three different ways, up, down and on both sides in total. The other parameters are the same as W4 wing and the wingleted wings directed downwards and oriented to both sides are coded and analyzed and coded as W6 and W7 respectively. As a result of the analysis, the W6 was the wing which provided the least efficiency (CL / CD) increase among all wingleted wings examined. However, it has an important feature that it does not cause CD increase compared to the bare wing. This feature can be applied directly on the existing wing on a hydrofoil boat. In other cases, the other winglets will cause the wing to increase the overall resistance and slow down the vessel by producing extra drift while traveling at maximum speed where the vessel does not need more lifting force. W6 is predicted not to cause a loss in the course of maximum speed but also to decrease the speed of the vessel to go from the hullborne to the foilborne cruise because it will increase the wing efficiency, that is to say, it will produce more lifting force than the same drag force. In order to use the W4 advantage, a wing that is smaller in size and smaller in attack angle should be used, by removing the existing wing, producing the same drift value as the existing wing but producing more lift because the efficiency is higher. In this case, it is predicted that the speed needed to switch from hullborne to foilborne will decrease more than that of the W6. With a different wing design, it is predicted that by replacing the wing with a wing that has a winglet, it is possible to keep the coefficient of lift force constant and to increase the maximum speed of the craft by reducing the resistance. In other words, the advantage of W6 is the ability to increase boat efficiency with a lower investment cost, although it is less efficient than other winglets. The W7 wing provides greater lift than the W4 wing with a CL increase of 13.55% compared to the base wing. However, the CD also caused a further increase of 7.83% from the W4 wing. As a result of these values, it was observed that CL / CD ratio could be increased by 5.28% behind W4. Similar to the comparison of the W4 wing with the W5 wing, this results in a high profile drift force, which is caused by the large surface area, negatively affects the CL / CD ratio, although the W7 wing also damps the induced velocities more effectively.

As a final parameter, the sweep angle β, 0^o and 15^o of the trailing edge are examined. In comparison with W4, the analysis of the winglet which has $\beta = 15^o$ coded as W8 and the same as the other parameters W4 has been carried out. As a result of the

analysis, the increase of 11.93% CL, which the W8 wing provided in accordance with the bare wing, lagged behind the W4 wing. However, the exhibited 6.78% CL / CD increase is only 0.03% higher than the W4. When the distributions of the wake of these two wings and the distribution of pressure coefficients are examined, it is left open to debate whether the W8 wing has the advantage of having a lower risk of cavitation, but with a more distorted wake distribution and a more complex structure in terms of production.

DİKEY KANATÇIKLARIN TAMAMEN BATMIŞ SUALTI KANATLARINA ETKİLERİNİN SAYISAL YÖNTEMLE İNCELENMESİ

ÖZET

Kanatlar bir yüzeyde akışkanın diğer yüzeyine göre daha yüksek hızda ve alçak basınçta akması prensibi ile iki yüzey arasında basınç farkı yaratarak kaldırma kuvveti oluşturmak amacı ile tasarlanan yapılardır. Bu sayede kaldırma kuvveti elde edilir. Ancak kanatların uç noktaları yüksek basınçtan alçak basınca ikincil bir akışın söz konusu olduğu kanadın performansını olumsuz etkileyen bir girdabı oluşturur. Bu girdabın etkilerinin azaltılıp kanadın performansını arttırmak yüz yıla yakın bir süredir özellikle havacılıkta önemli bir araştırma konusudur. Kanatçık ismi verilen ve kanat uçlarına belli bir açı ile yerleştirilen ek kanat parçalarının tasarımı bu konuda yürütülen araştırmaların büyük bir kısmını oluşturmaktadır. Tahmin edileceği üzere, bahsi geçen uç girdap sorunu, ayaklı tekne ismi verilen deniz araçlarının altına yerleştirilen ve hava yerine suda işlev gören kanatlar için de geçerlidir. Bu çalışmada basit geometrilere sahip kanatçık yapılarının, her kanatta benzer özellikler gösterecek temel parametrelerinin değişimlerinin, su altında kullanılan bir kanadın verimine olan etkileri incelenmiştir. Bölüm 1 ve 2 de kanatların çalışma prensibi, ayaklı tekneler ve kanatçıklar hakkında genel bilgi ve literatürde yapılan çalışmalar yer almaktadır.

Sonuç elde etmek amacı ile Hesaplamalı Akışkanlar Dinamiği (HAD) kullanılmıştır. HAD analizlerinin yönetici denklemleri, Reynolds ortalaması alınmış Navier Stokes (RANS) temelli nümerik çalışmanın daimi akış için basınç hız-bağıntısı veren ayrıklaştırma yöntemi olan SIMPLE algoritması ve sınır tabaka akış çözümlemesi için seçilen SST k-ω türbülans modeli hakkında detaylı bilgi Bölüm 3 te verilmiştir.

Çalışmada temel olarak NACA0012 kesitli, kesit uzunluğu 1 metre, yan oranı 6 olan dikdörtgen kanat kullanılmıştır. Tüm çalışma boyunca temel kanadın hücum açısı 5^o de ve Reynolds sayısı $6x10^6$ da sabit tutulmuştur. Analizler için oluşturulan çözüm hacimleri ayna prensibi kullanılarak yarı kanat açıklığı etrafında oluşturulmuştur. Kesitleri NACA0006 olarak seçilen kanatçıkların bahsi geçen temel kanatın uç kısmına eklenmesiyle oluşturulan yeni kanat yapılarının performansları, incelenen her bir parametre için birbirleri ile ve kanatçıksız temel kanat ile karşılaştırılmıştır. Kanatçıklar genel olarak kolay üretilmesi basit bir temel geometri olarak 0.3 sivrilme oranı ile kama kanat olarak ele alınmıştır. Kanat ve kanatçık geometri parametreleri, kullanılan çözüm ağının özelliklerinin detayları ve akışkan özellikleri Bölüm 4 te verilmiştir.

Kullanılan HAD çözüm ağı ve yönteminin tutarlılığı ve güvenilirliğini kontrol etmek amacı ile bir geçerleme çalışması yapılmıştır. Geçerleme çalışması üç ayrı bölüme ayrılmıştır. İlk olarak NACA0012 kesiti etrafındaki akışın ve sınır tabakanın

modellenmesinin kontrolü amacı ile iki boyutlu geçerleme çalışması, NASA tarafından geliştirilen CFL3D HAD kodunun sonuçları ile karşılaştırılmıştır. Daha sonra iki boyutlu olarak yeterli görülen çözüm ağının kanat açıklığı boyunca dağılımının kontrolü için iki buçuk boyutlu olarak adlandırılan sonsuz yan oranlı kanadı temsil eden çözüm ağının geçerlemesi yapılmıştır. En son olarak üç boyutlu çözüm ağının kontrolü iki buçuk boyutlu geçerleme çalışmalarından elde edilen profil sürüklenme kuvveti katsayısı ile kaldırıcı hat metodu ile elde edilen kaldırma kuvveti katsayısı ve indüklenmiş sürüklenme kuvveti katsayısı kullanılarak yapılmıştır. Ağdan bağımsızlık çalışmaları geçerleme çalışmaları ile birlikte yürütülmüş ve 3 boyutlu kanat için seçilmiş nihai çözüm ağı parametreleri kanatçıklı kanatların çözüm ağları oluşturulurken aynen korunmuştur. Ağdan bağımsızlık ve geçerleme çalışmaları ile ilgili detaylı bilgi Bölüm 5 te yer almaktadır.

Bölüm 6 da çeşitli kanatçık geometrili kanatların sonuçlarını birbirleri ile ve kanatçıksız kanat ile karşılaştırılmalarının yorumları yer almaktadır. Bu çalışmada incelenen kanatçık geometrisi parametreleri, kanatçık kök kesit uzunluğunun temel kanat kesit uzunluğuna oranı, kanatçık kanat açıklığının temel kanat kesit uzunluğuna oranı, kanatçığın doğrultu yönü ve kanatçık izler kenarının çalıklık açısıdır. Bu parametrelerden ilk ikisi, sırası ile CCR, SCR, DW ve β olarak sembolize edilmiştir. Optimal değerlerinin farklı temel kanatlarda ve farklı akış şartlarında değişiklik gösterebileceğinden dolayı kant-kanatçık bağlantı kısmına ovalleştirme yarıçapı ve kanatçık burulma açısı gibi parametreler incelenmemiştir. İncelenen kanatçıkların sadece indüklenmiş hızlara etkisinin gözlemlenebilmesi amacı ile kanatçığın kendisinin kaldırma kuvvetine katkısı olmaması gerektiği öngörülmüş ve dolayısı ile kanatçık yatıklık açısı 0^o olarak sabitlenmiştir. Karşılaştırmalarda kaldırma kuvveti katsayısı (C_L), sürüklenme kuvveti katsayısı (C_D) ve bu iki değerin birbirine oranı ile elde edilen verim katsayısı (C_L/C_D) temel alınmıştır. Ancak bunların yanı sıra kanat üzerinde ve iz bölgesinde alınan bazı kesitlerdeki x girdaplılık değerleri, basınç katsayısı dağılımları ve hız vektörleri incelenerek yorum yapılmıştır.

İlk olarak CCR oranı 0.5 doğrultu yönü yukarı doğru ve β 0^o olarak sabitlenmiştir. İncelenen kanatçıklı kanatlar sırası ile W1, W2 ve W3 olarak kodlanmıştır. Analizler neticesinde en verimli kanat %6.19 C_L/C_D artışı ile W1 olarak belirlenmiştir. W1 kanadı aynı zamanda 3 kanat arasında C_L artışı olarak da %10.03 le en yüksek değeri sağlamıştır. C_D değerlerinde ise düşüş gözlemlenmemiş ancak en az yükseliş %2.41 oranı ile W3 de gözlemlenmiştir. Bu durum kanatçıkların yüzeylerinin profil sürüklenme kuvvetine katkılarının indüklenmiş sürüklenme kuvvetini azaltma etkilerinde fazla olduğunu göstermektedir. W3 en az yüzey alanına sahip olduğundan C_D artışında en az değeri vermektedir. Ancak uç girdabını sönümleme ve ya öteleme bakımından en başarısız kanat olduğundan verim artışında en düşük değere sahip olduğu saptanmıştır. İncelenen 3 farklı CCR değerli kanat yapısı içinden en verimlisinin CCR değeri 1 olan olduğu saptanmıştır.

İkincil olarak SCR parametresi üç farklı değerde 0.5, 0.75, 1 olarak incelenmiş ve diğer parametreler W1 in parametreleri ile aynı değerde sabit tutulmuştur. Dolayısı ile iki yeni kanatçıklı kanadın analizi yapılmış ve bu kanatlar SCR değerleri 0.75 ve 1 olmak üzere sırası ile W4 ve W5 olarak kodlanmıştır. Analizler neticesinde en verimli kanat, %6.44 C_L/C_D artışı ile W4 olarak belirlenmiştir. W4 kanadı, kanatçıksız kanada göre C_L de %12.22 artış ve C_D de %5.42 artış sergilemiştir. W5 kanadı %13 ile en yüksek C_L artışını sağlamış ancak aynı zamanda C_D artışında da %7.23 ile en yüksek değeri göstermiştir ve C_L/C_D değerinde %5.38 ile W4 ten daha

başarısız bir performans sergilemiştir. Elde edilen sonuçlar göz önüne alınarak, SCR oranının verime etkisinin parabolik bir yapıya sahip olduğu gözlemlenmiştir. Yani, kanatçık açıklığının artışı bir optimal değerden sonra verimi olumsuz etkilemektedir. Bunun sebebi bu optimal değerden sonra kanatçığın uç girdabın etkisini sönümleme oranının, kanatçığın artan yüzey alanının sürüklenme kuvvetini arttırma oranına göre düşük kalmasıdır. Bu çalışmada En uygun SCR oranı 0.75 olarak bulunmuş olsa da bu değer farklı kanatlarda ve farklı akış parametrelerinde değişiklik gösterebilir. Dolayısı ile belirli bir kanat için kanatçık tasarımı yapılırken bu optimal oran detaylı bir SCR oranı incelenmesiyle belirlenmesi gerektiği sonucuna varılmıştır.

Bir sonraki parametre olan kanatçık doğrultu yönü, toplamda üç farklı şekilde, yukarı, aşağı ve her iki tarafa da olmak üzere incelenmiştir. Diğer parametreler W4 kanadı ile aynı olmak koşuluyla aşağı doğru yönlendirilmiş ve her iki tarafa da yönlendirilmiş kanatçıklı kanatlar, sırası ile W6 ve W7 olarak kodlanmış ve analiz edilmiş ve sırası ile W6 ve W7 olarak kodlanmıştır. Analizler neticesinde W6 kanadı incelenen tüm kanatçıklı kanatlar arasında en az verim (C_L/C_D) artışını sağlayan kanat olmuştur. Ancak, kanatçıksız kanada göre C_D artışına sebebiyet vermemesiyle önemli bir özelliğe sahiptir. Bu özellik bir ayaklı teknede hali hazırda var olan kanada direkt olarak uygulanabilmesidir. Diğer kanatçıklar böyle bir durumda ayaklı teknenin daha fazla kaldırma kuvvetine ihtiyaç duymayacağı azami süratte seyir ederken fazladan sürüklenme kuvveti üreterek teknenin genel direncin artmasına ve hız kaybetmesine neden olacaktır. W6 ise azami sürat seyrinde bir kayba neden olmayacak bunun yanı sıra az da olsa kanat verimini arttırdığından, yani aynı sürüklenme kuvvetine karşılık daha çok kaldırma kuvveti üreteceğinden teknenin gövde seyrinden kanat seyrine geçiş hızını düşüreceği öngörülmüştür. W4 avantajının kullanılabilmesi için ise var olan kanat sökülerek, var olan kanatla aynı sürüklenme değerini verecek ancak verimi daha yüksek olduğu için daha fazla kaldırma kuvveti üretmesi, boyut olarak daha küçük ve ya hücum açısı daha küçük olan bir kanat kullanılmalıdır. Bu durumda gövde seyrinden kanat seyrine geçiş hızını W6 nın düşürdüğünden daha fazla düşüreceği öngörülmüştür. Farklı bir kanat tasarımı ile yine W4 kanatçıklı bir kanatın var olan kanatla değiştirilmesi ile kaldırma kuvveti katsayısı sabit tutularak direncin düşmesi sağlanıp, kavitasyon ve akım ayrılması olmaması koşulunda teknenin azami hızı arttırılabileceği öngörülmüştür. Diğer bir deyişle, W6 nın avantajı, daha düşük bir yatırım maliyeti ile tekne veriminin diğer kanatçıklara nazaran daha az olsa da arttırılabilme kapasitesidir. W7 kanadı ise temel kanatla karşılaştırıldığında %13.55 değerinde C_L artışı ile W4 kanadından daha çok kaldırma kuvveti sağlamaktadır. Ancak C_D de W4 kanadından %7.83 değeri ile daha çok artışa neden olmaktadır. Bu değerler neticesinde de C_L/C_D oranında W4 ün gerisinde kalarak %5.28 artış sağlayabildiği gözlemlenmiştir. Bu durum W4 kanadı ile W5 kanadının karşılaştırmasına benzer şekilde W7 kanadının da uç girdabın etkilerini daha iyi sönümlemesine rağmen geniş yüzey alanının sebep olduğu yüksek profil sürüklenme kuvvetinin C_L/C_D oranını olumsuz etkilediği sonucuna varılmıştır.

Son parametre olarak kanatçık izler kenarının çalıklık açısı β, 0^o ve 15^o olarak incelenmiştir. W4 ile karşılaştırılmak üzere, W8 olarak kodlanan $\beta=15^o$ olan ve diğer parametreleri W4 ile aynı olan kanatçıklı kanadın analizleri yapılmıştır. Analizler sonucunda W8 kanadının temel kanada göre sağladığı %11.93 C_L artışı, W4 kanadının gerisinde kalmıştır. Ancak sergilediği %6.78 C_L/C_D artışı W4 kanadından i sadece %0.03 daha fazladır. Bu değer geçerleme çalışmalarında belirtilmiş olan hata oranı göz önüne alınırsa geçersiz sayılabilecek kadar küçüktür. Bu iki kanadın iz

dağılımları ve basınç katsayısı dağılımları incelendiğinde, W8 kanadının daha az kavitasyon riskine sahip olması gibi bir avantajı olmasına rağmen daha bozuk bir iz dağılımına neden olması ve üretim bakımından daha karmaşık bir yapısı olması, W4 kanadına göre tercih edilebilmesini tartışmaya açık bırakmıştır.

1. INTRODUCTION

Since the beginning of 20th century, engineers and designers developed many types of hydrofoils attached under hull of ships in a purpose to gain enough lift force in order to elevate the ship's hull and eventually to evade from the great proportion of the resistance. Additionally, it has been realized that hydrofoils also improve seakeeping and maneuvering characteristics. Until the end of 80's this technology had drawn intense attention in commercial ferries and naval applications. By time the area of usage has changed and nowadays hydrofoils are generally preferred in sailing sector rather than naval and commercial ones. This is because of some drawbacks of the system such as high maintenance especially for ferries and the appearance of the preference of stealth instead of high speed in naval scope.

Meanwhile, in another industry, aviation; a considerably new application for lifting surfaces has erupted in the period between 50's and 90's. As a wingtip device, winglets have started to be used experimentally in the beginning, by now it is still a significant research field in advance. This small additional structure placed at the end of the wing provides considerably enhancement in performance of the wing.

Between 1975 and 1978, NASA has carried out parametric experimental studies on winglets in Langley Research Center that would become the headstones of the geometrical investigations of winglets (Whitcomb, 1976), (Heyson et al., 1977). There are some recent studies about determining the performances of some type of winglets under incompressible fluid conditions. Elhan and Tooren (2014), conducted a comparison of some various winglet geometries for commercial airplanes utilizing Vortex Lattice Method (VLM). Panagiotou et al. (2014), conducted a winglet design and optimization procedure for an unmanned aerial vehicle utilizing CFD for analyses of tapered winglets various in twist, cant and sweep angles. Azlin et al. (2011) investigated the effects in efficiency of semi –circular and elliptical winglets at different cant angles and different angles of attack utilizing CFD within subsonic airflow. Komerath et al. (2001), used experimental and numerical approaches to examine potential of multi-winglets. Guatham and Bibin (2016), also investigated

performances of multiple-winglets compared to some blended and BMAX winglets by using CFD. Gavrilovic et al. (2015), conducted a comperative numerical investigation of some kind of spiroid blended and wingtip-fence type winglets. Heyes and Smith (2005), investigated the effects of vortex generators to the tip vortex induced velocities and downwash when implemented near wingtip.

Interestingly, there are a small number of literatures about combination of these two improvements. Also, there are almost no practical examples of winglet mounted hydrofoils except a few hydrofoil racing sailboats.

1.1 Objective

The main objective of the thesis is to examine the comparative performance of the variations of the basic parameters of the simple tapered winglet types that can be added to the wing tips for the purpose of increasing wing efficiency in fully submerged underwater wings. In accordance with this principle, the most optimal parameter values are evaluated for various situations on the basis of the analysis of flow characteristics on the wing and wake area, based on the lift force, the drag force and the ratio of these forces which is mentioned as efficiency. It is intended to provide a literature for predicting the basic geometry to be used in the initial design in subsequent applications of a winglet in an existing wing or in the redesign of the wing with the winglet.

In accordance of this purpose, the forces acting, pressure and velocity isometries and wake characteristics of NACA0012 cross sectioned, 1m in chord length, 3m in half span foil which NACA0006 cross sectioned winglets of different shapes attached on the open tip with its' naked condition in a free stream are examined.

Except providing some verification data, all analyses performed with computational fluid dynamics (CFD). For simulating the turbulence, Reynolds Averaged Navier Stokes (RANS) model has been used due it's low cost in time-process resource with acceptable accuracy. Using DNS or LES would provide more accurate and reliable results. But, unfortunately the computer cluster system used, was not capable of operating DNS or LES for examined cases of this study.

2. WING THEORY & HYDROFOILS

2.1 3D Finite Wing Theory

On a three dimensional finite wing, lift over each segment does not correspond to what obtained from 2D analysis. This caused by the pressure difference between upper and lower sides of wing. Air flows from below the wing and out around the tip to the top of the wing in a circular fashion. An emergent circulatory flow pattern named vortex is observed, featuring a low-pressure core. Three-dimensional lift and the occurrence of wingtip vortices can be approached with the concept of horseshoe vortex and described accurately with the Lanchester–Prandtl theory. In this view, the trailing vortex is a continuation of the wing-bound vortex inherent to the lift generation. There is one wingtip vortex trailing from the left-hand wing and circulating clockwise, and another one trailing from the right-hand wing and circulating anti-clockwise. The result is a region of downwash behind the wing, between the two vortices. Consequently, downwash decreases the effective angle of attack. Thus lift coefficient decreases, also lift direction changes according to this changed angle of attack. Hence the real lift which is named as induced lift, becomes the component of changed lift which is perpendicular to original upstream direction and the component of the changed lift which is parallel to original upstream (named as induced drag) emerges as an added resistance (Breslin & Andersen, 1994).

There are several methods to calculate induced drag and induced lift such as Prandtl's lifting line method, Vortex Lattice method, Lifting Surface method and Panel method. Even it has some limitations Lifting Line method is the simplest one and sufficient for the wing geometries in this study.

2.1.1 Lifting line theory

The Prandtl Lifting Line Theory is a mathematical model that predicts lift distribution over a three-dimensional wing based on its geometry. According to the concept of circulation and the Kutta-Joukowski Theorem, the lift distribution function, the unknown effectively becomes the distribution of circulation over the

span, $\Gamma_{(y)}$. As the Helmholtz theorems stated, a vortex filament cannot begin or terminate in the fluid. As such, any span-wise change in lift can be modelled as the shedding of a vortex filament down the flow, behind the wing.

To derive the model, it is started with the assumption that the circulation of the wing varies as a function of the spanwise locations. The function assumed is a Fourier function. Firstly, the coordinate for the spanwise location y is transformed by y = s*cosθ , where y is spanwise location, and s is the semi-span of the wing.

The circulation is assumed to be:

$$\Gamma_{(y)} = \Gamma_{(\theta)} = \gamma = 4sV_\infty \sum_{n}^{\infty} A_n \sin(n\theta) \tag{2.1}$$

Here, A_n represents the Fourier function coefficient. Lift coefficients related to circulation and angle of attack are given in Eq. (2.2) and Eq. (2.3).

$$Cl = \frac{2\gamma}{V_\infty c} \tag{2.2}$$

$$Cl = Cl_\alpha(\alpha_\infty + \alpha_{geo} - \alpha_0 - \alpha_i) \tag{2.3}$$

Here, c is sectional chord length, Cl_α is 2-D sectional lift coefficient and α_∞, α_{geo}, α_0, α_i are the angle between coordinate system and incoming velocity vector, geometric angle of attack, zero-lift angle of attack and induced angle of attack respectively. Hence, the vortex strength in any particular spanwise station can be given by the equation below.

$$\gamma = 0.5V_\infty c Cl_\propto(\alpha_\infty + \alpha_{geo} - \alpha_0 - \alpha_i) \tag{2.4}$$

This one equation has two unknowns: the value for γ and the value for α_i . However, the downwash is merely a function of the circulation only. So we can determine the value α_i in terms of $\Gamma_{(y)}$, bring this term across to the left hand side of the equation and solve. The downwash at any given station is a function of the entire shed vortex system. This is determined by integrating the influence of each differential shed vortex over the span of the wing (Anderson, 2001).

Differential element of circulation:

$$d\Gamma = 4sV_\infty \sum_{n=1}^{\infty} nA_n \sin(n\theta) \tag{2.5}$$

Differential downwash due to differential element of circulation:

$$d\omega_i = \frac{d\Gamma}{4\pi r} \tag{2.6}$$

Downwash at a particular location:

$$\omega_i = \int_{-s}^{s} \frac{1}{y - y_0} d\Gamma \tag{2.7}$$

Another expression of Eq. (2.7) is given as Eq.(2.8).

$$\omega_i = V_\infty \sum_{n=1}^{\infty} \frac{nA_n \sin(n\theta)}{\sin\theta} \tag{2.8}$$

Eq. (2.9) represents the change in angle of attack.

$$\alpha_i = \sin^{-1}\left(\frac{\omega_i}{V_\infty}\right) \cong \frac{\omega_i}{V_\infty} \; (small\ angles) \tag{2.9}$$

By substituting Eq. (2.8) and Eq. (2.9) into RHS of Eq. (2.4) and Eq. (2.1) into the LHS of Eq. (2.4), we then get:

$$4sV_\infty \sum_{n=1}^{\infty} A_n \sin(n\theta) = 0.5V_\infty c Cl_\propto \left[\alpha_\infty + \alpha_{geo} - \alpha_0 - \sum_{n=1}^{\infty} \frac{nA_n \sin(n\theta)}{\sin\theta}\right] \tag{2.10}$$

After rearranging, we get the series of simultaneous equations:

$$\sum_{n=1}^{\infty} A_n \sin(n\theta) \left(\sin(\theta) + \frac{nCl_\alpha c}{8s}\right) = \frac{Cl_\alpha c}{8s} \sin(\theta)(\alpha_\infty + \alpha_{geo} - \alpha_0) \tag{2.11}$$

Finally, lift force, lift coefficient, induced drag force and induced drag coefficient of entire wing are stated as Eq. (2.12), Eq. (2.13), Eq. (2.14), Eq. (2.15) respectively.

$$L = \rho V_\infty \int_{-s}^{s} \Gamma dy \tag{2.12}$$

$$CL = \pi AR A_1 \tag{2.13}$$

$$D_i = \rho V_\infty \int_{-s}^{s} \Gamma \sin(\alpha_i)\, dy \tag{2.14}$$

$$CD_i = \pi AR \sum_{n=1}^{\infty} nA_n^2 = \frac{CL^2}{\pi AR}\left[1 + \frac{\sum_{n=2}^{\infty} nA_n^2}{A_1^2}\right] = \frac{CL^2}{\pi ARe} \tag{2.15}$$

where,

$$\delta = \frac{\sum_{n=2}^{\infty} nA_n^2}{A_1^2} \tag{2.16}$$

$$e = \frac{1}{1 + \delta} \tag{2.17}$$

Here, e is the span efficiency factor (Katz and Plotkin, 1991) and AR is the aspect ratio of the wing. For a symmetric wing, the even terms of the series coefficients are identically equal to 0, and so can be dropped. In Figure 2.1, the relation between downwash, induced angle of attack and induced forces on a wing section is depicted. In Figure 2.2, a simple visualization of differential vortex shedding system over span of a wing is presented.

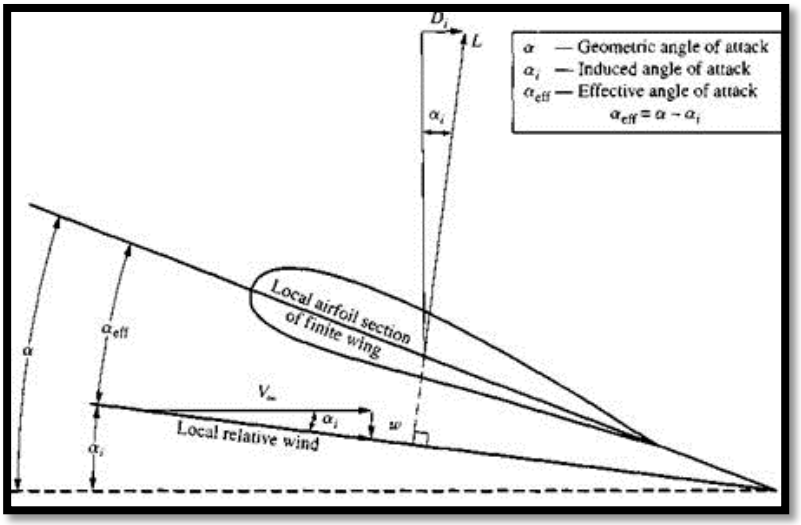

Figure 2.1: Downwash effect on a wing section.

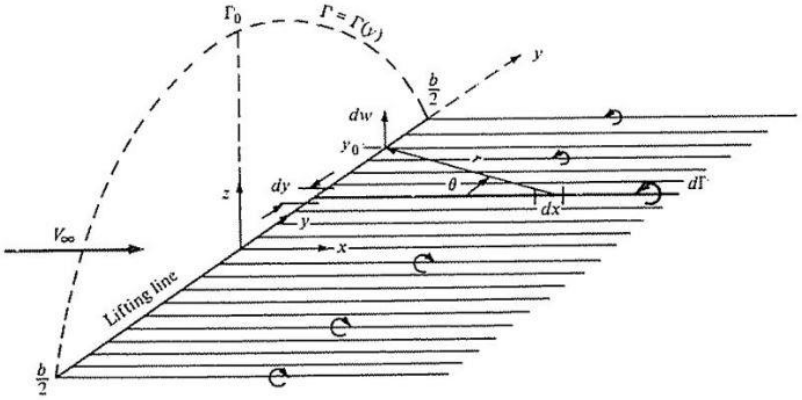

Figure 2.2: Superposition of an infinite number of horseshoe vortices along a lifting line.

2.2 Hydrofoil Vessels

Hydrofoil vessels are ships or boats with underwater wings attached beneath their hulls. Their principle is based on elevating the whole hull of the vessel above free surface at high speeds by the lift force created via wings remained under water and evading the viscous and most importantly wave resistance of the hull. Swa, the vessel can cruise at a higher speed with the same power or with lesser power at the same speed in foilborne condition. Additionally, evading incoming waves provides much better seakeeping characteristics which means a smooth comfortable cruise (Faltinsen, 2005).

After first prototypes like inventor Forlanini's boat (max speed 27 kn), Thornycroft's Miranda IV (max speed 35kn) and Bel's HD-4 (max speed 42kn) which are constructed with ladder type hydrofoils; successor vessels mainly designed with two types of hydrofoils which are v-shaped surface piercing and reverse T-shaped fully submerged (Figure 2.3).

Surface piercing type hydrofoils are easy to construct and operate however, they have lower efficiency compared to fully-submerged ones. They have self-stabilizing attribute in roll and pitch motions but have more resistance and lift-free regions due to occurrence of spray and ventilation at surface-piercing areas.

Fully submerged hydrofoils are less subjected to the effects of wave action, and, therefore, more stable at sea and more comfortable for crew and passengers. Also they have higher lift/drag ratio by having no ventilating areas. Albeit, they need

control process performed by sensors, a computer, and active flaps on trailing edge of wings. Thus, they have more fragile structure and require more maintenance.

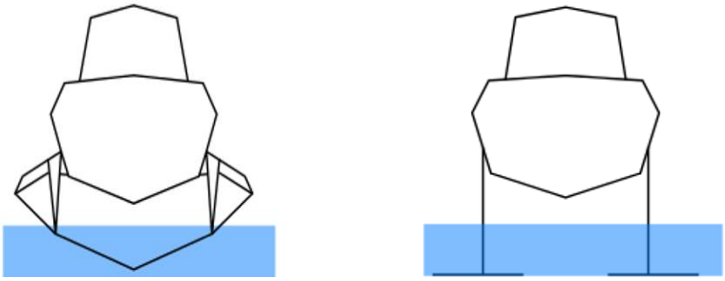

a) b)

Figure 2.3: Hidrofoil types a) Surface piercing b) Fully submerged.

As well as in military and commercial application, hydrofoils are also being used on sail boats. A French sail powered Hydroptére set new sailcraft world speed record in the 500m category wth a speed of 51.36 knots in September 2009. One military and one commercial vessel are presented in Figure 2.4 as examples.

Beside ships and boats, hydrofoils are attached to some entertainment gadgets like windsurfs and wakeboards.

Some notable hydrofoil vessels are:

- Freccia d'Oro "PT10" (passenger boat, 35 knots)
- Voskhod class (passenger boat, 32 knots)
- Boeing 929 (passenger boat, 43 knots)
- VS-6 (minelayer, 47 knots)
- HMCS Bras d'Or (submarine hunter, 63 knots)
- Pegasus class (fast patrol boat, 48 knots)
- Sarancha class (missile boat, 58 knots)
- Sparviero class (missile boat, 50 knots)
- Turya class (torpedo boat, 40 knots)

a) b)

Figure 2.4: a) HMCS Bras d'Or, b) Voskhod.

2.3 Winglets

Winglets have been used in aviation widely in order to increase efficiency of aircraft wings. The basic principle behind these devices is reducing induced drag and lift deduction due to the wingtip vortices by shifting the vortices away from the wing, hence lowering the negative effect on the main lifting surface (Figure 2.5).

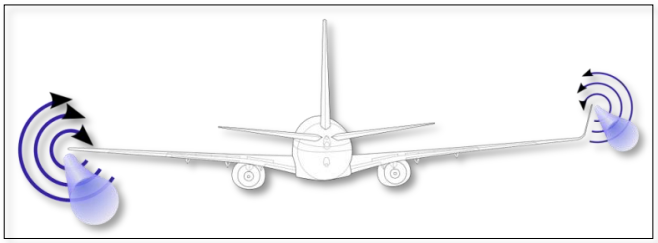

Figure 2.5: Tip-vortices without and with winglet.

Winglets are firstly inspired from wing tip feathers of eagles. The pioneer of the concept was Frederick W. Lanchester who patented wing-end-plates as a method for controlling wingtip vortices in 1897. Afterwards the first functional winglets installed to several monoplanes and biplanes by William E. Somerville. Following the end of World War II, Sighard F. Hoerner was a pioneer researcher in the field, having written a technical paper published in 1952 that called for drooped wingtips. Drooped wingtips are often called "Hoerner tips" in his honour.

NASA's first approach about winglets was the design study of Richard T. Whitcomb (Langley Research Center, 1976). Whitcomb's designs were flight-tested in 1979–80 by a joint NASA/Air Force team, using a KC-135 Stratotanker, a Lockheed L-1011, McDonnel Douglas DC-10.

Also in business aviation, Learjet and Gulfstream Aerospace engendered their prototypes with winglets. After the test flights of Learjet 28, Learjet informed that winglets provided increased range by about 6% and also improved directional stability.

As an independent designer, Burt Rutan has incorporated winglets in his composite aircrafts since 1975. One of his designs 'Rutan Voyager' achieved to be the first aircraft circumnavigate the world without refueling in 1986.

Airline jet producer companies like Boeing and Airbus started to employ winglet in 80's in various types. Some mainstream types are NASA(conventional) type,

blended type, fence type or combined. Visuals of some most used types of winglets are presented in Figure 2.6 and Figure 2.7.

a) b)

Figure 2.6: a) Conventional winglet on KC-135 Stratotanker, b) Blended winglet on Boeing 737.

a) b)

Figure 2.7: a) Fence winglet on Airbus A319, b) Combined winglet (blended&fence) on Boeing 737 MAX.

3. COMPUTATIONAL FLUID DYNAMICS

3.1 Numerical Solution Methods and Governing Equations

CFD analyses are based on the solution of the Navier-Stokes equations, which imply esentially conservation of mass, conservation of momentum, and conservation of energy. Flow of water is usually incompressible and flow of air at low speed (M< 0.3) is assumed to be incompressible. Thus, incompressible conservation of mass is written as

$$\frac{\partial U_i}{\partial x_i} = 0 \tag{3.1}$$

in Einstein notation where U_i denotes velocity components.

The general form of conservation of momentum (Cauchy equation) is;

$$\rho \frac{\mathrm{D}U_i}{\mathrm{Dt}} = \rho g_i + \frac{\partial \tau_{ij}}{\partial x_j} \tag{3.2}$$

Where g_i is the body force components (e.g gravity) and $\boldsymbol{\tau}_{ij}$ is the stress tensor which is related to velocity gradient using the following constitutive equation for newtonian fluids;

$$\tau_{ij} = -p\delta_{ij} + \mu\left(\frac{\partial U_i}{\partial x_j} + \frac{\partial U_j}{\partial x_i}\right) \tag{3.3}$$

where p is pressure and μ is coefficient of viscousity.

When Eq.(3.3) implemented in Eq.(3.2) with the assumption of constant viscousity (constant temperature field), the obtained equation is N-S equation for incompressible flow of newtonan fluids with constant viscosity in vectorial notation:

$$\rho \frac{D\vec{V}}{Dt} = \rho\vec{g} - \nabla p + \mu\nabla^2\vec{V} \tag{3.4}$$

where $\vec{V}$ is the velocity vector.

Because of high non-linearities of N-S equations, analytic solution is mostly impossible or impractical. Thus, numerical methods are being utilized to get results. In order to be solved numerically, N-S equations should be discretizated. There are plenty of methods for discretisation; finite elements, finite difference or finite volume. (Ferziger-Peric, 2002). In CFD field, using finite volume method is common for discretisation.

3.1.1 Finite volume discretisation

Obtaining the transport equations that simulate fluid flow, in conservative form of differential equations is possible by taking an infinitely small, fixed element and calculating momentum transfers through all its surfaces (Anderson 1996). Finite volume discretisation based on the integration of these equations for a finite volume. In Cartesian tensor notation, the discretisation process for a transport property of flow Φ (e.g. temperature) on convection and diffusion equations can be predicated as Eq. (3.5) (Johnson 1998).

$$\rho\frac{\partial\phi}{\partial t}+\rho\frac{\partial(U_j\phi)}{\partial x_j}=\frac{\partial}{\partial x_j}\left(\Gamma\frac{\partial\phi}{\partial x_j}\right)+S \tag{3.5}$$

U, Φ, Γ, and S represent; velocity in 3 components, a transport property of flow, diffusion coefficient and source term, respectively. If Eq. (3.5) is written in one dimension and steady form, it would be as Eq. (3.6).

$$\rho\frac{d(U\phi)}{dx}=\frac{d}{dx}\left(\Gamma\frac{d\phi}{dx}\right)+S \tag{3.6}$$

Hence , Eq.(3.6) integrated along a control volume (Figure 3.1) , in assumption of equivalence of the inlet and outlet surfaces (A_e=A_w=1).

$$\int_w^e \rho\frac{d}{dx}(U\phi)dx=\int_w^e\left[\frac{d}{dx}\left(\Gamma\frac{d\phi}{dx}\right)+S\right]dx \tag{3.7}$$

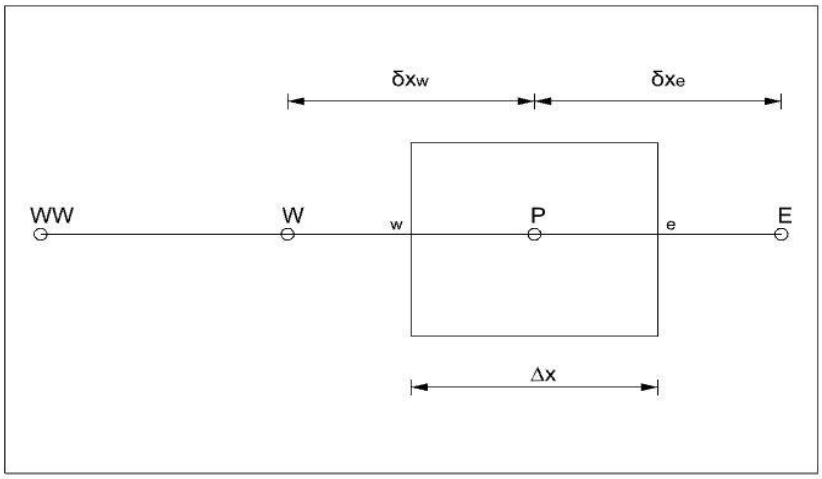

Figure 3.1: Computational Control Volume.

The integrals LHS and RHS of the equation will become as stated below.

$$\text{LHS} = (\rho U\phi)_e - (\rho U\phi)_w \tag{3.8}$$

$$\text{RHS} = \left(\Gamma \frac{d\phi}{dx}\right)_e - \left(\Gamma \frac{d\phi}{dx}\right)_w + S_U + S_p\phi_p \tag{3.9}$$

Here, S_U is the constant, which is based on the source term and, S_P is the coenstant of the variable that is dependant to S_U. Diffusion terms are commonly interpolated by central difference. When central difference utilized, the first component of RHS becomes as stated below.

$$\left(\Gamma \frac{d\phi}{dx}\right)_e = \Gamma\left(\frac{\phi_E - \phi_P}{\delta x_e}\right)_w \tag{3.10}$$

There are several discretisation diagrams for convective terms such as, first order upwind central difference, QUICK (Quadratic Upwind Interpolation for Convective Kinematics) (Versteeg – Malalasekera, 1995), MUSCLE (Monoton Upstream-Centered Schemes for Conservation Laws) (Blazek, 2001) and some other hybrid types (Hoffmann – Chiang, 2000). For instance, if "second order upwind" interpolation diagram with assumption $\delta x_e = \delta x_w = \delta x$, scrutinized, Φ values on surfaces can be denoted as Eq. (3.11) and (3.12).

$$\phi_e = \frac{3}{2}\phi_P - \frac{1}{2}\phi_W + O((\Delta x)^2) \tag{3.11}$$

$$\phi_w = \frac{3}{2}\phi_W - \frac{1}{2}\phi_{WW} + O((\Delta x)^2) \tag{3.12}$$

If these Φ values are implemented in Eq (3.8) and (3.9),

$$(\rho U)_e\left(\frac{3}{2}\phi_P - \frac{1}{2}\phi_W\right) - (\rho U)_w\left(\frac{3}{2}\phi_W - \frac{1}{2}\phi_{WW}\right) = \frac{\Gamma}{\delta x}(\phi_E - 2\phi_P + \phi_W) + S_U + S_P\phi_P \tag{3.13}$$

is attained . Hence, lastly Eq(3.14) would be found.

$$a_P\phi_P = a_W\phi_W + a_E\phi_E - a_{WW}\phi_{WW} + S_U = \sum_{km} a_{km}\phi_{km} + S_U \tag{3.14}$$

The index of 'km' represents adjacent volumes to volume P. This equation system is feasible for an iterative solution method like Gauss-Seidel (Hoffmann–Chiang, 2000).

3.1.2 N-S discretisation and SIMPLE algorithm

N-S Equations are also discretizable by finite volume method similar to transport equations. To procure this similarity, Φ=1 (unity) and S=0 for conservation of mass as Eq. (3.1). Φ=Ui (velocity) and Γ=μ (viscosity) for momentum equations in Eq (3.16).

$$\rho\frac{\partial U_i}{\partial t} + \rho\frac{\partial(U_jU_j)}{\partial x_j} = -\frac{\partial P}{\partial x_i} + \frac{\partial}{\partial x_j}\left(\mu\frac{\partial U_i}{\partial x_j}\right) \tag{3.15}$$

In solution of transport equations, the velocity components on surfaces of control volume are assumed to be known. However, in N-S equations velocity and pressure values are unknown and purposed to be attained as outputs. Furthermore, there is no other equation to estimate pressure. In order to overcome this dilemma, an algorithm called SIMPLE (Semi-Implicit Method for Pressure-Linked Equations) (Patankar and Spalding, 1972), and some other algorithms like SIMPLER (SIMPLE-Revised), SIMPLEC (Semi-Implicit Method for Pressure Linked Equations-Consistent) (Van Doormall and Raithby, 1984) and PISO (Pressure Implicit with Split Operator) (Issa, 1986), which are using auxillary equation as an indirect pressure solver, have been developed.

Placing the pressure and velocity point in the center of the control volume causes oscillations at pressure field. By the way, if the term of $-(\delta P/\delta x)$ which exists in x component of momentum equation is integrated along the control volume in Figure

3.1. Then, central differences are taken in account by assuming, $\delta x_e = \delta x_w = \delta x$, Eq. 3.16 will be obtained.

$$\int_{w}^{e} -\frac{dP}{dx}dx = -(P_e - P_w) = -\left(\frac{P_E + P_P}{2}\right) + \left(\frac{P_P + P_W}{2}\right) = \left(\frac{P_W - P_E}{2}\right) \tag{3.16}$$

Under these conditions, if P_W, P_P and P_E points have values like 100, 50, and 100 respectively; the gradient at point P will wrongly equal to zero. To avoid this, a shifted web layout is used as a pressure correcting technique (Patankar, 1980). A shifted one dimensioned control volume is shown in Figure 3.2. When the pressure gradient $-\left({}^{dP}/_{dx}\right)$, is integrated along the control volume with the center 'i', Eq. (3.17) is procured.

$$-\int_{\Delta V_i} \left(-\frac{dP}{dx}\right)_i dx = P_{I-1} - P_I \tag{3.17}$$

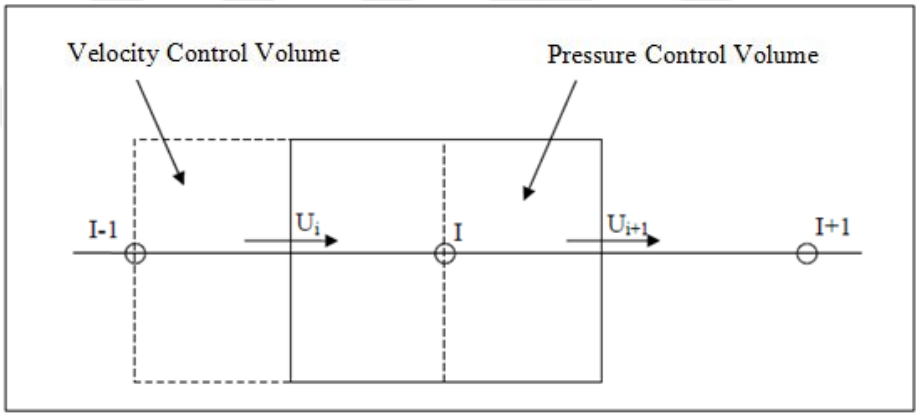

Figure 3.2 : Shifted control volume.

Hence, if one dimensional momentum equation is discretized with the indeces depicted in Figure 3.2 considering the inlet and outlet surfaces have unit size, the convective term, diffusion term and pressure term will become as Eq. (3.18), Eq. (3.19) and Eq. (3.20) respectively.

$$\int_{\Delta V_i} \frac{d}{dx}(\rho U\phi)dx = [(\rho U\phi)_I - (\rho U\phi)_{I-1}] \tag{3.18}$$

$$\int_{\Delta V_i} \frac{d}{dx}\left(\mu\frac{d\phi}{dx}\right)dx = \mu\left(\frac{\phi_{i+1} - \phi_i}{\delta x_I} - \frac{\phi_i - \phi_{i-1}}{\delta x_{I-1}}\right) \tag{3.19}$$

$$-\int_{\Delta V_i} \frac{dP}{dx} dx = (P_{I-1} - P_I) \tag{3.20}$$

A suitable discretisation diagram should be applied to Φ value as velocities on control volumes surface in convective term (which described in previous sub-topic). Eq. (3.21) will be attained by placing the terms on the same point and replacing Φ with U.

$$a_i U_i = a_{i-1} U_{i-1} + a_{i+1} U_{i+1} + (P_{I-1} - P_I) = \sum_{km} a_{km} U_{km} + (P_{I-1} - P_I) \tag{3.21}$$

In order to acquire the pressure values correctly, correction formulas for pressure and velocity magnitudes are required. Symbolising the uncorrected values with upper index " * " and corrections with upper index" ' ", velocity (U) and pressure (P) can be written as stated below.

$$U = U^* + U' \tag{3.22}$$

$$P = P^* + P' \tag{3.23}$$

Hence, terms of momentum equation will be written as Eq. (3.24) and Eq.(3.25).

$$a_i U_i^* = \sum_{km} a_{km} U_{km}^* + (P_{I-1}^* - P_I^*) \tag{3.24}$$

$$a_i U_i' = \sum_{km} a_{km} U_{km}' + (P_{I-1}' - P_I') \tag{3.25}$$

With a simplifying purpose $\sum_{km} a_{km} U_{km}'$ terms in the equations are neglected in SIMPLE algorithm. Hence, the formula of velocity correction value becomes as Eq. (3.26).

$$U_i' = \frac{(P_{I-1}' - P_I')}{a_i} \tag{3.26}$$

While, to find P' values, it is needed to discretize the continuity equation in control volume which has the pressure center in the middle. The continuity equation (with unit size of inlet and oulet surfaces of control volume) becomes as Eq. (3.27).

$$(\rho U')_{i+1} - (\rho U')_i + (\rho U^*)_{i+1} - (\rho U^*)_i = b_I' \tag{3.27}$$

Here, b_I' represents the continuity error. When this term becomes zero in iterations convergence is satisfied. If U' values provided from momentum equation are substituted in Eq. (3.28), it evolves to pressure correction equation. Eq. (3.28).

$$a_i P_i' = \sum_{km} a_{km} P_{km}' + b_I' \tag{3.18}$$

Briefly, general formulas for velocities and pressures are demonstrated as Eq. (3.29) and Eq. (3.30).

$$U_i = U_i^* + \frac{(P_{I-1}' - P_I')}{a_i} \tag{3.29}$$

$$P_I = P_I^* + P_I' \tag{3.30}$$

3.2 Turbulence Solver Methods and Models

3.2.1 DNS

Direct Numerical Simulation (DNS) is a computational analysis method which solves N-S equations directly without any turbulence modelling. It provides result with a great precision, fairly better accuracy than other methods. The reason of this, even extremely small eddies are being able to account for the solution. Therefore, cases, which are hard to construct an experimental set up, can be investigated with DNS. In fact, DNS provides an opportunity to avoid several uncertainties due to the experiment environment with only adding truncation and rounding errors. Thus, in some situations, DNS may provide more accurate findings than experiments. DNS, uses a very small length unit which is called Kolmogorov length scale (η).

$$\eta = \left({}^{\upsilon^3}/_{\varepsilon} \right)^{1/4} \tag{3.31}$$

Where, ν is the kinematic viscousity and ε is the rate of kinetic energy dissipation. If it is denoted that; length of the solution mesh in any direction is L, the number of vertices is N and the distance between vertices in the same direction is h. Eq. (3.32) and Eq. (3.33) should be satisfied in order to perform DNS solver.

$$N.h > L \tag{3.32}$$

$$h \leq \eta \tag{3.33}$$

The previous relations imply that a three-dimensional DNS requires a number of mesh points N^3 satisfying Eq. (3.34).

$$N^3 \geq Re^{9/4} \tag{3.34}$$

Hence, the memory storage requirement in a DNS grows very fast with the Reynolds number. In addition, given the very large memory requirement, the integration of the solution in time must be doneby an explicit method. This means that in order to be accurate, the integration, for most discretization methods, must be done with a time step, Δt, small enough such that a fluid particle moves only a fraction of the mesh spacing h in each step.

$$C = \frac{\Delta t . u'}{h} < 1 \tag{3.35}$$

C is here the Courant Number and u' is root mean square of velocity.The total time interval simulated is generally proportional to the turbulence time scale τ

$$\tau = \frac{L}{u'} \tag{3.36}$$

Combining these relations, and the fact that h must be of the order of η, the number of time-integration steps must be proportional to $(L/C\eta)$. On the other hand it leads to Eq. (3.37).

$$\frac{L}{\eta} \sim Re^{3/4} \tag{3.37}$$

The number of time steps grows also as a power law of the Reynolds number. Consequently, the computational cost of DNS grows as Re^3. Unfortunately, the requirements of high Re flows would exceed the capacity of even most powerful computers currently available (Moin and Mahesh, 1998).

3.2.2 LES

Large Eddy Simulation (LES), is proposed by Smagorinsky in 1963. The main objective of LES is to eliminate the computational burden of small eddies which make DNS nearly impossible to compute. By applying a low-pass filter to N-S equations, small eddies in the flow is ignored. Then, the effect of small eddies

reconsidered by Sub-Grid-Scale (SGS) model. Filtering formula can be expressed as mentioned below

$$\bar{\Phi}(x,t) = \int G\,(x,x',\Delta)\Phi(x',t)dx' \tag{3.38}$$

$$\Phi = \bar{\Phi} + \Phi' \tag{3.39}$$

Here, $\bar{\Phi}$ is filtered magnitude of velocity or pressure, Φ' is the magnitude of velocity or presuure which is calculated from SGS, G is filtering function, Δ is filter criteria (eddies smaller than criteria taken account by applying SGS).

In the sequel, filtered pressure and velocity are implemented in Navier-Stokes equations; Eq. (3.40) and Eq. (3.41) are obtained.

$$\frac{\partial(\rho\bar{u}_i)}{\partial x_i} = 0 \tag{3.40}$$

$$\frac{\partial(\rho\bar{u}_i)}{\partial t} + \frac{\partial\left(\rho\overline{u_i u_j}\right)}{\partial x_j} = -\frac{\partial\bar{p}}{\partial x_i} + \frac{\partial\left(\overline{\tau_{ij}} + \tau_{ij}^{s}\right)}{\partial x_j} \tag{3.41}$$

$$\overline{\tau_{ij}} = \mu\left(\frac{\partial\bar{u}_i}{\partial x_j} + \frac{\partial\bar{u}_j}{\partial x_i}\right) \tag{3.42}$$

where, $\overline{\tau_{ij}}$ is the filtered stress tensor and τ_{ij}^{s} is sub-grid scaled Reynolds stress (Deardorff, 1970). There are several SGS models in literature. Some widely known ones of them are:

There are several SGS models in literature. Some widely known ones of them are;

- Smagorinsky-Lilly
- Germano-Dynamic
- WALE(Wall Adapted Local Eddy Viscosity)
- Dynamic Kinetic Energy TGransport

LES gives the possibility to analyse high Reynolds numbered flows with a little renunciation from accuracy and precision when compared to DNS. Even so, also LES requires very intense grid and naturally to much “process-power * time” resource. Therefore, the required time for a complex analysis, using clusters which have moderate process-power, would be unacceptable.

3.2.3 RANS

Reynolds Averaged Navier Stokes is a mathematical turbulent flow solver method which based on Reynolds Decomposition of Navier-Stokes equations. Although it is remarkably less accurate than LES and DNS, currently the most prefered method in CFD, due to its much more affordable requirement of "process-power*time" resource. Reynolds Decomposition is a mathematical technique Eq. (3.43) to separate the average and fluctuating parts of a quantity which is proposed by Osbourne Reynolds in 1895.

$$\Phi(x,y,z,t) = \overline{\Phi(x,y,z,t)} + \Phi'(x,y,z,t) \tag{3.43}$$

Where, $\overline{\Phi}$ denotes the time average of Φ, and Φ' fluctuating part. Eq. (3.44) mentions N-S equations which Reynolds decomposed velocity and pressure magnitudes, implemented in (Tennekes and Lumley, 1972).

$$\frac{\partial(\rho\bar{u}_i)}{\partial x_i} = 0 \tag{3.44}$$

$$\frac{\partial(\rho\bar{u}_i)}{\partial t} + \frac{\partial\left(\rho\overline{u_i u_j}\right)}{\partial x_j} = -\frac{\partial\bar{p}}{\partial x_i} + \frac{\partial\left(\overline{\tau_{ij}} + \tau_{ij}^R\right)}{\partial x_j} \tag{3.45}$$

Here, τ_{ij}^R is Reynolds stress function which is expressed via Boussinesq approximation below.

$$\tau_{ij}^R = -\rho\overline{u_i u_j} = 2\mu_t S_{ij} - \frac{2}{3}\rho k\delta_{ij} \tag{3.46}$$

$$S_{ij} = 0.5\left(\frac{\partial\bar{u}_i}{\partial x_j} + \frac{\partial\bar{u}_j}{\partial x_i}\right) \tag{3.47}$$

$$k = \left(u'^2 + v'^2 + w'^2\right)/2 \tag{3.48}$$

S_{ij}, μ_t, and k denote average shear stress scale, eddy viscosity, and turbulence kinetic energy, respectively. Due to the presence of Reynolds stress τ_{ij}^R which contains 9 unknown parameters, RANS equations is not possible to be solved without turbulence models.

There are several turbulence models developed implemented with RANS. Some widely used ones are stated as:

- Spalart–Allmaras model
- standard k–ε model

- realizable k–ε model
- standard k–ω model
- k – ω SST(Shear-Stress-Transport) model

3.2.3.1 k - ω standard and k - ω SST models

Kolmorov has developed a differential equation for variable "ω" which represents the dissipation magnitude per unit kinetic energy instead, the variable "ε" which modelled from a fairly complex turbulence dissipation transport equation. For a period, the equation of "ω" remodelled and formed several times. Eventually, the model took place in literature as Standard k–ω model. The advantage of k–ω model than k–ε model, is the ability to show a better performance in simulating the velocity and turbulence profiles and determination of pressure gradient and flow seperations (Wilcox, 1988a).

Even though, standard k–ω model provides a particular solution in boundary layer, it is realized that the model calculates shear stress excessively (Menter, 1992a).

Menter states that, the erroneous results arise from the viscosity definition in flows with reverse pressure gradient (Menter, 1993). In his study, he developed a clever trick for viscosity calculation and prevented the shear stress to surpass the "Bradshaw Constant (k)" of 0.3.

Another enhancement Menter applied, was based on the idea of using k–ω model in boundary layer but k–ε model in shear-free flow regions. In order to actualise this, he included a cross-diffusion term in to "ω" transport equation. Basic two equations of this model are Eq. (3.49) and Eq (3.50) (Menter, 1993).

$$\frac{\partial \mathrm{k}}{\partial \mathrm{t}} + \frac{\partial}{\partial \mathrm{x_j}}\left(\mathrm{kU_j}\right) = \frac{P}{\rho} - \beta_\mathrm{k}\omega\mathrm{k} + \frac{\partial}{\partial \mathrm{x_j}}\left[\left(\upsilon + \sigma_\mathrm{k}\upsilon_\mathrm{t}\right)\frac{\partial \mathrm{k}}{\partial \mathrm{x_j}}\right] \tag{3.49}$$

$$\frac{\partial \omega}{\partial \mathrm{t}} + \frac{\partial}{\partial \mathrm{x_j}}\left(\omega\mathrm{U_j}\right) = \frac{\gamma P}{p\upsilon_\mathrm{t}} - \beta\omega^2 + \frac{\partial}{\partial \mathrm{x_j}}\left[\left(\upsilon + \sigma_\omega\upsilon_\mathrm{t}\right)\frac{\partial \omega}{\partial \mathrm{x_j}}\right] + 2(1-\mathrm{F_1})\sigma_{\omega 2}\frac{1}{\omega}\frac{\partial \mathrm{k}}{\partial \mathrm{x_j}}\frac{\partial \omega}{\partial \mathrm{x_j}} \tag{3.50}$$

where;

$$\upsilon_\mathrm{t} = \frac{\alpha_1 k}{\max(\alpha_1\omega, SF_2)} \tag{3.51}$$

$$S = \sqrt{S_{ij}S_{ji}} \tag{3.52}$$

$$F_1 = \tanh(arg_1^4) \tag{3.53}$$

$$arg_1 = min\left[max\left(\frac{\sqrt{k}}{\omega y \beta_k}, \frac{5oov}{y^2\omega}\right), \frac{4k\sigma_{\omega 2}}{CD_{k\omega}d^2}\right] \tag{3.54}$$

$$CD_{k\omega} = max\left(\frac{2\sigma_{\omega 2}}{\omega}\frac{\partial k}{\partial x_i}\frac{\partial \omega}{\partial x_j}, 10^{-10}\right) \tag{3.55}$$

$$F_2 = \tanh(arg_2^2) \tag{3.56}$$

$$arg_2 = max\left(\frac{\sqrt{k}}{\omega y \beta_k}, \frac{5oov}{y^2\omega}\right) \tag{3.57}$$

$$P = min\left(\tau_{ij}\frac{\partial u_i}{\partial x_j}, 10k\omega\beta_k\right) \tag{3.58}$$

3.3 Wall Function

By secession, normal from wall surface, the rate of turbulent kinetic energy arises rapidly due to high velocity gradients. Henceforth, it is essential to obtain a precise numerical solution in boundary layer where shear stress has the main role in emerging vorticity and turbulence (Ünal, 2007). In this region, while the flow is substantially influenced by viscous forces, it is independent from freestream parameters. The wall shear stress (τ_w), due to laminar or turbulent flow, is used in defining friction velocity (u_t):

$$u_t = \sqrt{\frac{\tau_w}{\rho}} \tag{3.59}$$

'The Wall Function' is defined as

$$U^+ = f(y^+) \tag{3.60}$$

where, U^+ is the dimensionless velocity gradient:

$$U^+ = \frac{U}{u_t} \tag{3.61}$$

and y^+ is dimensionless distance from wall surface.

$$y^+ = \frac{\rho u_t y}{\mu} \tag{3.62}$$

The turbulent region is divided in two sections called inner and outer range. Inner range also is split up into two sections called logarithmic region and viscous sub-layer (Wilcox, 1994; Ünal et al, 2012).

In the region $y^+ \leq 5$, the viscous sub-layer is very thin, thus Eq. (3.60) can be expressed as:

$$U^+ = y^+ \qquad \text{if} \quad y^+ \leq 5 \tag{3.63}$$

Logarithmic region which corresponds to $30 < y^+ \leq 500$, the fluid influenced by merely turbulence itself. In this region the relation between U^+ and y^+ becomes as:

$$U^+ = \frac{lny^+}{\kappa} + C \qquad \text{if} \quad 30 < y^+ \leq 500 \tag{3.64}$$

According to experimental investigations, the von Karman costant κ is approximately taen as 0.41 and the costant C is approximately taken as 5 for smooth surfaces (Schlichting and Gersten, 2000).

In the transition region, $5 < y^+ \leq 30$, the flow characteristic can be switched between turbulent and laminar. Thus, if y+ applied in this region, results of analyses would be unstable and unreliable.

4. COMPUTATIONAL STUDY

4.1 Computational Model

For defining the the parameters examined in this study, some abbreviations are used. The root chord length of winglet was defined as “Cwr”; the chord length of rectangular main wing is defined as “Cmw”, the span length of winglet is denoted as “Sw”; the tip chord length of winglet is denoted as “Cwt”; the swep angle of winglets trailing edge is denoted as “Θ” and the cant angle of winglet is denoted as “ψ”. The winglet geometry parameters to be examined for comparison in this study are basically the ratio of Cwr/Cmw which is denoted as “CCR”and the ratio of Sw/Cmw which is denoted as SCR. First, CCR was examined. Then SCR was examined based on the wing with the most efficient CCR. After selecting the most efficient values of these two parameters, the effects of the direction of winglet and the trailing edge sweep angle were investigated separately. Measures and angles are explained in Figure 4.1.

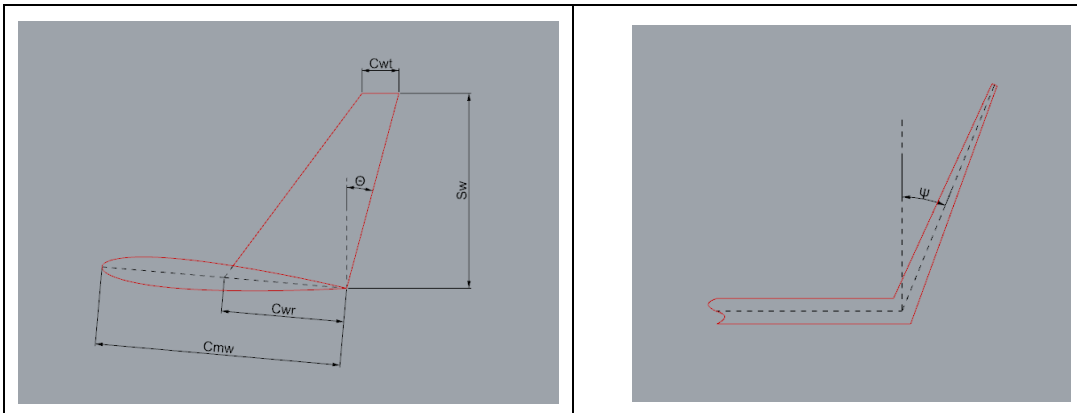

Side View	Front View

Figure 4.1: Main dimensions of winglet geometry.

4.1.1 Selection of main wing geometry

The preferred requirements are regarded below in selecting the geometry and fixed specifications:

1. The wing has been chosen to be rectangular and un-twisted, since the effect of the main wing's taper ratio and sweep angle in efficiency is outside the scope of our study. For the selection of aspect ratio, it is considered that both the width of the craft and the strength requirements of the long wings are ultimate restrictions for high aspect ratios. Furthermore, because of the direct of effect of the wing length to the dimensions of the numerical solution domain, it was decided that the aspect ratio should be in medium range between 5 and 8 without entering the low-aspect ratio wing class.

2. There should be enough materials and references to obtain information about the flow characteristics of the wing section geometry at medium and high Reynolds numbers and low Mach numbers (incompressible flow).

3. Angle of attack should not be too high to lead flow separation or cavitation in considered domain particulars. Besides, it should not be too low, which will cause insufficient induced velocities to investigate.

4. It should match with the geometry in reference, which is used for validation. Hence selected geometry specifications are; Aspect Ratio (Λ): 6, Span Length: 6m, Tip Chord Length: 1m, Root Chord Length: 1m, Wing Section: NACA0012, Angle of Attack (AoA): 5^{o}

4.1.2 Selection of winglet geometries

The assumptions below are compromised in selecting the geometries and variables of winglets to be analysed.

1. The installation of the winglet to an existing wing should be easy. Therefore, the junction will be sharp edged, not blended.

2. The winglet should not increase the lifting surface area of the total wing. This means cant angle of the winglet will be always "0^{o}". Thus, the winglet would not contribute to the lift itself. It will have an influence upon lift only by reducing induced velocities.

The parameters were selected according to the criteria above:

- Winglet section profile: NACA0006,

- Root chord length of winglet: three different values; along all the chord of main wing, rear three quarter of the main wing, rear half chord of the main wing.

- Winglet span: Three different values; 1 chord length of main wing, 0.75 chord of main wing, 0.5 chord of main wing.

- All winglets are simply tapered (not elliptical or curvative) for the sake of easy construction. Taper ratio of 0.3 is the same for all winglets.

- Trailing edge sweep angle: Two different values; 0^o, 15^o.

- Winglet direction: Three types; upward, downward (Hoerner), both (fence).

Upward winglets are generally more efficient than downward ones (Liang et al, 2012). However, establishing the winglet upward may cause unwanted cavitation, ventilation or emergency problems when used on a hydrofoil. Thus a downward winglet configuration was also examined to see whether any drawbacks or advantages exist.

4.2 Computational Details

All numerical analyses were performed using ANSYS Fluent v.15 software. All cases solved with steady (spatial) approach since the study deals with steady, incompressible flow around fully submerged bodies. Free surface and gravity effects are neglected. For modelling the turbulent flow, RANS equations based k-ω SST approach (Menter, 1994) was preferred with SIMPLE algorithm to ensure pressure-velocity relation (Patankar, 1980). Energy equations were not taken account as the absence of any heat exchange or heat generation. The spatial discretization of the convective terms is done by the second-order forward differences method, while the spatial discretization of the viscous terms is done by the second-order central difference method (Davidson, 2005). For pressure calculations, pressure stepping approach is used. Along with the result obtained from the pressure correction method, a system of 7 unknown equations is formed in each successive approximation step. The Gauss-Seidel consecutive approximation method is used together with the AMG algorithm to accelerate the convergence of this system of linear equations (Wesseling, 1992).

The fluid was selected as fresh water with density of 998.2 kg/m^3 and kinematic viscosity of $1x10^{-6}$ m^2/s at temperature of 15^o celcius. In all cases, the incoming velocity of the fluid was held at 6m/s which correspond to the Reynolds number of $6x10^6$.

All domain meshes are prepared by using the software Pointwise v17.3r1. After some tentative approaches, it is experienced that structural meshing for foil geometries give more accurate results in boundary layer. Thereby, all domains of this study are prepared in structured (hexahedral) mesh type.

It is initially intended to establish all meshes with y^+ of 1 regarding the ability to simulate viscous boundary layer more precisely. However, creating the 3D meshes leaded rigours in providing the sufficient process*time resource. Allowing for the circumstances, it is concluded to create 3D meshes with y^+ of 50, even if it is obliged to concede to have slightly higher error in results. This topic is presented elaborately in Chapter 5.

The boundaries of the domains are placed at 25c distance in front, top and bottom directions and 50c in rear direction. For 3D analyses, the clearance to the side of the finite end of the foil is taken as s. Here, "c" is the chord length of the main foil and "s" is the half span length of the main foil.

For validation cases C-Type mesh was used. In 2D domains the wing placed horizontal without AoA. The boundary condition for frontal semi-circular and bottom boundary surfaces were selected as velocity inlet with proper direction according to intended AoA. The boundary conditions for far-field rear and top boundary surfaces were selected as pressure outlet. The additional boundary conditions for side boundary surfaces in 2.5D (3D wing with infinite span) and 3D domains, were selected as symmetry (no normal flux namely slip condition wall).

For test cases for wings with winglets H-type mesh was used. The wing placed with 5 degrees of AoA and flow was sent in x-direction in all cases. Thus, the boundary conditions of rectangular prism shaped domain were selected as velocity inlet for frontal boundary surface, pressure outlet for far-field boundary surface and symmetry for sides, top and bottom boundary surfaces.

The surfaces of wings were selected as smooth viscous wall (specific rougness height = 0, roughness coefficient = 0.5).

5. VERIFICATION AND VALIDATION STUDY

For a CFD study, it is essential to ensure the reliability of the used computational method and mesh structure. For the sake of this requirement, several test runs were performed for flow around wings all with a cross-section NACA0012. These tests are performed for two dimentional (2D) wing, three dimentianal wing without open ends which represents an infinite wing in span (2.5D), and three dimentional wing (3D) with an aspect ratio of 6. For each one of these three different patterns of flow, firstly a grid-dependency study is carried out at different mesh resolutions as verification. The type of mesh for all cases is C-type and structured with local refinements near wall especially at leading edge, trailing edge and wake region. Then, validation runs are performed at different angles of attack to compare with the available, reliable reference data.

5.1 Two Dimensional Verification and Validation Study

Firstly, a grid dependency study was carried out with three mesh resolutions for 2D programming. With the selected resolution, CFD validation studies were done for NACA0012 cross-section in 2D programming for three different angles of attack.

5.1.1 Two Dimensional Grid Dependency Study

Three different grid resolution models were used to find out an acceptable grid resolution. The cell sizes have been decreased in all axes by the ratio of $\sqrt{2}$ in sequence which multiplies the cell count by 2 for 2D domain. The coarsest mesh is denoted as mesh A, the medium mesh is denoted as mesh B, and the fine mesh is denoted as mesh C.

In all mesh layouts, the grid intension is increased around the location of trailing edge and leading edge. Grid resolutions of the mesh types are shown in Figure 5.1.

NACA0012 two dimensional wing at 10^o of AoA are tested at Re = $6x10^6$ for each one of the meshes A, B, and C. Lift coefficient and profile drag coefficient (C_L and

$C_{D(2D)}$) were calculated as the basic parameters for the grid dependency study. The related definitions are given in Eq. (5.1) and Eq. (5.2) respectively.

$$C_L = \frac{L}{0.5\rho V^2 S} \tag{5.1}$$

$$C_{D(2D)} = \frac{D_{2D}}{0.5\rho V^2 S} \tag{5.2}$$

Where, L is the lift force, D_{2D} is the profile drag force per unit span, ρ is the fluid density, V is the free-stream velocity and S is the reference area (chord length, c) of the wing. Results and details of mesh types are presented in Table.5.1.

Table 5.1: 2D Results and details of grid dependency study at 10^o AoA.

Mesh Type	Cell Count	Cell Quantity on Foil	Average y^+	C_L	$C_{D(2D)}$	Difference C_L%	Difference $C_{D(2D)}$%
A	47840	397	0.548	1.0639	0.01290	-	-
B	95420	557	0.557	1.0645	0.01244	0.056	3.56
C	191052	797	0.565	1.0650	0.01237	0.047	0.56

As seen in Table 5.1, the relative difference of C_L and $C_{D(2D)}$ values between mesh B and mesh C are satisfactorily small. Hence, the mesh type B (Figure 5.2) was selected to be used for validation test runs.

The results of the grid dependency study at 10^o AoA are shown in Figure 5.3.

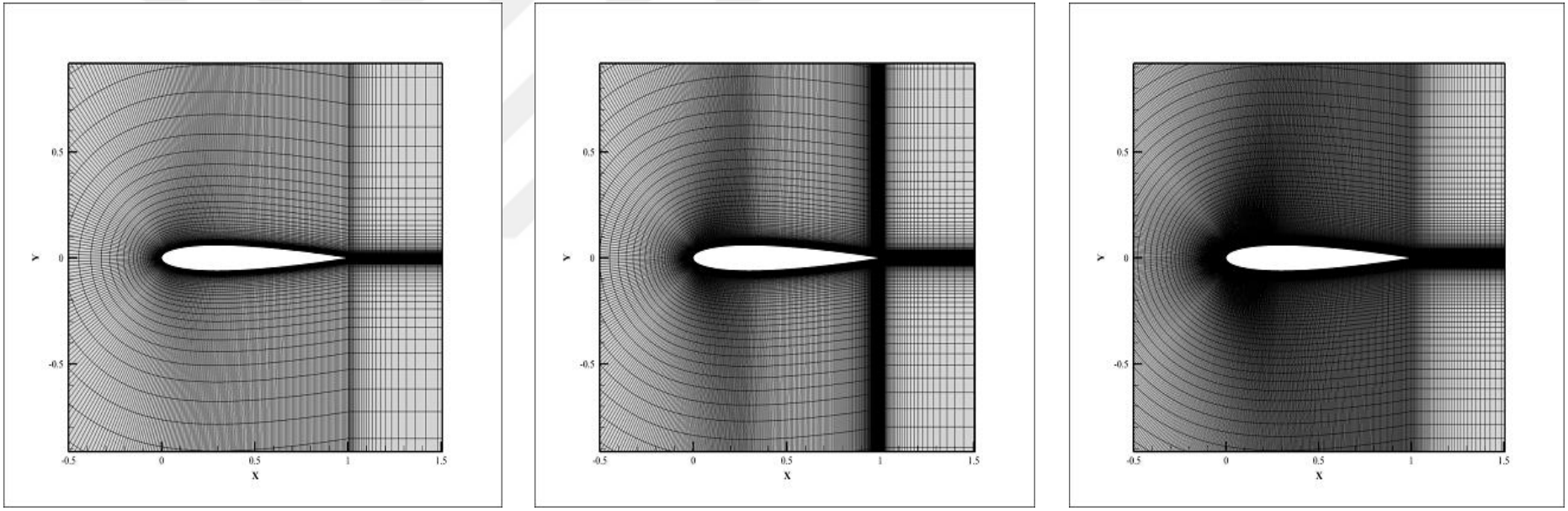

a) b) c)

Figure 5.1: 2D Grid Resolutions a)Mesh A, b)Mesh B, c)Mesh C.

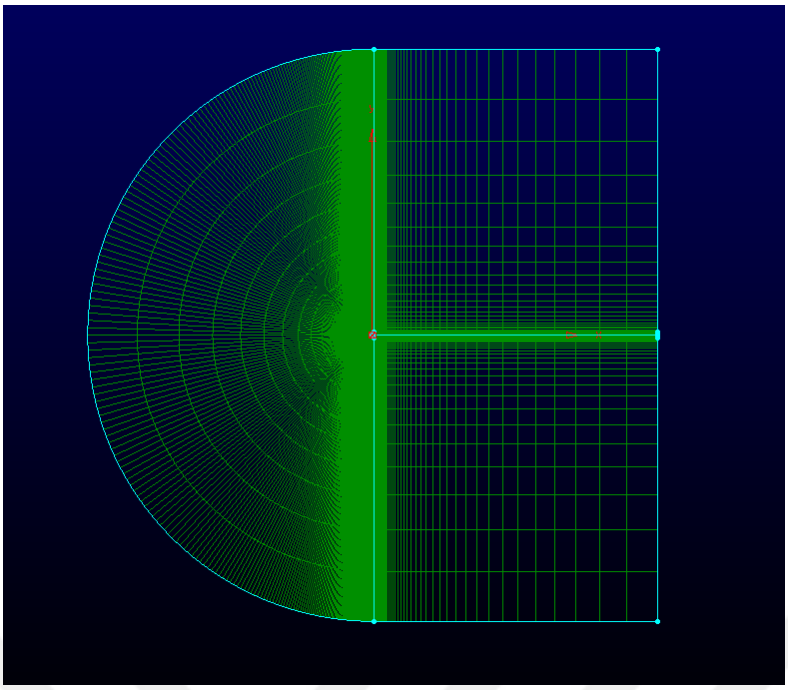

Figure 5.2: General view of mesh type B.

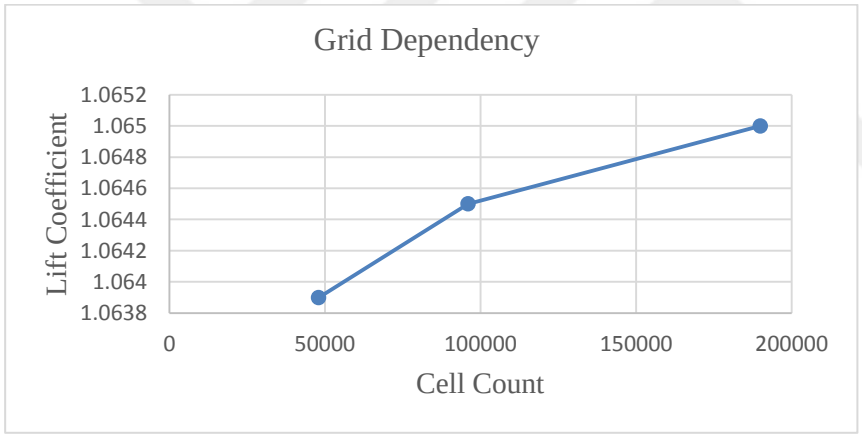

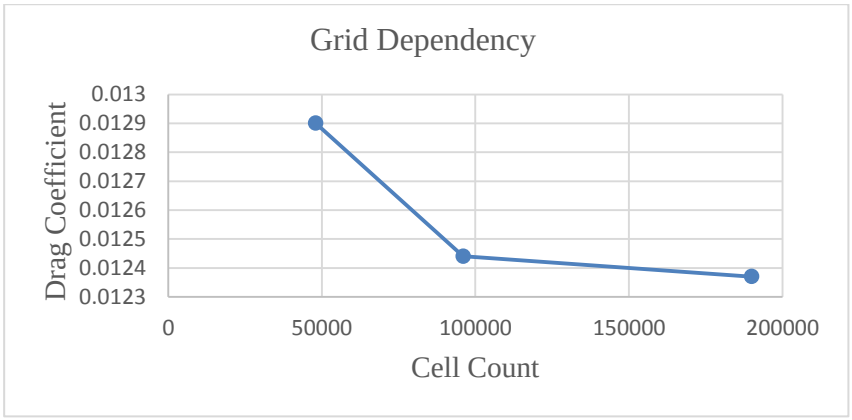

Figure 5.3: C_L and $C_{D(2D)}$ change of grid dependency study at 10^o angle of attack of NACA0012.

5.1.2 Validation results (2D)

For 2D validation, SST results of CFL3D CFD code which developed by NASA LaRC, used as reference source (URL1). Although CFL3D code is a compressible code but results are at "essentially incompressible" conditions of Mach Number of M=0.15. The profile NACA0012 at angles of attack of 0, 10, and 15 degrees, all of them at the Reynolds number $6x10^6$. In the test runs the fluid type was selected as liquid water, with a free-stream velocity of 6m/s, i.e., $Re=6x10^6$.

In the validation study, the comparisons are based on the lift coefficient (C_L), profile drag coefficient ($C_{D(2D)}$) and surface pressure coefficient distribution (C_P). Definition of C_P is given as in Eq. (5.3).

$$C_P = \frac{P - P_{ref}}{0.5\rho V^2} \tag{5.3}$$

In the equation, P is the local surface pressure, P_{ref} is the free-stream pressure, ρ is the fluid density, and V is the free-stream velocity.

The comparison of the C_L and C_D results for 0^o, 10^o and 15^o AoA of the analysis with the CFL3D SST code results is given in Table 5.2.

Additionally, C_P comparison is displayed in Figure 5.4 on 3 graphs for all 3 angles of attack.

Table 5.2: 2D Validation results.

	C_L			$C_{D(2D)}$		
AoA	This Study	CFL3D SST	Error %	This Study	CFL3D SST	Error %
0	0	0	0	0.00808	0.00809	0.12
10	1.0645	1.0778	1.23	0.01244	0.01236	0.65
15	1.4911	1.5068	1.04	0.02175	0.02219	1.98

As it seen in Table 5.2 the highest error is about 1.2% for 10^o AoA in C_L and about 2% for 15^o AoA in $C_{D(2D)}$. Figure 5.4 informs that C_P values obtained from analyses almost coincide with the values of CFL3D code results. It can be accepted that the method used in this study is satisfactory and sufficient.

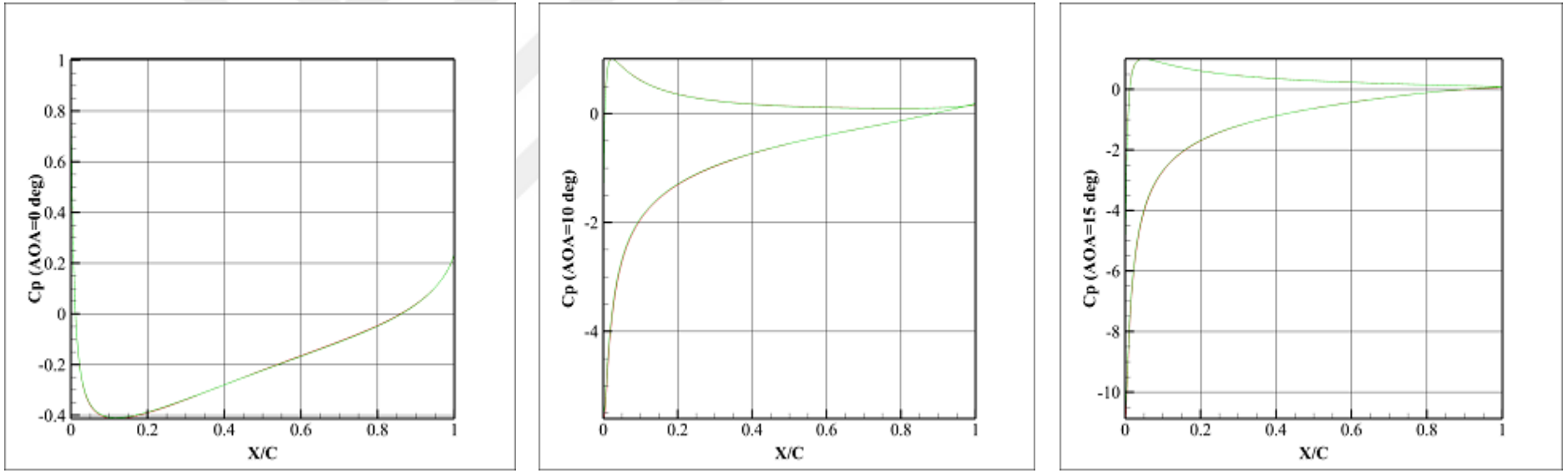

a) b) c)

Figure 5.4: 2D C_P comparison of CFL3D (red) and this study (green) a) 0deg AoA, b) 10deg AoA, c) 15deg AoA.

5.2 Verification and Validation of the 2.5D Study

Implementation of third direction in the discretization process can be checked in this 2.5D validation task. In fact, 3D programming is utilized for physically two-dimentional flow (flow around infinitely long NACA0012 wing). In a similar way that was performed for the 2D validation study, first a grid dependency study was carried out for an AoA of 10^o then the validation was conducted for angles of attack of 10^o and 5^o with chosen mesh structure.

5.2.1 Grid dependency study (2.5D)

The initial mesh structure generated by extruding the chosen 2D mesh 2*c (c is chord length) in spanwise direction with 100 cells and denoted as mesh type B. A coarser mesh denoted as mesh type A is generated by increasing cell dimensions by the ratio $\sqrt[3]{2}$ in all directions. Similarly, a finer mesh denoted as mesh type C is generated by decreasing cell dimensions by the ratio $\sqrt[3]{2}$ in all directions. As in 2D study the y^+ value is 1 for all meshes. Also in 2.5D, lift coefficient and profile drag coefficient (C_L and $C_{D(2.5D)}$) were calculated as the basic parameters for the grid dependency study. Grid resolutions of the mesh types are shown in Figure 5.5. Results and details of mesh types are presented in Table 5.3.

Table 5.3: 2.5D Results and details of grid dependency study.

Mesh Type	Cell Count	Cell Quantity on Foil	Average y^+	C_L	$C_{D(2.5D)}$	Difference C_L%	Difference $C_{D(2.5D)}$%
A	$4.6*10^6$	34320	0.562	1.0628	0.01284	-	-
B	$9.6*10^6$	55044	0.564	1.0632	0.01272	0.037	0.934
C	$19*10^6$	87000	0.573	1.0634	0.01267	0.019	0.393

As seen in Table 5.3, the relative difference of C_L and $C_{D(2.5D)}$ values between mesh B and mesh C are satisfactorily small. Hence, mesh type B was selected for validation calculations.

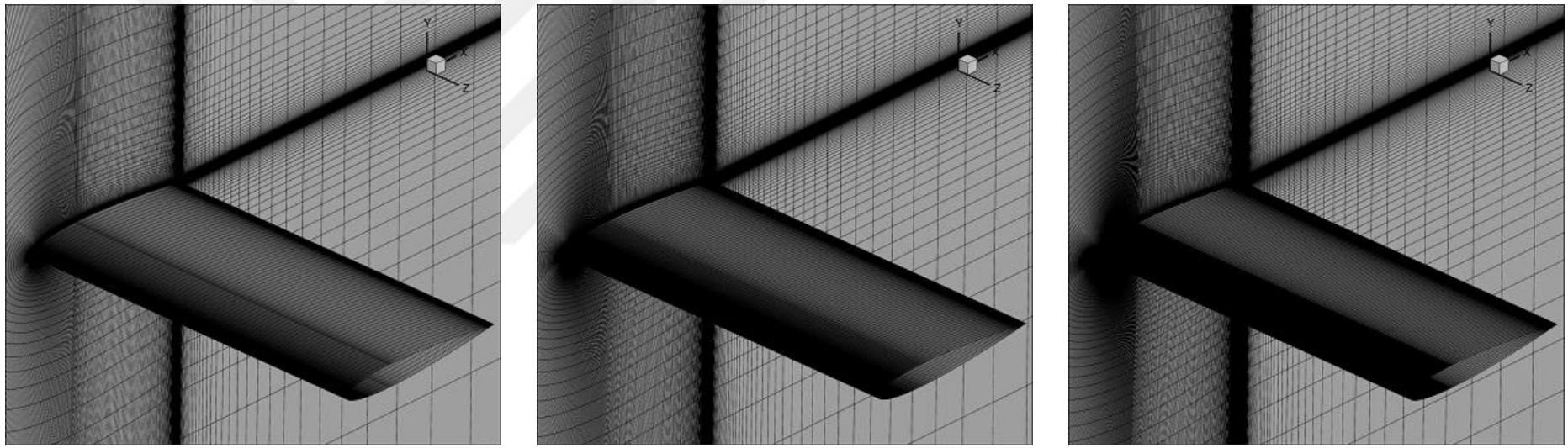

a) b) c)

Figure 5.5: Grid resolutions of 2.5D a) Mesh A, b) Mesh B, c) Mesh C.

5.2.2 Validation results (2.5D)

The 2D results of CFL3D code were used for 2.5D validation since physically 2D flow pattern is expected as the solution from the 2.5D study run. The angles of attack were 5^o and 10^o. For 5^o AoA reference values, an extrapolation was done between 0, 10^o and 15^o AoA data of CFL3D results. 5^o AoA analysis was conducted especially; because the main wing which winglets were applied on, is operated at 5^o of AoA.

Similar to 2D validation parameters, also in 2.5D validation, lifting force coefficient (C_L), surface pressure coefficient distribution (C_P vs x/c) and profile drag coefficient ($C_{D(2.5D)}$) were compared. The comparison of the C_L and C_D results for 5^o, and 10^o AoA of the current study with the CFL3D SST code results (extrapolated result for 5^o) is summarised in Table 5.4. C_P distribution data of the 10^o AoA analysis, which is used for validation in Figure 5.6, is taken from the section plane at the center of the wing in spanwise direction. There is no C_P comparison for 5^o AoA due to the lack of CFL3D analysis at 5^o AoA.

Table 5.4: 2.5D Validation results (CFL3D values for 5^o AoA are extrapolated)*.

	C_L			$C_{D(2.5D)}$		
AoA	This Study	CFL3D SST	Error %	This Study	CFL3D SST	Error %
5	0.5455	0.5461*	0.11	0.00914	0.00933*	2.04
10	1.0632	1.0778	1.35	0.01272	0.01236	2.91

Table 5.4 shows that the errors in C_L and $C_{D(2.5D)}$ for 10^o AoA are 1.35% and 3% respectively. The errors of 5^o AoA analysis are much smaller. It is observed that the percentage of errors have increased slightly relative to 2D analyses probably because of the additional discretization error in z-direction. Even so, the amounts of the errors seem to be acceptable and the results are considered as reliable for further work. In Figure 5.6, the graph shows that also C_P curve convergence is quite accurate and reliable.

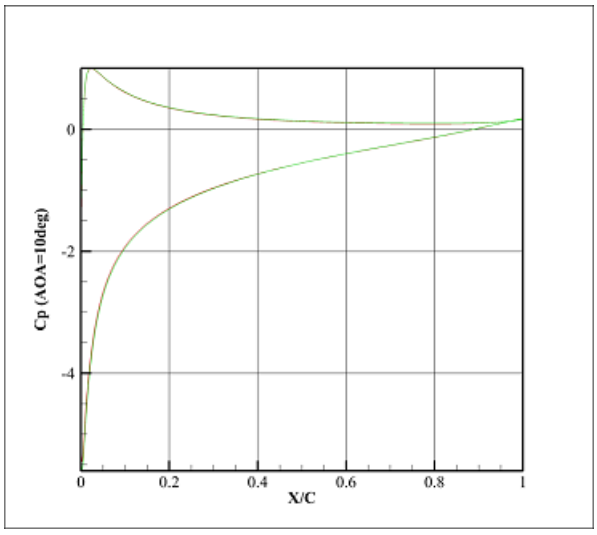

Figure 5.6: 2.5D C_P Comparison at 10^o AoA: CFL3D (red) and this study (green).

5.3 Verification and Validation of the 3D Study

3D validation has been carried out with a 3m semi-span and 1m chord length rectangular foil which has a total aspect ratio 6. The initial mesh is generated by using the grid resolution of the chosen 2.5D mesh. In a similar way that was performed for the 2.5D validation study, firstly a grid dependency procedure was carried out at AoA of 10^o; then validation process was conducted at AoA of 10^o and 5^o. Mesh structures were generated with y^+ value of 1. After selecting the proper mesh resolution, the analyses were carried out using Fluent v15 at AoA of 10^o and 5^o. However, it is needed to use another approach of comparison in stead of validation due to the lack of experimental and/or reliable viscous CFD reference. The results are compared with inviscid numerical solution obtained by XFLR5 solver which is based on lifting line theory. Details about this approach of comparison are presented in sub-chapter 5.3.2.

Differently from previous grid dependency procedures, for 3D verification the grid size changed only in spanwise direction (z-direction). This was compulsory due to the excessive number of cells needed to perform refinement in all directions. It is concluded that 2D and 2.5D grid dependency studies are sufficient to determine the optimal grid resolution in x-y plane (section cut) which influences viscous turbulence accuracy. Details of 3D grid dependency study are presented in sub-chapter 5.3.1.

Since the mesh structures generated for the cases of wings with winglets will require excessive number of grid cells with y^+ value of 1, another grid dependency study and

the comparison test were carried out for 3D bare wing mesh structures with y^+ value of 50.

5.3.1 Grid dependency study (3D, y^+=1)

In 3D grid dependency study, the streamwise gridline of the initial mesh (type B) was taken from the 2.5D mesh structure. In spanwise direction, 150 gridlines were used such that the resolution was concentrated towards the open end of the wing but the average cell size has not been changed. A 3 m gap in width is left from the tip of the wing to the side boundary of the flow domain. 100 cells are placed in this gap in z-direction (spanwise) with a concentration near tip surface. This mesh structure is denoted as mesh type B. Mesh type A and mesh type C are generated coarser and finer respectively. Mesh type A has 120 cells on foil and 80 cells in the gap in z-direction. Mesh type C has 200 cells on foil and 150 cells in the gap in z-direction. Results and details of mesh types are presented in Table 5.5.

Table 5.5: 3D (Y^+=1) Results and details of grid dependency study.

Mesh Type	Cell Count	Cell Quantity on Foil	Average y^+	C_L	C_D	C_L Difference %	C_D Difference %
A	$22*10^6$	78112	0.669	0.7715	0.03976	-	-
B	$27*10^6$	116692	0.661	0.7718	0.03978	0.038	0.050
C	$38*10^6$	144492	0.675	0.7719	0.03979	0.013	0.025

As seen on Table 5.5, the relative difference of C_L and C_D values between mesh B and mesh C are satisfactorily small. Hence, mesh type B was selected for validation calculations. Grid resolution of the mesh type B is shown in Figure 5.7.

5.3.2 Validation results (3D, y^+=1)

For 3D validation a potential solver XFLR5 was used for lifting line calculations in order to estimate induced lift (C_{Li}) and induced drag coefficient (C_{Di}) to compare with the numerical results. The total drag coefficient (C_D) can de expressed as the sum of profile drag coefficient and induced drag coefficient. Hence, validation method for total drag coefficient of the 3D wing is comparing the numerical total drag coefficient from 3D numerical analysis and the sum of 2.5D numerical profile drag coefficient result and the induced drag coefficient result obtained from XFLR5.

Also, in 3D validation the wing was tested at AoA of 5^o and 10^o. The comparison of the C_L and C_D results for 5^o, and 10^o AoA of the 3D analysis with the combination of XFLR5 and 2.5D analyses results is given in Table 5.6.

Table 5.6: 3D Validation results.

	C_L			C_D				
AoA	This Study C_L	XFLR5 C_L	Error C_L%	This Study C_D	XFLR5 C_{Di}	This Study $C_{D(2.5D)}$	XFLR5 C_{Di} + This Study $C_{D(2.5D)}$	Error C_D%
5	0.3857	0.3961	2.625	0.01630	0.00730	0.00914	0.01644	0.851
10	0.7718	0.7900	2.303	0.03978	0.02860	0.01272	0.04132	3.727

Table.5.6 shows that the error in total drag coefficient (C_D) is about 3.72% and in induced lift coefficient (C_{Li}) about 2.3%. Differently from previous validation results it is noticed that the character of the error is changed. In previous studies the profile drag coefficients of Fluent based numerical analyses were slightly higher than the reference values. However, in 3D analyses the total drag coefficient of Fluent result is slightly lower than the reference value. Also is can be noticed that the error in lift coefficient is increased. Actually it is not an unexpected issue. XFLR5 has a tendency to overestimate C_{Li} slightly higher at moderate angles of attack (Botez et al., 2016). By the algorithm of lifting line method C_{Di} is proportional to C_{Li}^2 (Eq.2.15). Thus, if we consider that C_{Dp} of 3D analysis is quite similar with result of 2.5D analysis, a 3% underestimated C_D seems to be normal and expected.

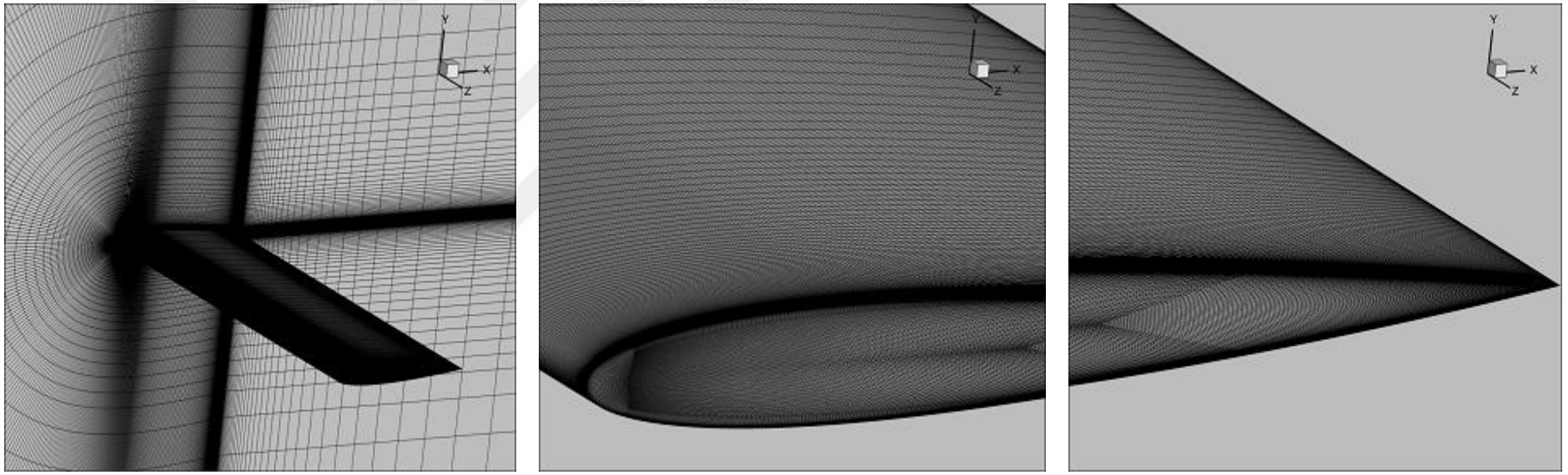

General Leading edge of open tip Trailing edge of open tip

Figure 5.7: 3D y^+=1 Grid resolution of mesh type B.

5.3.3 Grid dependency study and validation results (3D, y^+=50)

After some trials, it is discerned that constructing meshes of wingleted wings with y^+value of 1 leads extreme cell counts and unfavorable quality conditions of grid. Herewith, a new mesh structure has been generated with y^+ value of 50. This mesh structure was denoted as mesh type E in grid dependency study. Mesh type D and mesh type F were generated as coarse and fine meshes respectively. The spanwise grid resolution was optimized in the previous sub-chapter. Thereby, the refinement was made only in section plane (x-y plane) by ratio of $\sqrt[3]{2}$.

The grid dependency study is carried on with 10^o AoA. Results and details of mesh types are presented in Table 5.7. Grid resolutions of mesh types are shown in Figure 5.8.

Table 5.7: Results and details of grid dependency study (Y^+=50).

Mesh Type	Cell Count	Cell Quantity on Foil	Average y^+	C_L	C_D	Difference C_L%	Difference C_D%
D	$8.8*10^6$	64764	60.7	0.7658	0.0413	0	0
E	$12.4*10^6$	85173	60.5	0.7673	0.0409	0.196	0.968
F	$17.7*10^6$	107296	61	0.7685	0.0408	0.156	0.244

According to Table.5.7, the relative difference of C_L and C_D values between mesh E and mesh F are satisfactorily small. Thus, mesh type E is reanalysed with 5^o of AoA and the validation procedure is presented in Table 5.8. A comparison with mesh type B is made in 10^o and 5^o angles of attack and examined in Table.5.9.

Table 5.8: 3D (Mesh type E) Validation results.

	C_L			C_D				
AoA	This Study C_L	XFLR5 C_L	Error C_L%	This Study C_D	XFLR5 C_{Di}	This Study $C_{D(2.5D)}$	XFLR5 C_{Di} + This Study $C_{D(2.5D)}$	Error C_D%
5	0.3838	0.3961	3.105	0.01660	0.00730	0.00914	0.01644	0.954
10	0.7673	0.7900	2.873	0.04090	0.02860	0.01272	0.04132	1.016

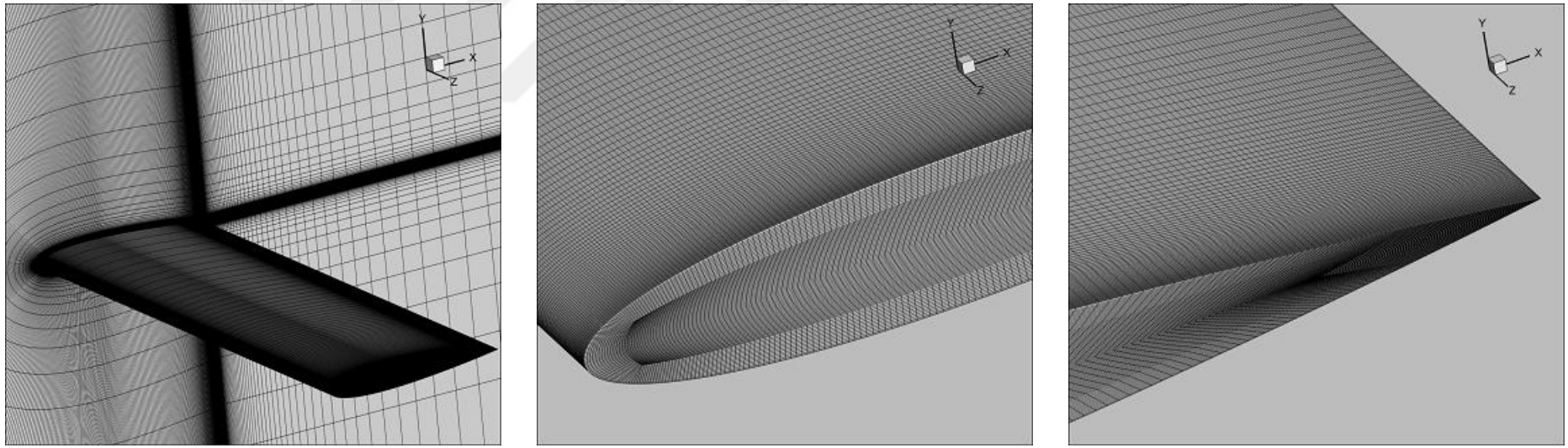

General | Leading edge of open tip | Trailing edge of open tip

Figure 5.8: 3D y^+=50 Grid resolution of mesh type E.

Table 5.9: 3D (y^+=50) and 3D (y^+=1) comparison.

AoA	Mesh B C_L	Mesh E C_L	Mesh B C_D	Mesh E C_D	Relative Error C_L%	Relative Error C_D%
5	0.3857	0.3961	0.01630	0.01644	2.69	1.84
10	0.7718	0.7900	0.03978	0.04132	2.38	3.87

At first glance, when Table 5.8 and Table 5.6 are examined, mesh E represents a better convergence in C_D. Normally, mesh type E is supposed to give higher errors than mesh type B due to the coarser grid resolution in boundary layer. The suspicious improvement in the error of C_D is a consequence of overestimation of XFLR5 which is mentioned previous sub-chapter. The C_{Dp} result from the analysis of mesh type E is also overestimated due to the coarser boundary layer (y^+ =50). Consequently, these separate overestimations compensate each other, thus, the total drag coefficient (C_D) seems like converged more accurately.

Figure 5.9 shows the velocity magnitude comparison of mesh type B and mesh type E around the section 2.5 m distant from root of the wing at 5^o AoA. Besides, Figure 5.10 shows the vorticity distributions on the y-z plane 0.1*c behind the trailing edge of both mesh type B and mesh type E.

Difference in the velocity magnitude distribution is inconspicuous in Figure 5.9. Even if there are some differences in the vorticity distribution in Figure 5.10, main characteristics of the pattern is quite similar. Hereby, it is decided that the rest of the study can be carried out with mesh structures of wingleted wings which are based on the specifications of Mesh type E.

Figure 5.10 shows the vorticity magnitude comparison of mesh type B and mesh type E on the slice of wake region 0.1c behind the trailing edge. Although there are visible differences in shapes of contour lines, the main distribution is very similar to each another with same peak values. Eventually, the results are not perfect but acceptable.

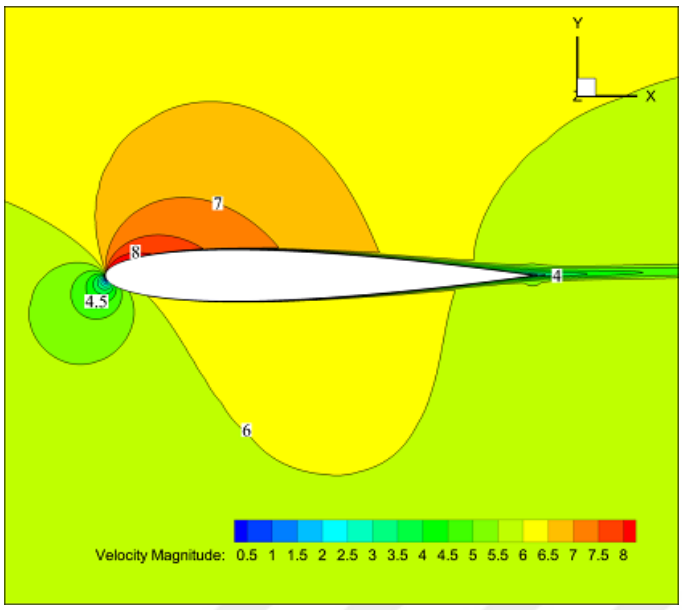

a)

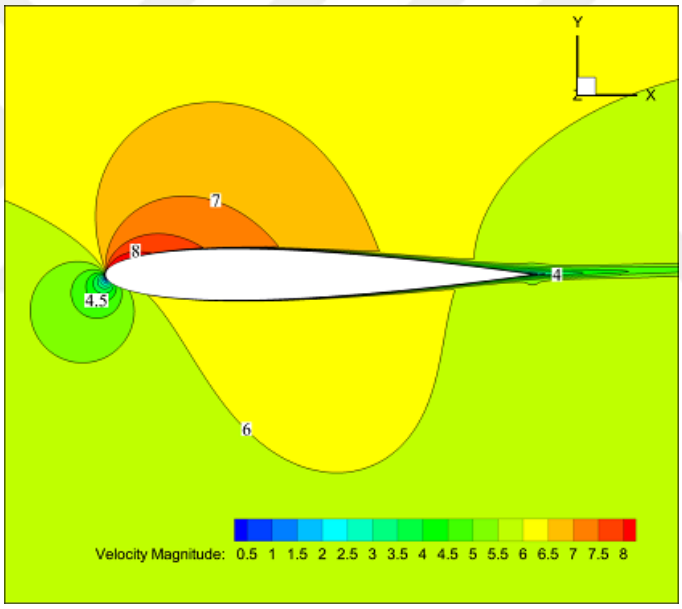

b)

Figure 5.9: Velocity magnitudes of Mesh type E (a) and Mesh type B (b) at 5^o AoA, 2.5 m distant from wing root.

As a conclusion for 3D analyses with y^+ value of 50, the maximum error estimations are 5% in C_L and %7 in C_D with considering the error in 2.5D analyses with y^+ value of 1, error in 3D analyses with y^+ value of 1, and relative difference between 3D analyses with y^+ value of 1 and 3D analyses with y^+ value of 50.

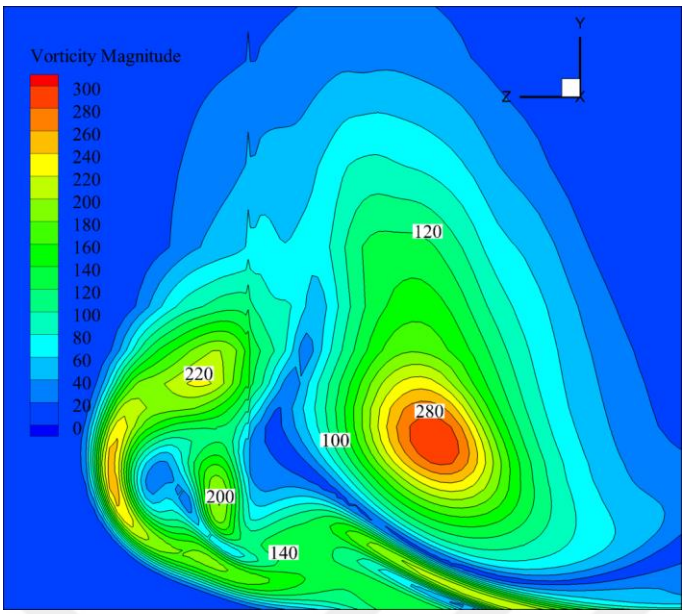

a)

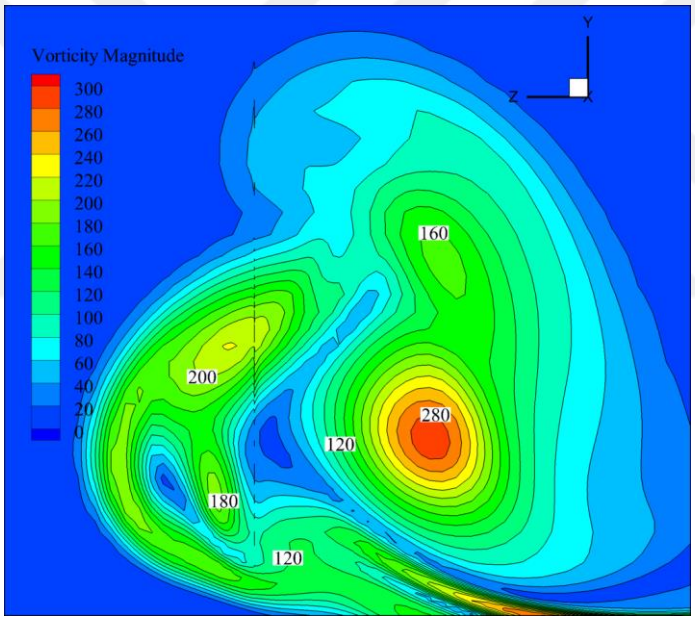

b)

Figure 5.10: Vorticity magnitudes of Mesh type E (a) and Mesh type B (b) at 5^{o} AoA, 0.1c behind of trailing edge.

6. RESULTS & DISCUSSION

The effect of the root chord length of the winglets was first examined while the other basic geometrical parameters were kept constant. Accordingly, whilst the ratio of Sw/Cmw (SCR) and winglet trailing edge sweep angle (Θ) was initially set to 0.5 and 0^o, respectively, an upward pointing winglet configuration was adopted. After investigating the results of three analyses, the chord length value of the most efficient winglet was selected and fixed for the subsequent examinations. Then, the effect of the variation in winglet span length was evaluated with inclusion of two additional span length values. Simulations were also performed for downward pointing, fence type winglet configurations. Finally, a sweep angle of 15^o to the trailing edge of the most efficient winglet was applied. The geometrical parameters used in this study are presented in Table 6.1, and the force coefficients of all configurations in Table 6.2. The side views of the winglets, on the other hand, are shown in Figure 6.1. Interpretations of the analyses and parameters are elaborated in the respective sub-chapters. Wing with winglets are numbered from 1 to 8 and denoted sequentially W1 to W8. The bare wing is denoted as W0.

Table 6.1: Geometric parameters of winglets.

Winglet	CCR	SPR	DW	Θ
W1	1	0.5	Up	0
W2	0.75	0.5	Up	0
W3	0.5	0.5	Up	0
W4	1	0.75	Up	0
W5	1	1	Up	0
W6	1	0.75	Down	0
W7	1	0.75	Both	0
W8	1	0.75	Up	15

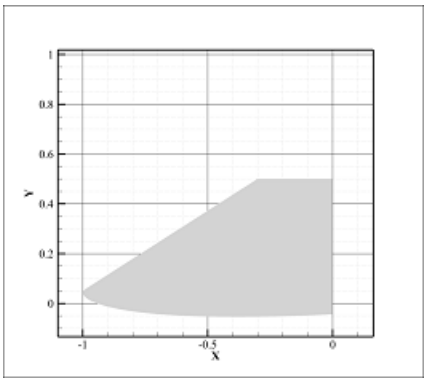

W1

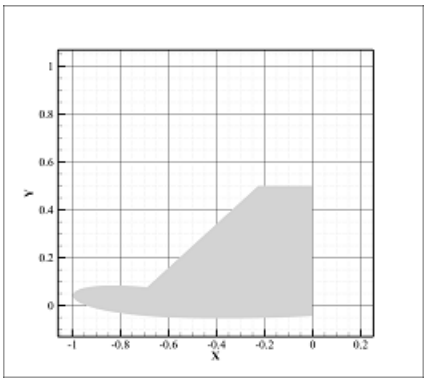

W2

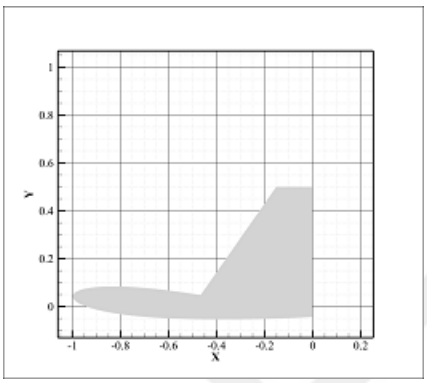

W3

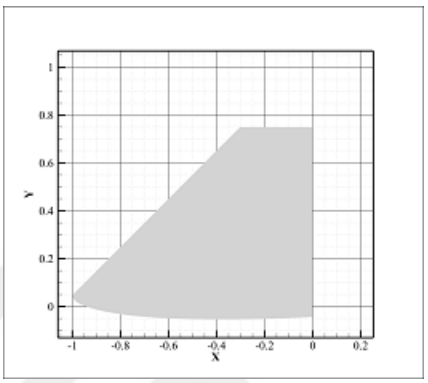

W4

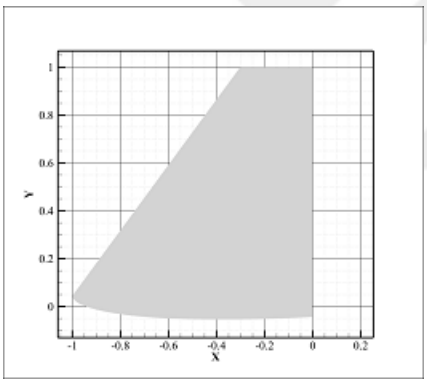

W5

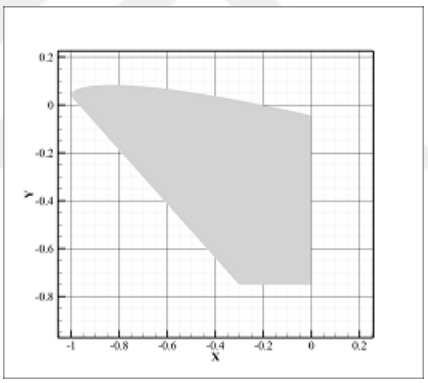

W6

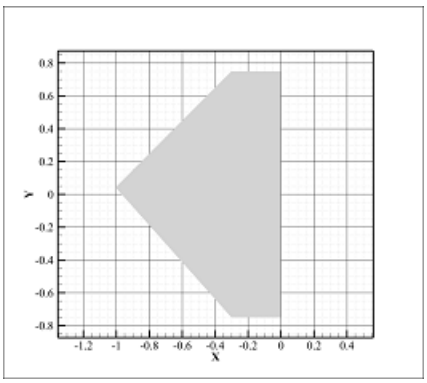

W7

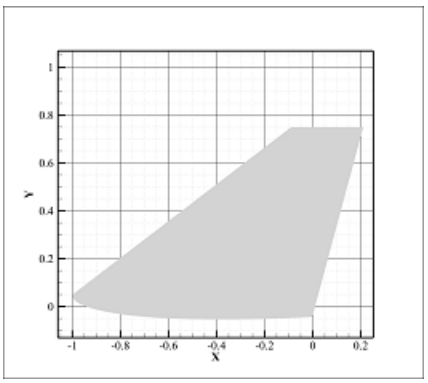

W8

Figure 6.1: Sideviews of wingleted wings.

Table 6.2: General results of wingleted wings and bare wing.

	W0	W1	W2	W3	W4	W5	W6	W7	W8
C_L	0.3838	0.4223	0.4166	0.4098	0.4307	0.4337	0.4001	0.4357	0.4296
C_D	0.0166	0.0172	0.0171	0.0170	0.0175	0.0178	0.0166	0.0179	0.0174
ΔC_L%	-	10,03	8.54	6.77	12.22	13.00	4.25	13.55	11.93
ΔC_D%	-	3,61	3.01	2.41	5.42	7.23	0.00	7.83	4.82
Cl/Cd	23.12	24.55	24.36	24.11	24.61	24.36	24.10	24.34	24.69
Δ(Cl/Cd)%	-	6.19	5.37	4.26	6.44	5.38	4.25	5.28	6.78
Cell Count	12.4m	35.4m	35.3m	35.1m	37.1m	38m	37.2m	50.1m	37.2m

6.1 Effect of "CCR (Cwr/Cmw)"

The ratio of root chord length of winglet to chord length of main wing (CCR) was investigated at 3 different values as 1, 0.75 and 0.5 with SPR value of 0.5. The generated structures are labelled as (W1), (W2) and (W3) with CCR ratios equal to 1, 0.75 and 0.5 respectively.

At the first glance, the comparisons given in Table 6.2 indicate that W1, W2 and W3 i.e. the wingleted wings are more efficient than the bare wing. The most efficient among them is W1 which has the CCR value of 1. The table also shows that in terms of Cl/Cd ratio, W1, W2 and W3 provide a gain of 6.19%, 5.37%, and 4.26%, respectively. Winglets significantly increase the lift coefficient (C_L) but do not have any decreasing effect on drag coefficient (C_D). (In the calculation of all C_D and C_L values, the projected area of the wing is fixed to $3m^2$ without adding the area of the winglet in order to have a true idea about the change in the total drag and lift force.) It should be noted that, the increase in lift coefficient means lower rates of tip vortices-driven reduction for the lift forces. Meanwhile, it is conjecturable that, induced drag coefficients are decreasing but only at lower rates than those of the increments in the profile drag coefficients. Overall, the total drag coefficients are on the rise.

It may be foreseen that the added surface which causes an additional profile drag force would be the smallest on the W3 and the largest on the W1. Interestingly, a comparison of variation in Cd values in Table 6.2 exhibits smaller increments between W3 and W2 than those of the W2 and W1, 0.59% and 0.58% respectively. The increments in C_L values, on the other hand, are more significant than C_D

variations: 10.03%, 8.54%, and 6.77% for W1, W2 and W3 respectively. The fact that C_L gains are higher than the increase in C_D values signifies that, favorable C_{Di} drops driven by the reduction in the tip vortex effect make up for/compensate C_{Dp} inclines to a large extent. Following on from this assessment, as the winglet takes up a higher percentage of the tip chord of the main wing, the preferred effect of the winglet becomes stronger. Therefore, W1 that covers the whole chord of the main wing gives the best result of the three configurations.

Figure 6.2 depicts general trajectories of x vorticity. The vorticity distribution can be investigated with a view to determining the areas where large vortices emerge. Table 6.3 lists extreme x vorticity values read at the center of the fully developed vortices forming around the open tip at 0.75c, 0.5c, 0.25c, and 0c, in front of the trailing edge in respective cases. Also in Figure 6.3 is presented a comparative view of the x vorticity distributions at 0.25c behind the trailing edges, with a focus on the open-end tip area of these three wingleted wings and bare wing. The formula for vorticity and x vorticity are shown in Eq. 6.1 and Eq. 6.2, respectively.

$$\vec{\omega} = \nabla x \vec{v} = \left(\frac{\delta}{\delta x}, \frac{\delta}{\delta y}, \frac{\delta}{\delta z}\right) x (v_x, v_y, v_z) \tag{6.2}$$

$$\omega_x = \left(\frac{\delta v_z}{\delta y} - \frac{\delta v_y}{\delta z}\right) \tag{6.2}$$

As seen in Figure 6.2a, there are two strong clockwise rotating vortices generated from the tip of the bare wing. The upper one, in particular, significantly affects the wing's low pressure side, and mounts to 520 s^{-1}. After the trailing edge in the wake region, these two vortices unite to make one clockwise vortex slightly canted towards the wing root.

In Figure 6.2b, there is only one vortex along the tip of the main wing(junction), and the main unfavorable vortex which canting on the low pressure side on the W0 is almost totally dispersed at W1. A new vortex emerges at the tip of the winglet, but the vorticity magnitude at its center reaches its maximum at very end of the tip chord with a value of 400s^{-1}. This vortex has a considerably lesser effect on the main wing under favour of the distance to the main wing when compared the vortex which affects the low pressure side of the W0.

W2 and W3 failed to equal the performance of W1. In Figure 6.2c and Figure 6.2d clearly illustrate that adverse/unfavorable vortices, which create unwanted induced velocities and affect the low pressure side of the main wing, are not successfully vanished. Even with vortices fading closer towards the trailing edge, their major effects on the forward naked part of the wing remain. The strength of those vortices peaks at the maximum thickness of the winglet.

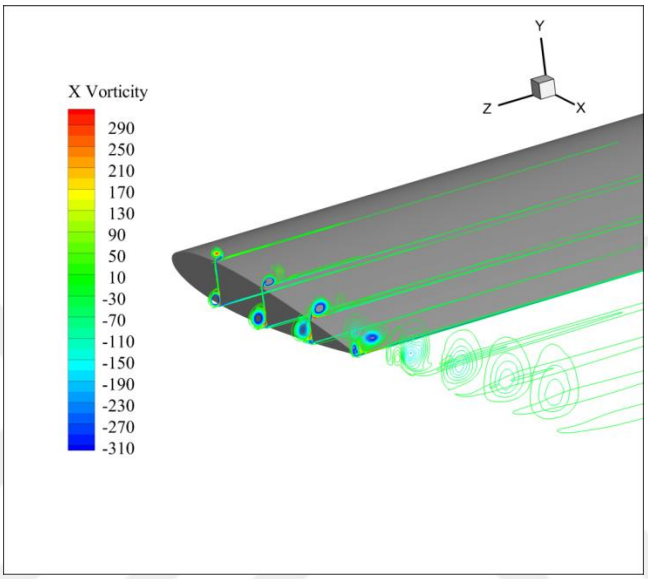

a)

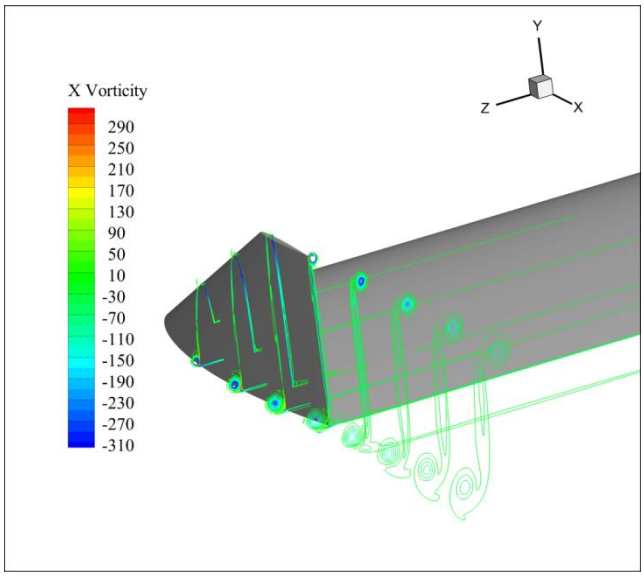

b)

Figure 6.2: X vorticity trajectories a) W0, b) W1, c) W2, d) W3.

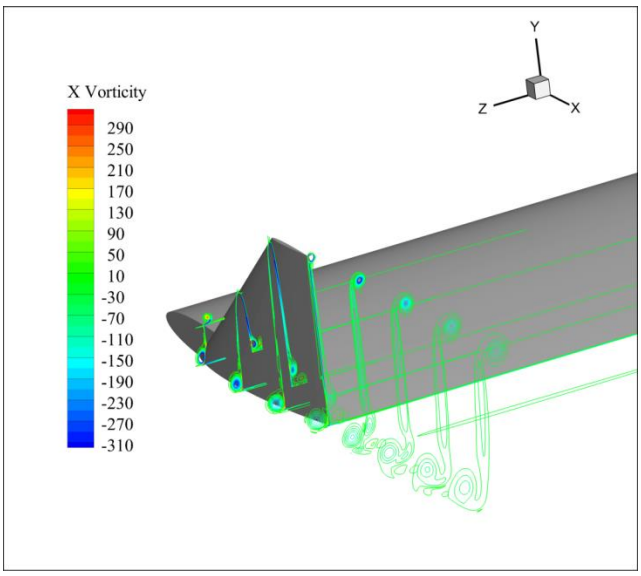

c)

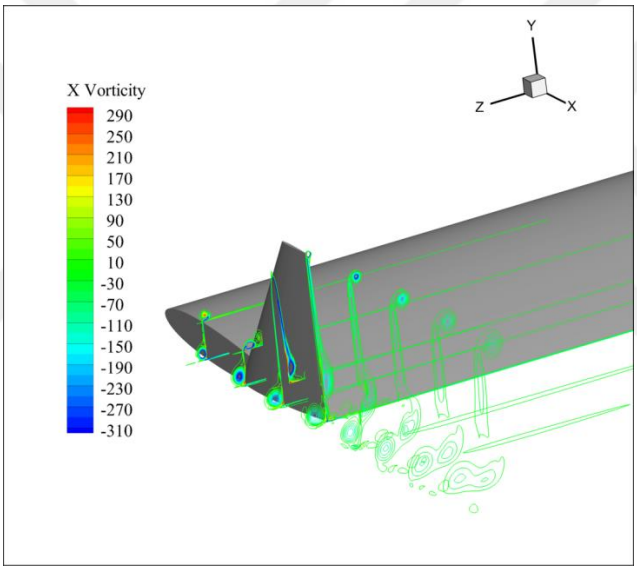

d)

Figure 6.2 (cont.): X vorticity trajectories a) W0, b) W1, c) W2, d) W3.

When it is revolved about the wake at 0.25c behind trailing edge in Figure 6.3, the united single tip vortex of the bare wing is cants inward with a peak x vorticity value of $190s^{-1}$. In figure 6.3 c & d, we see that the vortices generated around the junction still failed to unite into a single tip vortex at the wake. Presence of the winglet hinders the outer (lower) vortex from swirling inside and merging with the inner (upper) one. Plus, it is demonstrated that at both winglets, the strength of the vortices at the level of the trailing edge of the main wing are trimmed down at least by approximately 31.5 percent (190 to 130).

Unlike the two above-mentioned winglets, W1 (covering the entire chord of the main wing) does not allow for generation of an inner vortex whatsoever. Eventually, the outer vortex does not cant inside nor appears an unfavourable inner vortex.

However, it cannot be said that the wakes evolve more smoothly. The x vorticity of the vortex emitted from the tip of the winglet reaches a value about $390s^{-1}$ in W1 and $410s^{-1}$ in W2 and W3. Even if these vortices have no significant impact on the performance of the main wing and act within a small diameter of dominance, they cause an exceptional local turbulence point.

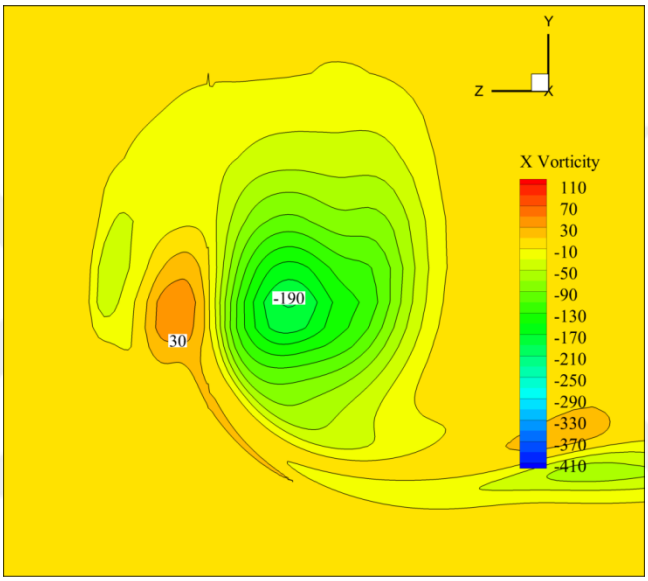

a)

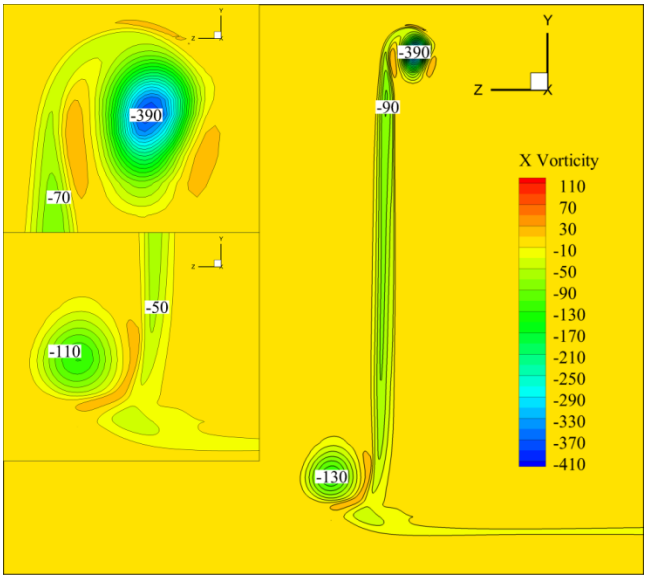

b)

Figure 6.3: X vorticity at 0.25c behind trailing edge (looking from behind) a) W0, b) W1, c) W2, d) W3.

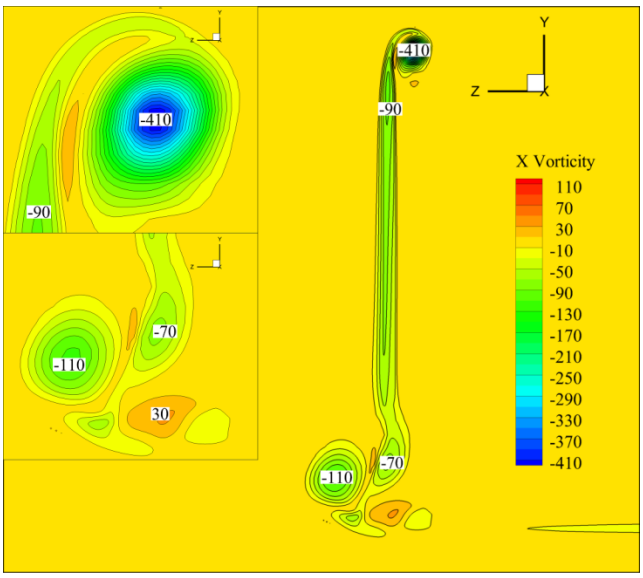

c)

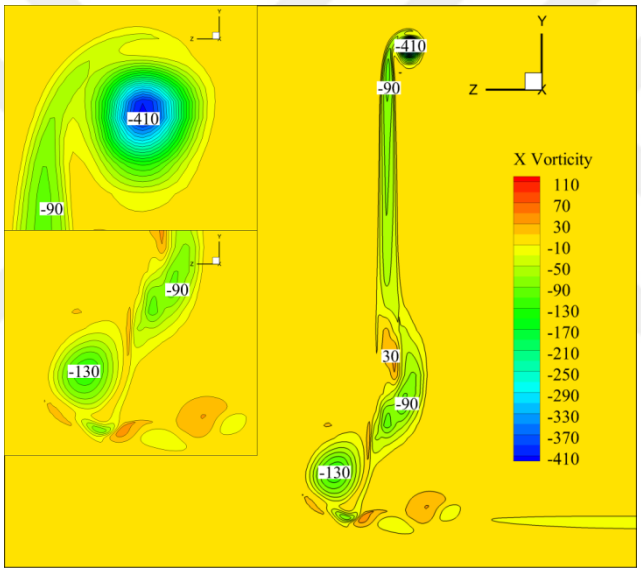

d)

Figure 6.3 (cont.): X vorticity at 0.25c behind trailing edge (looking from behind) a) W0, b) W1, c) W2, d) W3.

To better reflect the effects of the tip vortices and induced velocities in y and z directions on the low-pressure side of the main wing, Figure 6.4 indicates the streamlines at the x slice of 0.75c behind the leading edge via a velocity magnitude color scaling on the Y-Z plane. It is seen in Figure 6.4 that streamlines of induced velocities form a strong vortex cants towards the low-pressure side of the bare wing as evidenced by vorticity distributions. Additionally, there is a separation border approximatey 0.5c above the low-pressure side.

Even if there is no significant change in Y-Z velocity magnitudes between W0 and W1, W1 configuration shifts the unfavourable vortex that emerges adjacent to the low-pressure side of the main wing towards the tip of the winglet. Moreover, the winglet prevents the flow separation occurred in W0.

W2 and W3 perform similar characteristics to W1. However, they are not successful as W1 in shifting the vortex canting towards the low pressure side of the main wing.

Lastly, Figure 6.5 illustrates a Cp comparison of the z slice at 2.95m outer to the tip from the root of main wing. The pressure coefficient distribution is a proof key for the lift coefficient. The difference between the high-pressure and low-pressure surfaces gives an opinion about the lift force exerting on the area near the tip of the main wing.

Table 6.3: X vorticity values of W0, W1, W2, W3. ("–": no fully developed vortex; "Tip": winglet tip; "Upper J": upper part of the junction; "Lower J": lower part of the junction).

Location	W0	W1	W2	W3
0.75 c front from trailing edge				
Tip	-	-	-	-
Upper J	320	120	260	280
Lower J	-750	-900	-580	-680
0.5 c front from trailing edge				
Tip	-	-	-	-
Upper J	-520	-	-680	-560
Lower J	-380	-400	-300	-320
0.25 c front from trailing edge				
Tip	-	-	-	-
Upper J	-400	-20	-240	-440
Lower J	-240	-240	-200	-220
At trailing edge				
Tip	-	-700	-900	-1180
Upper J	-320	-	-80	-180
Lower J	-320	-160	-120	-160

On the high-pressure sides, there is almost no difference between the wingleted wings and the bare wing. An observation of the low-pressure side of the bare wing reveals that Cp decreases to only -0.5, and a great percentage of the upper side, the value of Cp is between -0.1 and -0.2. An area around the trailing edge, which extends at a slightly higher level than that of the wing surface, reaches -0.4.

As for the wingleted wings, the characteristic of the contours on the upper side is completely changed. The lowest Cp value of W1 is -0.6, and it covers approximately

a quarter of the length on the upper side. Similarly, the -0.3 contour covers a significant length, corresponding to 70% of the upper side.

In conclusion, it is clearly seen that the winglet absorbs the pressure rising over the low-pressure side and helps the wing keep the pressure difference between the high-pressure and low-pressure sides, which creates the lift force near the main wing tip. W2 too has -0.6 as the lowest Cp value. That said, it barely covers 15 percent of the upper side. Similarly, the -0.3 contour covers a relatively small area. These findings are in line with the Cl values obtained.

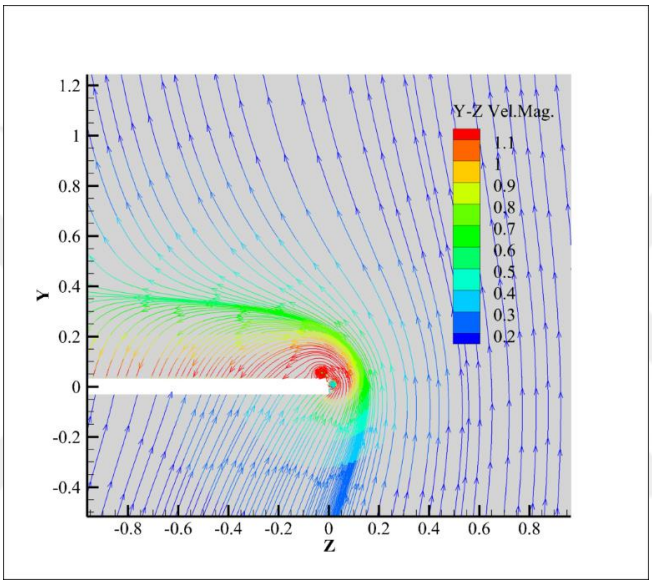

a)

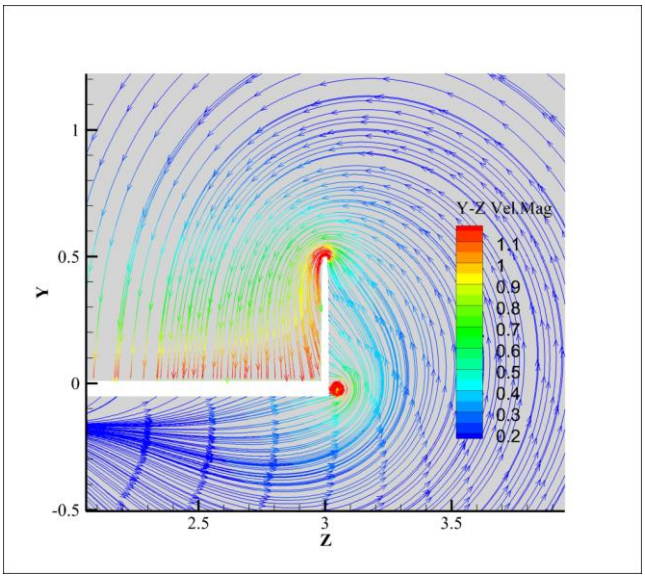

b)

Figure 6.4: Streamlines at 0.75c behind leading edge a) W0, b) W1, c) W2, d) W3.

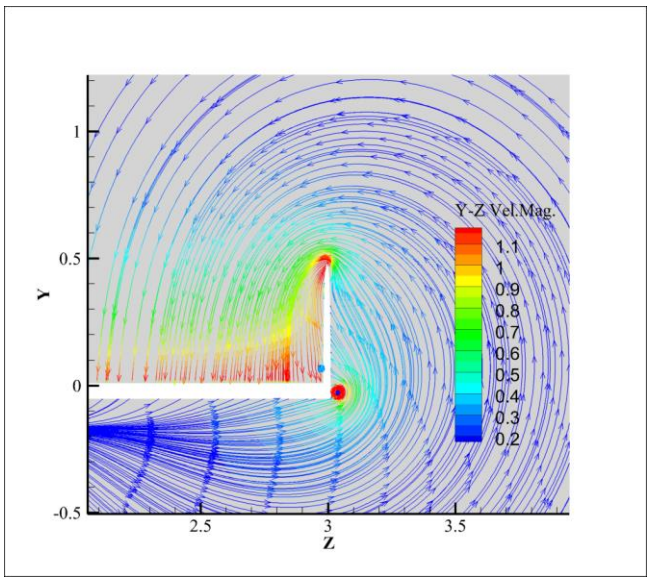

c)

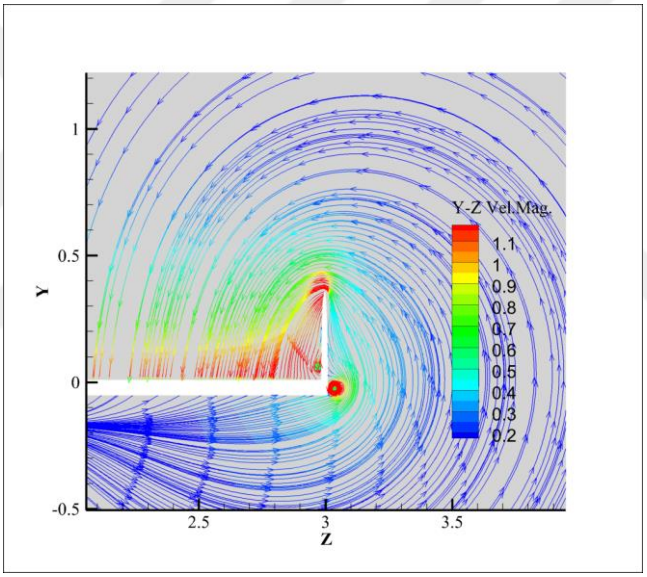

d)

Figure 6.4 (cont.): Streamlines at 0.75c behind leading edge a) W0, b) W1, c) W2, d) W3.

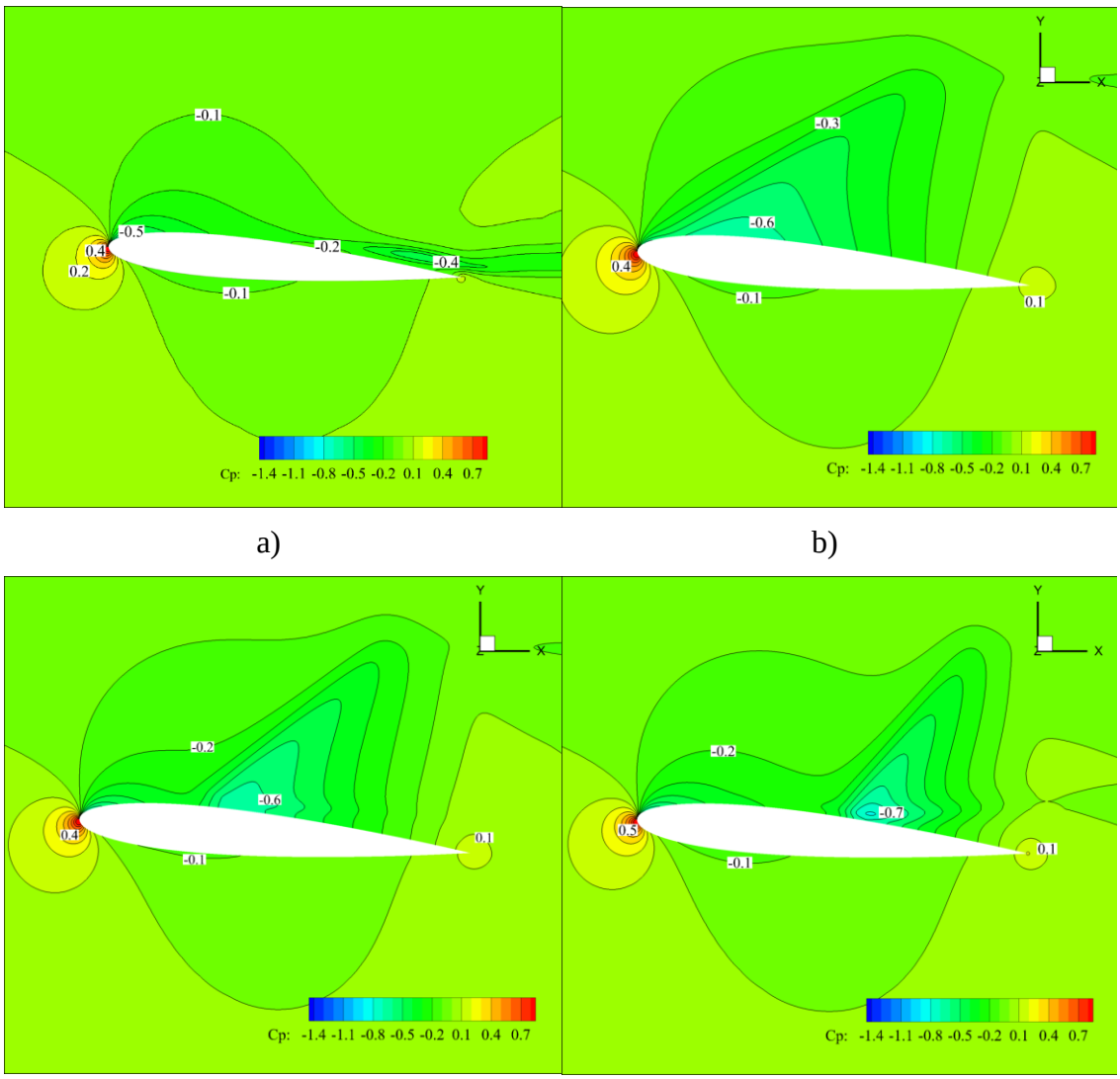

Figure 6.5: Cp contours at 2.95m outside from the root of the main wing a) W0, b) W1, c) W2, d) W3.

W3 has a larger drop in Cp like -0.7, yet just for a little point. It can be seen that coverages of other contours are lesser than W2. Independently from the efficiency factor, a moderate difference in Cp between the upper and lower sides along with a smoother distribution is preferred to local ups and downs of difference along with fluctuating values. Fluctuations are not desired for they might lead to unwanted flow separation and pose a higher risk of cavitation.

6.2 Effect of "SCR (Sw/Cmw)"

The ratio of the winglet span to chord length of the main wing (SCR) was investigated at three different values, namely 1, 0.75 and 0.5, with the ratio of the winglet root chord length to main wing chord length (CCR) equal to 1. The winglet configuration with SCR taken as 0.5 was already addressed and analysed in the previous sub-chapter. Thus, it was required to perform the analyses of the winglets with SCR equal to 0.75 and 1. The compared structures were labelled as (W1), (W4) and (W5) with SCR ratios equal to 0.5, 0.75 and 1, respectively.

As presented in Table 6.2, there is a parabolic trend in Cl/Cd values against increasing SCR. When compared to W0, the overall performance improvement for W1, W4 and W5 are read as 6.19%, 6.45% and 5.38%, respectively. Although obtained C_L values continuously rise as the winglet span grows, nearing the SCR of 1, the increments in C_L shrink in comparison to those of C_D. The increments in total drag coefficients (C_D) in comparison to W0 are calculated as 3.61%, 5.42%, and 7.23%, and the increments in lift coefficients (C_L) related to W1, W2 and W3 as 10.01%, 12.22% and 13%, respectively. Looking at these results, it can be deduced that extending the winglet span further reduces the effect of the W0 tip vortex. Yet, with the optimum SCR value of 0.75, the increment in viscous surface adds too much profile drag, countering the advantage of reduction in induced velocities.

Figure 6.6 shows the general trajectories of x vorticity. Vorticity distribution can be surveyed to identify the areas where big vortices develop. For all cases under scope, Table 6.4 features extreme x vorticity values recorded at the center of the fully developed vortices around the open tip at 0.75c, 0.5c, 0.25c and 0c in front of the trailing edge. Also in Figure 6.7, a comparative view of x vorticity distributions at 0.25c behind the trailing edges is presented with an emphasis on the open-end tip area of these three wingleted wings.

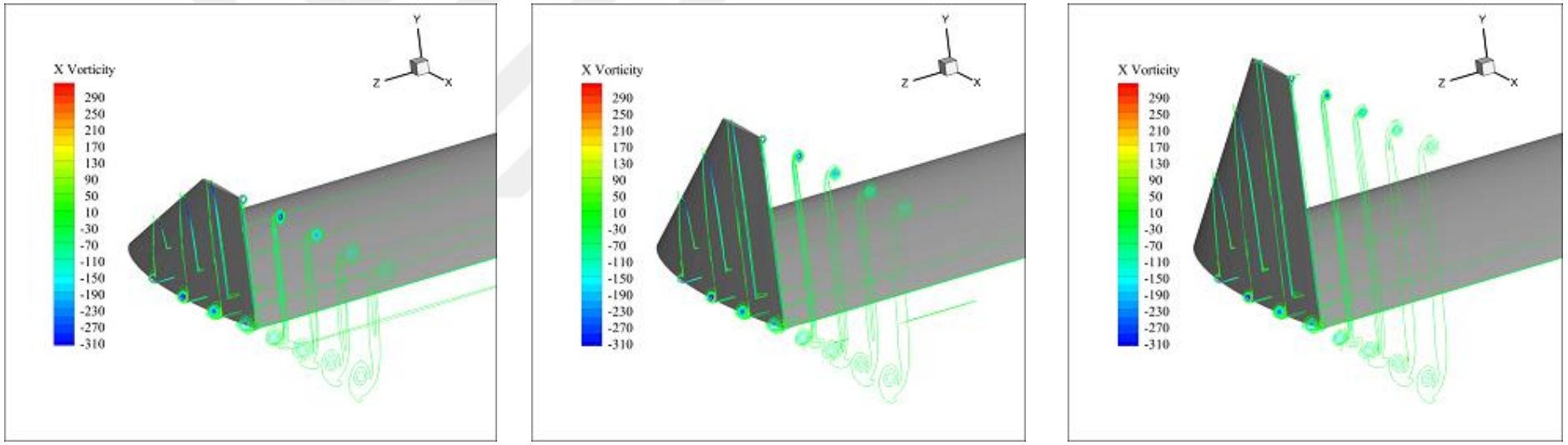

a) b) c)

Figure 6.6: X vorticity trajectories a) W1, b) W4, c) W5.

Table 6.4: X vorticity values of W1, W4, W5. ("–": no fully developed vortex; "Tip": winglet tip; "Upper J": upper part of the junction; "Lower J": lower part of the junction).

Location	W1	W4	W5
0.75 c front from trailing edge			
Tip	-	-	-
Upper J	120	-	-
Lower J	-900	-980	-980
0.5 c front from trailing edge			
Tip	-	-	-
Upper J	40	-	-
Lower J	-400	-440	-440
0.25 c front from trailing edge			
Tip	-	-	-
Upper J	-20	20	-20
Lower J	-240	-260	-260
At trailing edge			
Tip	-700	-680	-480
Upper J	-160	-140	-120
Lower J	-160	-180	-180

In Figure 6.4, it is observed that the general characteristics of x vorticity trajectories are fairly similar in three winglets. In fact, development patterns of the junction vortices are almost identical. There are only small differences at a maximum x vorticity magnitude, which evoke trivial shifts in shape and diameter. Despite this fact, it can be said that there is a slightly declining trend in upper junction vortices and a slightly ramping trend in lower junction vortices as the winglet with longer span is attached.

In all three winglet configurations, vortex generation at the winglet tip starts at a point quite behind, close to the trailing edge of the winglet. Interestingly, while the maximum x vorticity differs by as low as $20s^{-1}$ (2.85%) from W1 and W4, there is a dramatic difference of $200s^{-1}$ (29.41%) between W4 and W5.

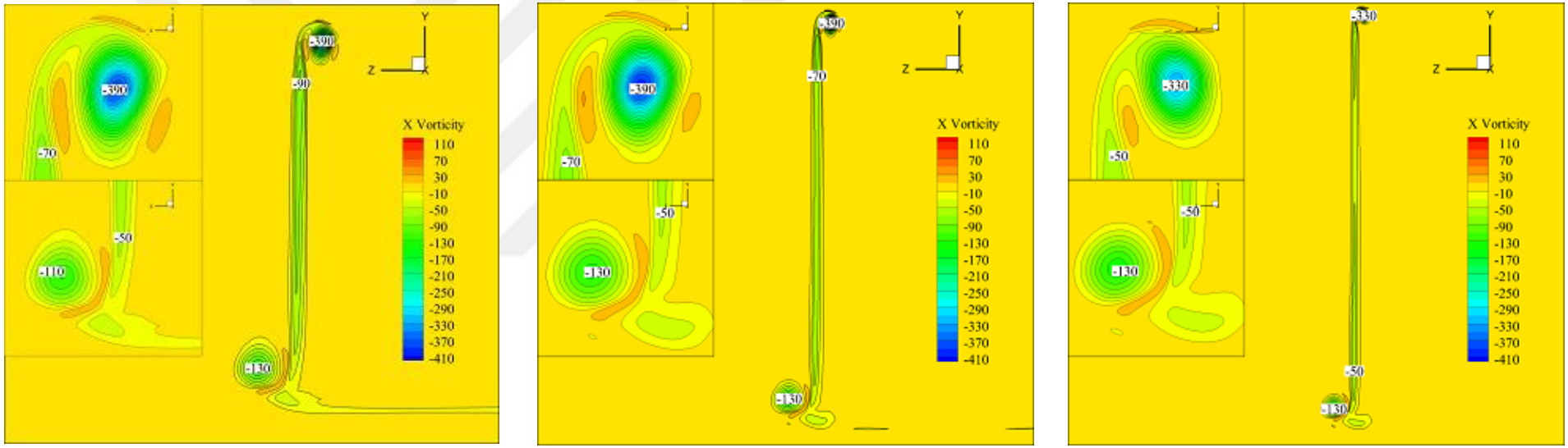

a) b) c)

Figure 6.7: X vorticity at 0.25c behind trailing edge (looking from behind) a) W1, b) W4, c) W5.

Also in the examination of the wake vorticity distribution at 0.25c behind the trailing edge in Figure 6.7, W5 performs the most optimal low vorticity values; especially at the winglet tip vortex which is also the most distant one from the main wing. Despite W5 should be the most efficient one, it has fairly higher drag coefficient than other two winglet configurations which rolls back its efficiency lower than W4, although it supplies the highest lift coefficient. This situation can be explained only by the extreme negative effect of increasing viscous drag force, which pulls the total drag force up by boosting profile drag force.

To better reflect the effects of the tip vortices and induced velocities in y and z directions on the low-pressure side of the main wing, Figure 6.8 indicates the streamlines at the x slice of 0.75c behind the leading edge via a velocity magnitude color scaling on the Y-Z plane. Streamline patterns of W4 and W5 are quite similar to W3. Albeit it is noted that Y-Z velocity magnitude in the region above low-pressure side decrease by increasing span of winglet. This strengthens the comments mentioned above for the results of coefficients and vorticity examinations.

The Cp comparison of z slice at 2.95m outer to the tip from the root of main wing is presented in Figure 6.9. It is observed that the coverage percentage of the contours on the surface of each wing are quite similar. However, the minimum value of Cp declines further from -0.6 to -0.8, and the elongation of the low value contours towards the tip of the winglet extends as the winglet span becomes larger. This infers that a longer winglet reduces the downwash more effectively, allowing a fluid flow at a higher rate of velocity on the low-pressure side of the main wing, as expected. However, a combination of higher velocity and a larger viscous area, the Reynolds number increases excessively and hence the profile drag force. Therefore, the overwhelming profile drag force vitiates the beneficial decrease in induced drag force.

Hence, as a conclusive statement, there is an optimum SCR for the maximum Cl/Cd performance. In this study, it is determined that the optimum value for the SCR is 0.75 of the carried out analyses. Nevertheless, it is important to note that the optimum SCR may differ according to the parameters such as aspect ratio of the main wing, general flow velocity, cross-section geometry of the main wing and the winglet, etc.

Considering the results obtained up to this point in Cl/Cd, which is the main comparison criterion, W4 was taken as the base configuration for investigation of subsequent parameters of winglet geometries in the following sub-chapters.

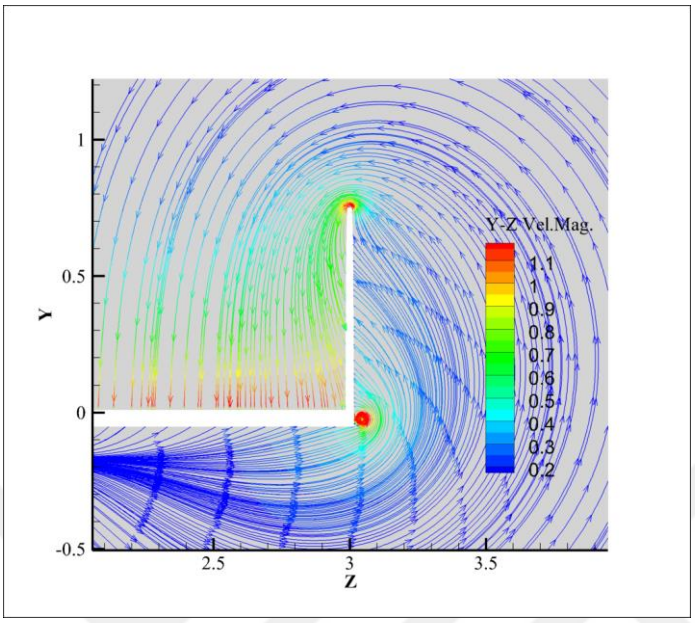

a)

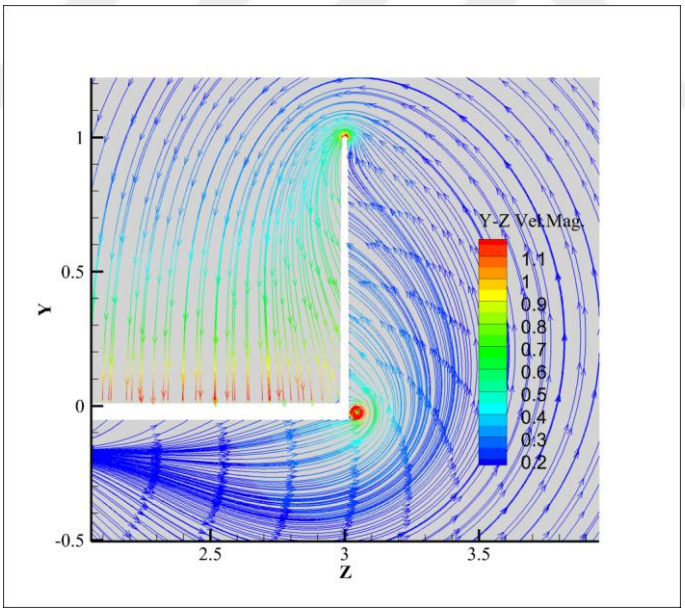

b)

Figure 6.8: Streamlines at 0.75c behind the leading edge a) W4, b) W5.

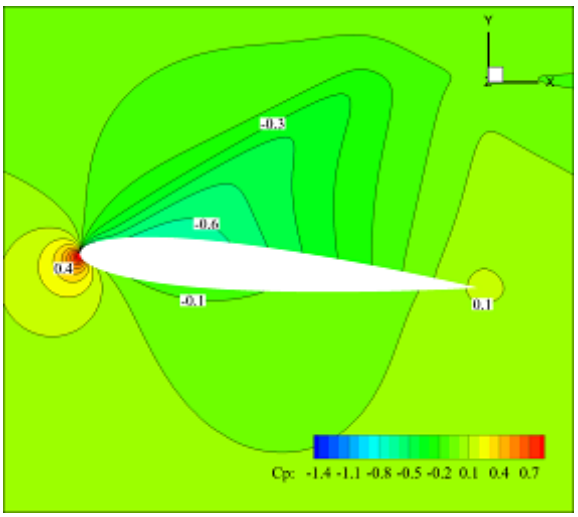

a)

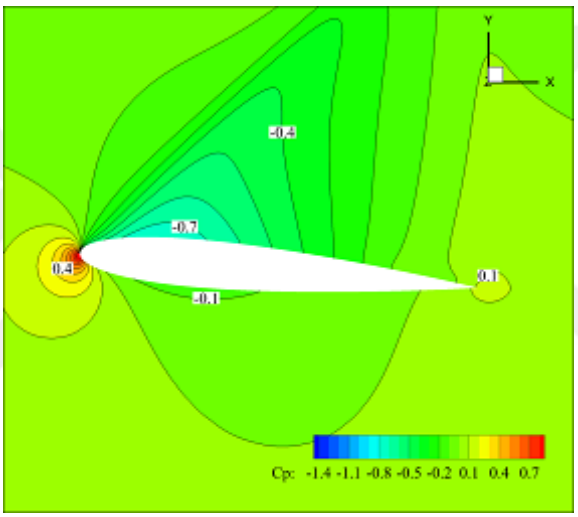

b)

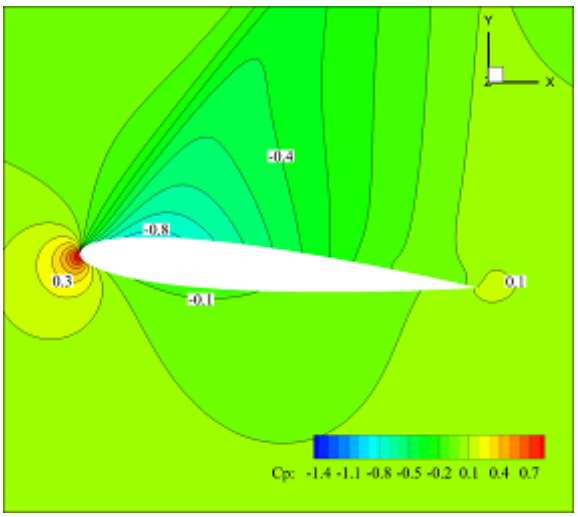

c)

Figure 6.9: Cp contours at 2.95m out from root of the main wing a) W1, b) W4, c) W5.

6.3 Effect of "direction of winglet"

Three different direction configurations were investigated with CCR equal to 1 and SCR of 0.75. These configurations are; upward (W4 from previous sub-chapter), downward and both directions (fence type). The configurations of downward and fence are denoted as W6, and W7 respectively.

According to Table 6.2, it is observed that W4 is still the most efficient configuration in terms of Cl/Cd. Cl/Cd gains of W4, W6 and W7 in proportion to W0 are 6.44%, 4.25% and 5.28%, respectively. Still for the W4, W6 and W7 configurations, comparison of C_L values indicates the respective gains as 12.22%, 4.25%, and 13.55%, relatively to the bare wing. As for reduction of induced velocities due to tip vortices, W7 generates the best gains vis-a-vis C_L values. In other respects, W6 performs the worst among all the winglet configurations. The C_D comparison, on the other hand, gives out a different picture. At W4, W6 and W7 configurations, the rises in C_D to W0 are read as 5.42%, 0% and 5.83%, respectively. W7 has the highest drag coefficient with a slight difference from W4 but even this slight increase is far from making its gain in C_L the most efficient.

Figure 6.10 shows the general trajectories of x vorticity. Vorticity distribution can be surveyed in order to determine the areas where large vortices develop. For all cases, Table 6.5 presents extreme x vorticity values at the center of the fully developed vortices around open tip at 0.75c, 0.5c, 0.25c and 0c in front of the training edge. Also in Figure 6.11, a comparative view of x vorticity distributions at 0.25c behind the trailing edges is presented with an emphasis on the open-end tip area of these three wingleted wings.

In Figure 6.10, it is seen that W6, the downward pointing winglet, fails to junction vortex prevent the twist of the towards the low-pressure side of the main wing. This explains why the gain in C_L of this configuration is so much lower than that of other configurations. In addition, C_{Di} should be higher than other configurations as there is a high downwash due to presence of an un-vanished upper junction vortex. However, W6 generates a smaller C_D within all configurations. This in turn weakens the extra C_{Dp} caused by the winglet to a great extent. As a matter of fact, it is not an unexpected result. Because, the lower side of the winglet is the high-pressure side; thus, general velocity magnitude in that region is lower than that of the upper side.

Accordingly, viscous drag is smaller on the downward pointing winglet than the upward pointing winglets.

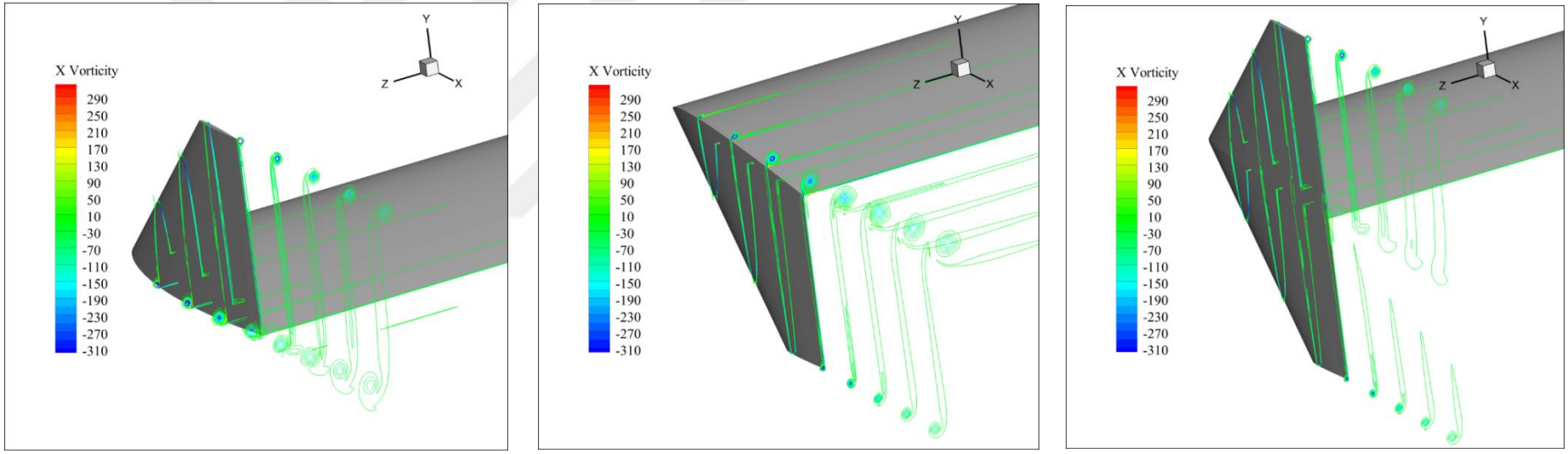

a) b) c)

Figure 6.10: X vorticity trajectories a) W 4, b) W6, c) W7.

Table 6.5: X vorticity values of W4, W6, W7. ("–": no fully developed vortex; "Tip": winglet tip; "Upper J": upper part of the junction; "Lower J": lower part of the junction).

Location	W4	W6	W7
0.75 c front from trailing edge			
Upper Tip	-	-	-
Upper J	-	-850	-
Lower J	-980	-270	-230
Lower Tip	-	-	-
0.5 c front from trailing edge			
Upper Tip	-	-	-
Upper J	-	-610	50
Lower J	-440	-70	-50
Lower Tip	-	-	-
0.25 c front from trailing edge			
Upper Tip	-	-	-
Upper J	20	-390	-
Lower J	-260	-	-
Lower Tip	-	-	-
At trailing edge			
Upper Tip	-680	-	-690
Upper J	-140	-250	-
Lower J	-180	-	-
Lower Tip	-	-590	-570

Looking at W7, the additional downward facing part of the winglet slightly contributes to reduction of induced velocities. However, this contribution of the downward part is even smaller due to the reduction added by the upper part. It only shifts the lower junction vortex away to a point further downward where its effect on the main wing weakens. However, in the configuration of W4, this vortex already cants toward the outer side of the winglet. Therefore, even if the viscous drag force is lower than the upper part, it will still be high enough to neutralize and even eliminate the additional gain in C_L for the sake of efficiency. Maybe, a fence type (both sided) winglet with a smaller downward part on the span would give a better result than W4 in Cl/Cd.

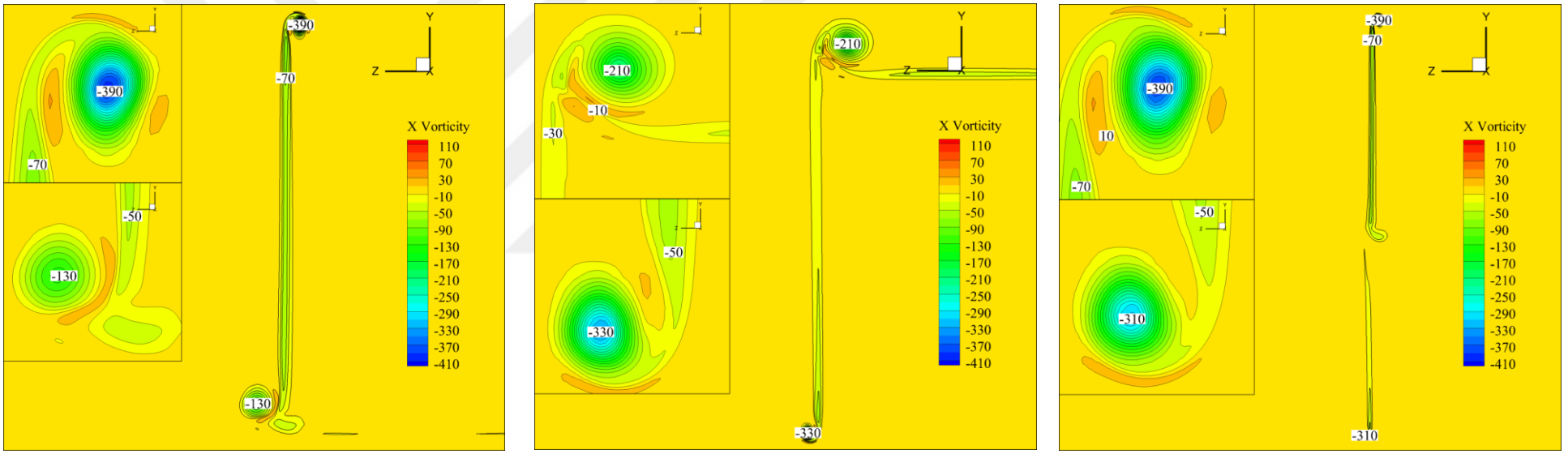

a) b) c)

Figure 6.11: X vorticity at 0.25c behind trailing edge (looking from behind) a) W4, b) W6, c) W7.

When Table 6.4 is surveyed, a strange issue can be observed. The upper junction vortex of W6 does not show the trend of starting with counter clockwise direction and then turning to clockwise direction. It arises in clockwise from the beginning with a x vorticity magnitude even higher than W0 on the forward half of the chord but diminishes faster on the rear half. Additionally, again unexpectedly, this fading rate does not continue in the wake region. As it can be seen in Figure 6.11, the vortex swaying from the tip of the main wing of W6 has a stronger vorticity than that of W0. This could be explained by the strong vorticities of the two uniting vortices behind W0 mitigating each other and becoming one weaker but larger vortex. In the wake of W6, the lower junction vortex shifting to the tips of winglets causes, the upper junction vortex to keep its strength a bit further without dispersing.

For a better understanding of the effect of the tip vortices and induced velocities in y and z directions on low-pressure side of the main wing, the streamlines at x slice of 0.75c behind the leading edge are shown with Y-Z plane velocity magnitude colour scaling in Figure 6.12. W6 could not shift or disperse the unfavourable vortex that cunting over the low-pressure side of the main wing. This vortex is slightly weaker than that of W0 but still has a significant negative effect. Coherent with its high C_L value, W7 provides the best reduction in induced velocities. It is clearly seen that the Y-Z velocity magnitudes of W7 are lower than all other configurations and also both vortices near the tip of the main wing are shifted successfully towards the tips of the winglet.

The Cp comparison of the z slice at 2.95m outer to the tip from the root of the main wing is presented in Figure 6.13. As observed on the chart, the upward facing winglet contributes to the lift by dropping the pressure on the low-pressure side, whereas the downward facing winglet has almost no effect on the low-pressure side. The downward facing winglet adds to the lift mainly by increasing the pressure of the high-pressure side of the wing. Moreover, the fence type (both sided) winglet gives a distribution of an almost exact combination of the distributions of the upward and downward winglets. These contours are in consistent with the obtained C_L results.

As a conclusion to this phase of the study, up to now, W4 is still the most efficient configuration among all the configurations tested.

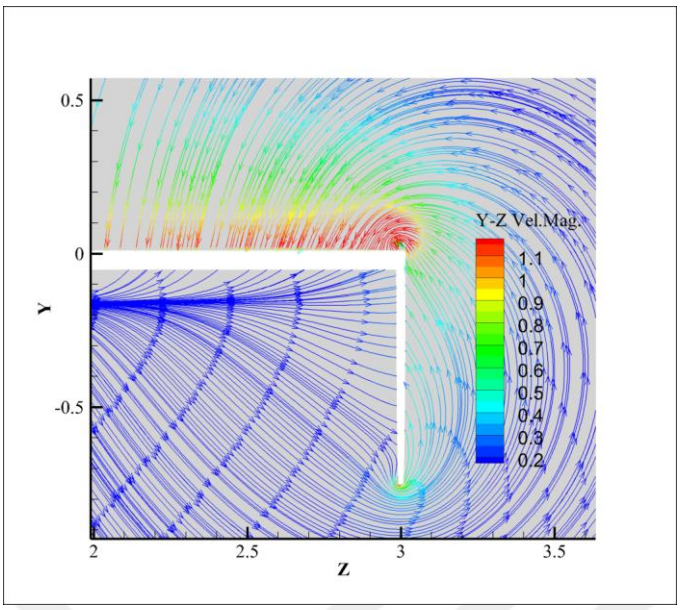

a)

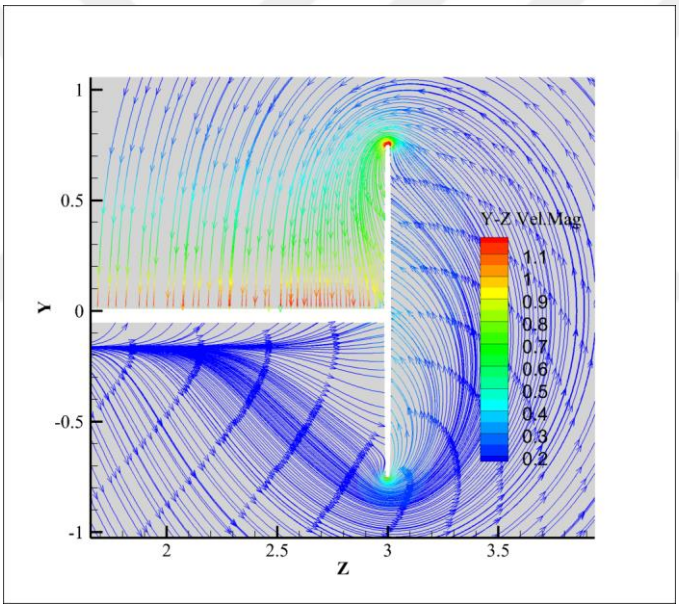

b)

Figure 6.12: Streamlines at 0.75c behind the leading edge a) W6, b) W7.

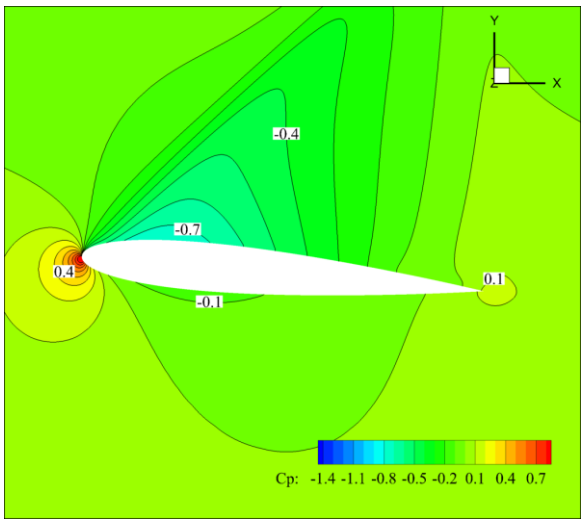

a)

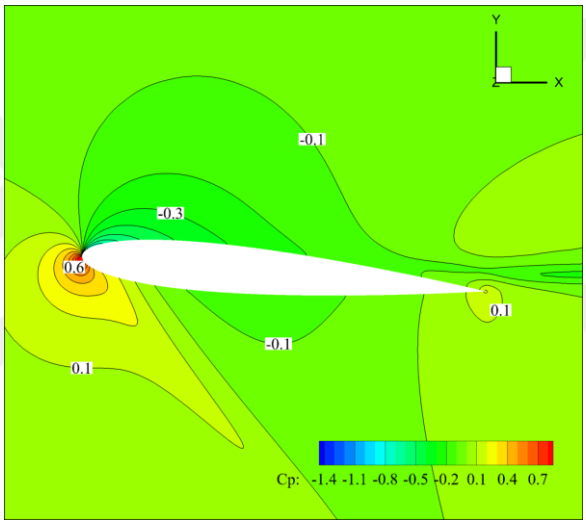

b)

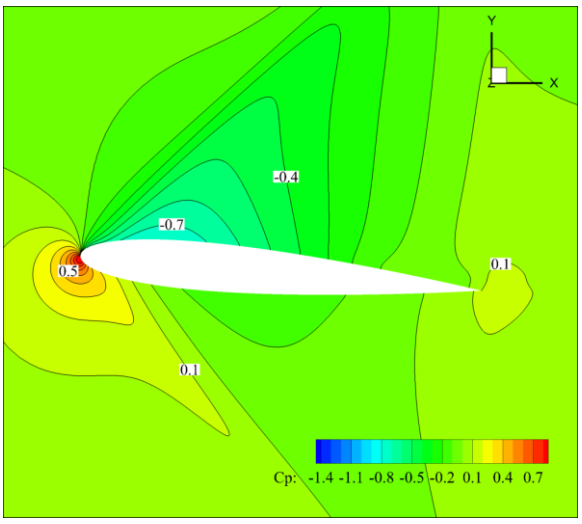

c)

Figure 6.13: Cp contours at 2.95m out from root of the main wing a) W4, b) W6, c) W7.

Yet, W6 is the only winglet configuration that does not increase the total drag force compared to W0. This fact is crucial for a project that only includes a winglet modification to a hydrofoil vessel without replacing the whole foil but merely mounting a winglet on the tip of the existing wing. At the maximum cruise speed of a hydrofoil vessel, the existing lift force is sufficient for raising the vessel's hull above the free surface, sono additional lift force will be required. Thence, independently of the efficiency of the configuration, any increase at the total drag will increase the the amount of power needed for propelling the vessel at top speed. Accordingly, in such situations, W4 would empower the vessel to pass to the foilborne condition from the hullborne condition at a remarkably lower speed, while, on the other hand, compromising the maximum speed. W6 would also decrease the lift off speed at a smaller rate than W4 due to lower efficiency. Yet, with no rise in the total drag force, the vessel will be able to cruise without compromising the maximum speed.

If the modification project involves replacing the whole foil then, constructing a smaller wing with configuration of W4 will give the opportunity of both cruising at a higher maximum speed and lift off at a lower speed.

6.4 Effect of "Winglet Trailing Edge Sweep Angle (Θ)"

The winglet configurations studied until this point had the trailing edge of the winglet fixed at 0^o (perpendicular to incoming flow direction). This final section compares W4 and W8 (W4 with Θ value of 15^o).

According to Table 5.2, the results are very close. In terms of C_L, W4 is slightly higher than W8 when compared to W0, with increments of 12.22% to 11.93% respectively. However, W4 has a slightly higher C_D value than that of W8 in comparison to W0, with increments of 5.42% to 4.82% respectively. As regards efficiency (Cl/Cd), W8 outperforms W4 by only 0.3%, which can be somewhat negligible as any comment might be invalid given the potential error of the CFD analysis itself.

In Figure 6.14 shows the general trajectories of x vorticity. Extreme x vorticity values at the center of the fully developed vortices around open tip at 0.75c, 0.5c, 0.25c and 0c in front of the training edge of all concerning cases are given in Table 6.6. Also in Figure 6.15, a comparative view of x vorticity distributions at 0.25c

behind the trailing edges focusing the open end tip area of the these 2 wingleted wings is presented.

In Figure 6.14, it is observed that the x vorticity evolutions of the lower junction vortices are almost identical for both winglet configurations. The majority of difference is seen in the trajectory of winglet tip. The strength of x vorticity of W8 continues a bit further behind in the wake when compared to W4. The swept tip of W8 postpones the developing and also the dispersing of the tip vortex. Figure 6.15 also corroborates the situation. As it is seen in wake region at 0.25 c behind the main wing, the strength of vorticity of W8 is 1.56 times greater than the strength of vorticity of W4. The color scaling of the contours sports a different color for each winglet in order to illustrate the whole range. Doch, it is possible to track the similarity of the contour patterns of lower junction vortex. In this situation, it can be said that, W8 leaves a more disturbed wake astern. This makes a bit more difficult to answer the question whether giving a sweep angle to the trailing edge of the winglet is beneficial or not.

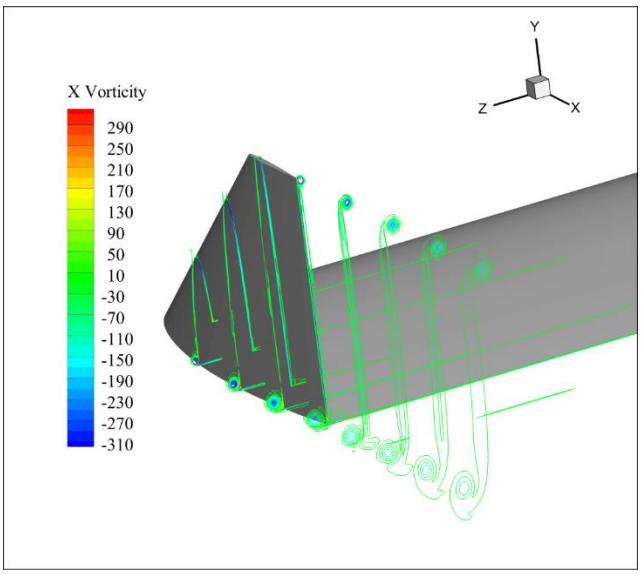

a)

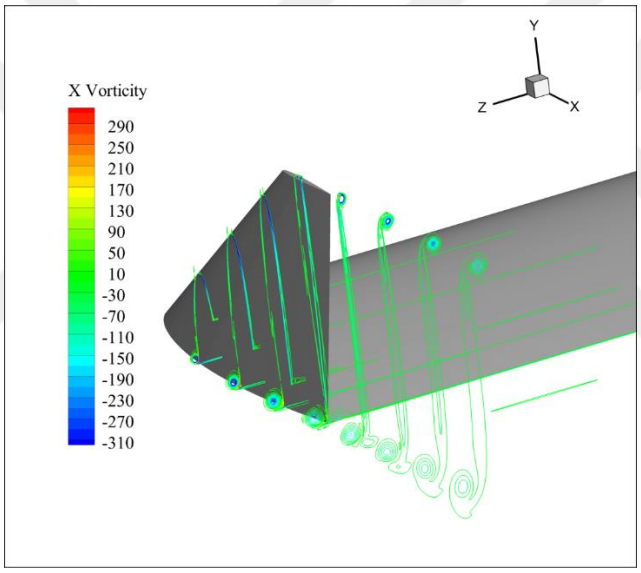

b)

Figure 6.14: X vorticity trajectories a) W4, b) W8

When Table.6.6 is examined, a high x vorticity value of 2100 s^{-1} greets the eye on the winglet tip at main wing trailing edge alignment within the values of W8. It is caused by a very little vortex developed along the sharp winglet edge, which is also very hard to track in Figure 6.14. Presumably, it does not have a significant effect on the main wing.

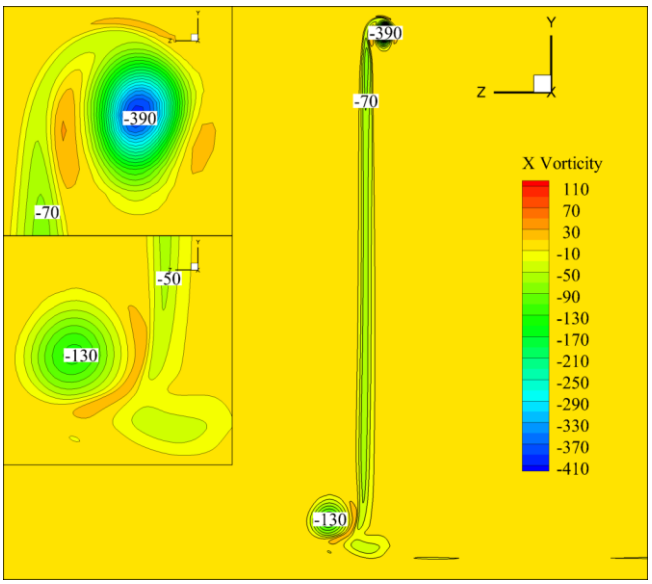

a)

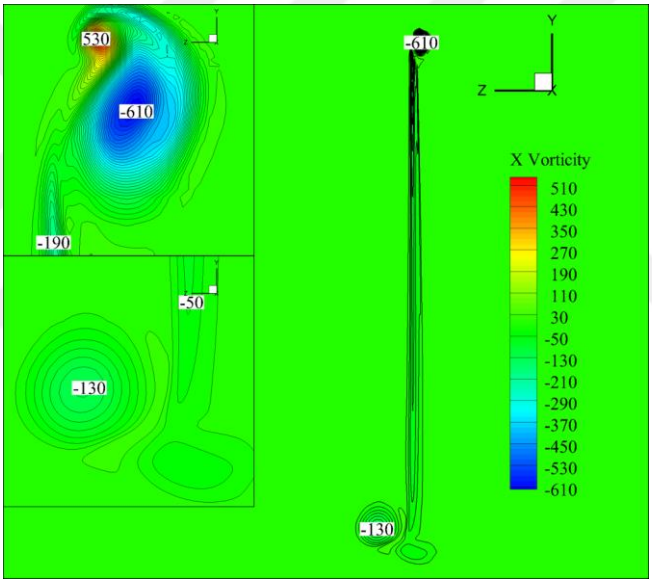

b)

Figure 6.15: X vorticity at 0.25c behind trailing edge (looking from behind) a) W4, b) W8.

For a better understanding of the effect of the tip vortices and induced velocities in y and z directions on low pressure side of the main wing, the streamlines at x slice of 0.75c behind the leading edge of W4 and W8 are shown with Y-Z plane velocity magnitude colour scaling in Figure 6.16. It is seen that the magnitudes of induced velocities of W8 are apparently higher than that of W4. Besides, the outer junction vortex of W8 is larger.

Table 6.6: X vorticity values of W4, W8. ("–": no fully developed vortex; "Tip": winglet tip; "Upper J": upper part of the junction; "Lower J": lower part of the junction).

Location	W4	W8
0.75 c front from trailing edge		
Tip	-	-
Upper J	-	-
Lower J	-980	-930
0.5 c front from trailing edge		
Tip	-	-
Upper J	-	-
Lower J	-440	-430
0.25 c front from trailing edge		
Tip	-	-
Upper J	-20	-20
Lower J	-260	-250
At trailing edge		
Tip	-680	-2100
Upper J	-140	-140
Lower J	-180	-170

The Cp comparison of z slice at 2.95m outer to tip from root of main wing is presented in Figure 6.17. The contours below the wing are identical for both configurations. The contours above the wing draw patterns in a trend of parallel to the slopes of the leading and trailing edges of the winglet. But the most significant difference is the coverage distribution of the contours on the low pressure side. Until the Cp drops to -0.5, the coverages of contours are almost the same. However, when contours of -0.6 and -0.7 are examined, it can be seen that the contours of W8 cover a smaller than those of W4. This difference in distribution also explains the slight difference in C_L. The higher pressure profile of the W8 gives it a small edge in reducing the cavitation risk.

As a conclusion to this comparison, W8 has advantages of a slight higher efficiency and a relatively preferable pressure distribution; on the other hand, it has some disadvantages such as geometry that is more complex and a more distorted wake characteristic. In different circumstances like a different wing section, a different aspect ratio of main wing, a different Reynolds number etc., the result may be more distinctive in usefulness.

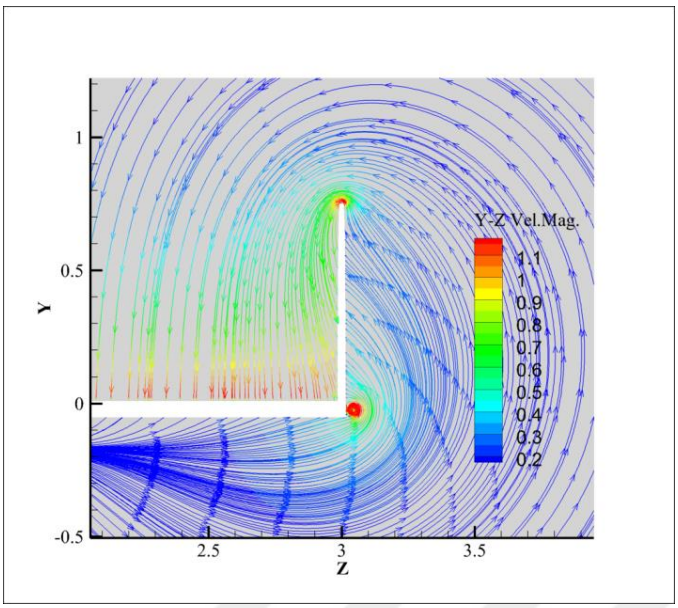

a)

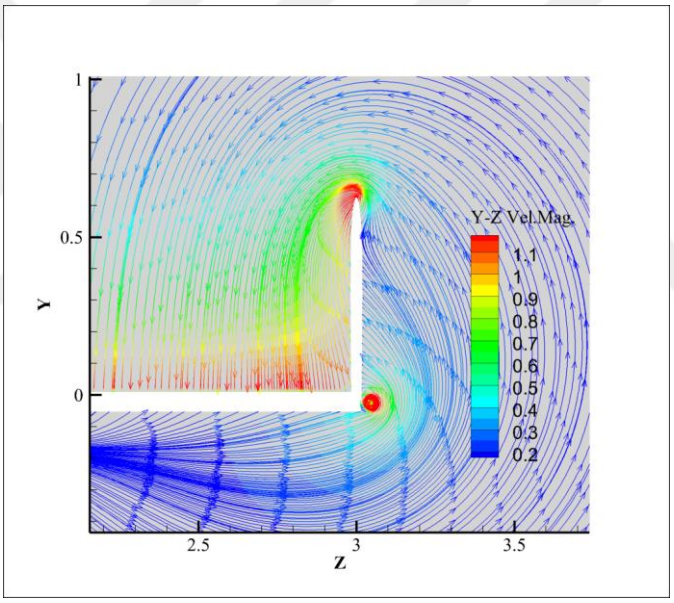

b)

Figure 6.16: Streamlines at 0.75c behind the leading edge a) W4, b) W8.

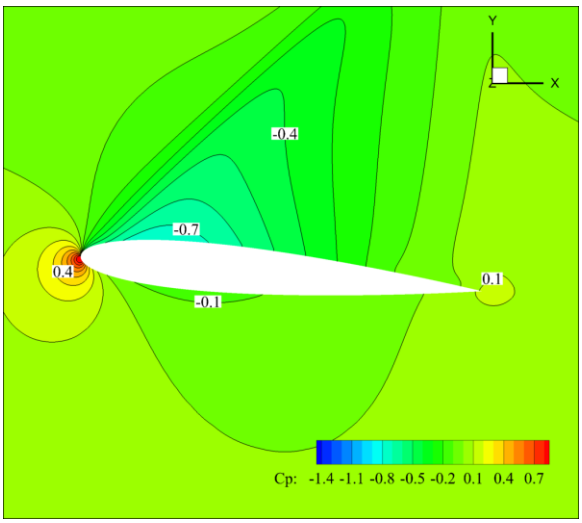

a)

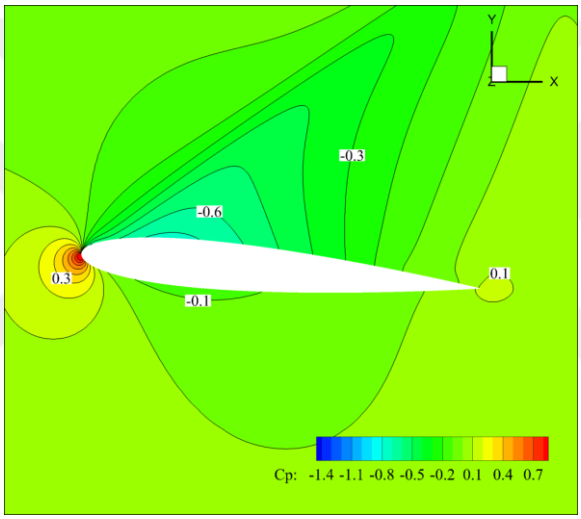

b)

Figure 6.17: Cp contours at 2.95m out from root of the main wing a) W4, b) W8.

6.5 Discussion

When the Cl/Cd value, the assessment criteria is considered, it is deduced that W4 and W8 are the most efficient configurations with very similar results. On the other hand, W6 is the only configuration that does not increase the total drag force coefficient. This means that W6 is the only configuration that can be used without the need to change any dimension and parameter of the main wing. Even if the gain in efficiency turns out low; W6 would enable switching to the foilborne condition at a lower speed, which would provide a higher lift force for the same drag force. W4 and W8 have the same ability as well. In fact, they would lower the lift off speed much more than W6 due to the higher Cl/Cd ratio. However, if these winglets are

applied to an existing wing, they would generate a higher drag force at the maximum speed of the craft where the craft needs no more lift (it is already lifted off the water). The use of W4 or W8 requires the replacement of the entire wing. The new wing could have a smaller size or smaller angle of attack in order to keep the drag force at the same or lower level at the maximum cruise speed. Here, the new wing can be designed for three different purposes. The first option is keeping the drag force constant at the maximum speed. This way, maximum speed of the craft would not change whereas the lift off speed would decrease significantly, providing the necessary lift force to lift off at a lower speed. This is the same effect that W6 provides but only with better results. The second option is keeping the lift force constant, which would not change the lift off speed but lower the effective power required to speed up by generating a smaller drag force. In addition, if there is no cavitation or separation problems, it would allow the craft to climb up to a higher maximum speed. Moreover, the third option is using both of these improvements with lower gains. However, it is noteworthy that W4 and W8 are both upward pointing winglets. For this reason, when using these winglets, it would be harder to create a design free from cavitation, ventilation or emergency problems. In contrast, W6 is a downward pointing winglet. Thus, it is less likely to encounter such problems with W6.

7. CONCLUSION & FUTURE WORK

In this study, the effects of some basic geometrical parameters of a NACA0006 sectioned winglet with fixed taper ratio of 0.3 attached on a hydrofoil were examined in feasibility and efficiency scope by using CFD. The parameters comprised chord, span and direction of the winglet, and sweep angle of the winglet's trailing edge. A rectangular wing with Aspect Ratio (Λ)=6 and NACA0012 section was chosen as the main wing. The Angle of Attack (AoA) of the main wing and the Reynolds number of pure water (the selected fluid) were kept constant and taken as 5^o and $6x10^6$ respectively. The results were examined taking into consideration the lift force, drag force and wake characteristic changes caused by the winglets. Some interpretations were made about the practical usage of winglets on hydrofoil vessels along with advantages and disadvantages.

7.1 Conclusion

Firstly, in the inspection of the ratio of root chord length of winglet to chord length of mainwing (CCR), namely the main wing tip coverage of the winglet, it is deduced that the winglet covering the entire chord of the main wing is significantly more efficient than using a winglet with a smaller chord at the junction edge. It is observed that the winglet shows the best performance in reducing the unfavoured vortex generation along the junction edges which affect the low-pressure side of the main wing.

Afterwards, in the inspection of the ratio of the span length of the winglet to the chord length of the main wing (SCR), the most efficient result was obtained with the value of 0.75 within three values of 0.5, 0.75 and 1. But, a detailed examination was made for all the analyses results, it was noticed that the efficiency of the winglet shows a parabolic trend with increasing SCR. This means, after this optimum value the additional profile drag caused by the area of the winglet starts to make the lift increment and induced drag decrease obsolute which assured by shifting the tip vortex away. By the way, it is deduced there is an optimum SCR which provides the

highest efficiency and also it is predicted that this optimum SCR may change with different wings and outflow circumstances. Thus, for every different kind of wing, an optimum SCR examination should be made.

By the results the examination of CCR and SCR, the winglet labelled as W4 was found as the most efficient winglet among tested values which has the CCR value of 1 and SCR value of 0.75.

The subsequent investigation addressed the direction of the winglet. Accordingly, the direction of the upward pointing winglet (W4) was changed, and two other winglet configurations were analysed: the downward facing W6, and fences double-sided (fence) oriented, W7. This analysis demonstrated that the downward facing winglets are not as successful as upward facing ones in mitigating the effects of tip vortices. Nevertheless, the downward pointing W6 proved to be only winglet configuration that does not increase the total drag force on the wing. Therefore, it is estimated that W6 offers convenience in cases where the total drag force does not increase is more essential than the increase in the ratio of lift force to drag force. Although W7 yielded the highest lift force, its Cl/Cd efficiency fell behind W4 due to its large viscous area which increases profile drag too much. This may be useful where high lift is needed without regard to drag force, which is unlikely for hydrofoil vessels. It is however noted that with a smaller downward pointing part, it may perform more efficiently and therefore would be more applicable.

In order to observe if a swept geometry procures any gain in efficiency, W8 configuration was analysed with a swept type of W4 winglet. W8 configuration, which has a sweep angle of trailing edge of 15^{o}, executes a lower lift force than W4 but also a lower drag force whose efficiency (Cl/Cd) shows insignificant difference compared to the efficiency of W4. The W8 has a much more complicated structure and requires a larger wing. This requirement translates into more material to achieve the same lifting force and efficiency, which greatly reduces the likelihood of being preferred to W4.

Finally, out of the winglet configurations in question, W4 proved the most efficient, generating an increase of 6.44% in efficiency (Cl/Cd), an increase of 12.22% in C_L and an increase of 5.46% in C_D in comparison to the bare wing. Besides, W6 provides an increase of 4.25% in Cl/Cd without causing any increase in C_D.

7.2 Future Work

This study investigates the effects of certain parameters of basic structured and low-cost winglets that can be installed on a hydrofoil vessel's underwater wings with respect to wing efficiency. For a convenient assembly, the interfaces between a wing and a winglet were constructed with rough junctions. In prospective researches, a more detailed parametric study can be conducted with different main wings and various Reynolds numbers with the purpose of obtaining more significant and easily interpretable results. Additionally, a more important factor is the effect of the free surface, which was not taken into account in this study. Unsteady analyses featuring more powerful clusters and free surface modelling should be run to provide more realistic data.

REFERENCES

Anderson, J.D. (1996). *Computational Fluid Dynamics: An Introduction.* Berlin, Germany: Springer.

Anderson, John D. (2001). *Fundamental of Aerodynamics*, McGraw-Hill, Boston.

Azlin, M.A., Mat Taib, C.F., Kasolang, S., Muhammad, F.H. (2011). CFD Analysis of Winglets at Subsonic Flow. *Proceedings of the World Congress on Engineering 2011 Vol I.* WCE 2011, London, U.K.

Blazek, J. (2001). *Computational Fluid Dynamics: Principles and Applications.* Oxford, UK: Elsevier.

Botez, R.M., Gabor, Ş.O., Koreanschi, A. (2016). A new non-linear vortex lattice method: Applications to wing aerodynamic optimizations. *Chinese Journal of Aeronautics, 29(5):* 1178–1195

Breslin, J.P. & Andersen, P. (1994). *Hydrodynamics of Ship Propellers.* Cambridge University Press.

Davidson, L. (2005). *Numerical Methods for Turbulent Flow, MTF071 Lecture Notes.* Göteborg, Sweden: Department of Thermo and Fluid Dynamics, Chalmers University of Technology.

Deardorff, J.W. (1970). A numerical study of three-dimensional turbulent channel flow at large Reynolds numbers. *Journal of Fluid Mechanics, Vol. 41 Issue 02,* 453- 480.

Elham, Ali & Van Tooren, Michael J.L. (2014). Winglet multi-objective shape optimization. *Aerospace Science and Technology 37,* 93–109. Elsevier.

Faltinsen, O.M. (2005). *Hydrodynamics of High-Speed Marine Vehicles.* Cambridge University Press.

Ferziger, J.H. & Peric, M. (2002). *Computational Methods for Fluid Dynamics.* New York, USA: Springer.

Guatham, N. & Bibin, J. (2016). Effect of winglets induced tip vortex structure on the performance of subsonic wings. *Aerospace Science and Technology 58* 328–340.

Gavrilovic, N.N., Rasuo, B.P., Dulicravic, G.S., Parezanovic, V.B. (2015). Commercial aircraft performance improvementusing winglets. *FME Trans., 43 (1) pp. 1-8*

Heyes, A.L. & Smith, D.A.R. (2005). Modification of a wing tip vortex by vortex generators. *Aerospace Science and Technology 9* 469–475.

Heyson, H.H., Riebe G.D., Fulton, C.L. (1977). Therotical parametric study of the relative advantages of winglets and wing-tip extensions. *NASA TM X-74003.*

Hoffmann, K.A. & Chiang, S.T. (2000). *Computational Fluid Dynamics for Engineers Volume 1-2-3.* Kansas, USA: Engineering Education System Publication.

Issa, R. I. (1986). Solution of the Implicitly Discretized Fluid Flow Equations by Operator Splitting. *Journal of Computational Physics 62(1),* 40-65.

Johnson, R.W. (1998). *The Handbook of Fluid Dynamics.* Boca Raton: CRC Press.

Katz, J. & Plotkin, A. (1991). *Low speed aerodynamics: from wing theory to panel methods*. New York: McGraw-Hill Inc.

Komerath, N., Pearson, J., Smith, P.J., Ames, R., Wong, O. (2001). Performance analysis of a wing with multiple winglets. *AIAA*-2001-2407.

Liang, H., Sun, H., Zong, Z., Zhou, L., Zou, L. (2012). Analytical modelling for a three-dimensional hydrofoil with winglets operating beneath a free surface. *Applied Mathematical Modelling 37,* 2679–2701.

Menter, F.R. (1992a). Influence of Freestream Values on k-ω Turbulence Model Predictions. *American Institute of Aeronautics and Astronautics Journal: Technical Notes 30(6),* 1657-1659 .

Menter, F.R. (1993). Zonal Two Equation k-ω Turbulence Models for Aerodynamic Flows. *Orlando, Florida, USA.: American Institute of Aeronautics and Astronautics Report,* 93-2906.

Menter, F.R. (1994). Two-Equation Eddy-Viscosity Turbulence Models for Engineering Applications. *AIAA Journal 32(8),* 1598-1605.

Moin, P. & Mahesh, K. (1998). Direct numerical simulation: a tool in turbulence research. *Ann. Rev. Fluid Mech. 30,* 539 - 578.

Panagiotou, P., Kaparos, P., Yakinthos, K. (2014). Winglet design and optimization for a MALE UAV using CFD. *Aerospace Science and Technology 39,* 190–205.

Patankar, S.V. & Spalding, D.B. (1972). A Calculation Procedure for Heat, Mass and Momentum Transfer in Three-Dimensional Parabolic Flows. *International Journal of Heat and Mass Transfer 15,*1787-1806.

Patankar, S.V. (1980) *Numerical Heat Transfer and Fluid Flow*. McGraw-Hill, New York, USA.

Whitcomb, R. (1976). A design approach and selected wind tunnel results at high sub-sonic mounted speeds for winglets. *NASA TN-D-8260.*

Schlichting, H. & Gersten, K. (2000). *Boundary-layer Theory* (8th revised ed.), Springer, ISBN 3-540-66270-73.

Tennekes, H. & Lumley, J.L. (1972). *A First Course in Turbulence*. MIT Press, Cambridge, UK.

Ünal, U.O. (2007). Girdap Yaratıcıların Dairesel Silindir Etrafındaki Akışa Etkisinin Deneysel ve Hesaplamalı Olarak İncelenmesi. (Doktora tezi). *İstanbul Teknik Üniversitesi, Fen Bilimleri Enstitüsü, İstanbul.*

Ünal, U.O., Ünal, B., Atlar, M. (2012). Turbulent boundary layer measurements over flat surfaces coated by nanostructured marine anti-foulings. *Exp. Fluids 52,* 1431-1448.

Van Doormall, J.P. and Raithby, G.D. (2984). Enhancements of the SIMPLE method for predicting incompressible fluid flows. *Numerical Heat Transfer, 7,* 147-163.

Versteeg, H. K. & Malalasekera W. (1995). *An Introduction to Computational Fluid Dynamics: The Finite Volume Method*. Harlow, England: Longman Group Ltd.

Wesseling, P. (1992). *An Introduction to Multigrid Methods.* New York, USA.: John Wiley, Chichester.

Wilcox, D.C. (1988a). Multiscale model for turbulent flows. *American Institude of Aeronautics and Astronautics Journal, 26(11),* 1311-1320.

Wilcox, D.C. (1994). *Turbulence Modeling for CFD.* California, USA: DCW Industries, Inc.

URL1, < https://turbmodels.larc.nasa.gov/naca0012_val_sst.html > *date received: 15.10.2016*

CURRICULUM VITAE

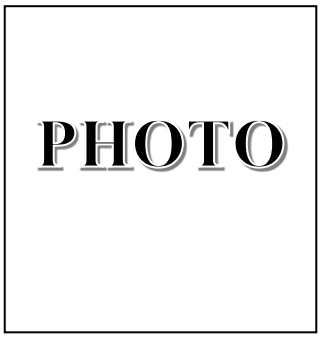

Name Surname **:** Aras Çetinkaya

Place and Date of Birth **:** ANKARA 1986

E-Mail : cetinkayaar@itu.edu.tr

EDUCATION **:**

- **B.Sc.** **:** 2009, Yildiz Technical University, Faculty of Naval Architecture and Maritime, Naval Architecture and Marine Engineering Department.
- **M.Sc.** **:** 2017, Istanbul Technical University, Faculty of Naval Architecture and Ocean, Naval Architecture and Marine Engineering Department.